Department of Precision and Microsystems Engineering

Air-based contactless positioning of thin substrates

Niek Verbruggen

Report no : MSD 2017.029
Coach : Dr.ir. R.A.J. van Ostayen
Professor : Dr.ir. R.A.J. van Ostayen
Specialisation : Mechatronic System Design
Type of report : Master Thesis
Date : 3 July 2017

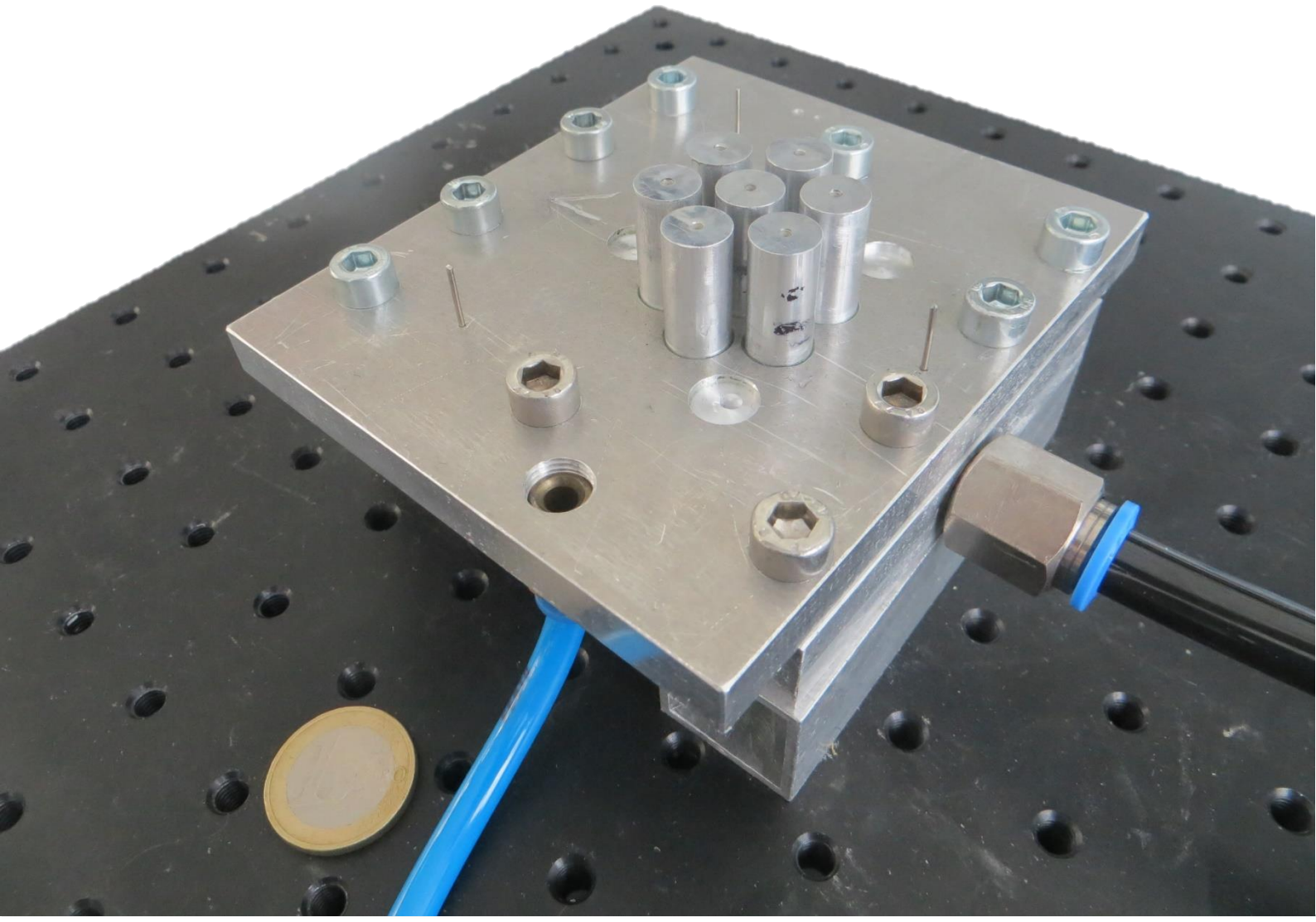

TU Delft Delft University of Technology

Challenge the future

Air-based contactless positioning of thin substrates

Exploring the outlet restriction variation concept

by

N. Verbruggen

to obtain the degree of Master of Science
at the Delft University of Technology,
to be defended publicly on Wednesday July 12, 2017 at 9:30 AM.

Student number:	4111087	
Project duration:	August 15, 2016 – July 12, 2017	
Thesis committee:	Dr. ir. R.A.J. van Ostayen,	TU Delft, supervisor
	Dr. ir. J.F.L. Goosen,	TU Delft
	Dr. ir. M. Langelaar ,	TU Delft
	Ir. J.W. Spronk,	TU Delft

An electronic version of this thesis is available at `http://repository.tudelft.nl/`.

TU Delft

Preface

This report is a result of my thesis study, which is the final deliverable of the master Mechanical Engineering, track Precision and Microsystems Engineering at the Delft University of Technology. Eleven months ago, I decided to start this project after an exploratory discussion with Ron. I liked the state of the art and the possibilities of the air based contactless technology. Moreover, the possibility to create a prototype did fit my interests.

The project did actually start with the task to improve the mechanical design of the Flowerbed, however already in the first week the idea of a continuous outlet restriction using a thin air film around an actuator came to my mind, which changed the topic of my research. I would like to thank Ron for his flexible attitude and the given possibility to elaborate on this idea. Moreover, I would like to thank Ron as well for the many interesting discussion we had. Our meetings did nearly always start a few minutes too late and it was no exception that our meeting did end more than a few minutes too late. The reason was simple, both of us were still enthusiastically exchanging new ideas for the contactless technology. Moreover, if I skipped a weekly meeting to play jass (klaverjassen) with my granddad, Ron's reaction was very positive and understanding. Again, I'm very thankful for our co-operation.

Also, I would like to thank Piet, Gerard and especially Rene and Wim for their help in the faculty workshops. Although I had many questions and was not very skilful at the start of my project, these guys did help me out with their experience. I can easily say that I would never get my setup performing as it does now with only my knowledge from the internet. Conventional machining is true craftsmanship, that even in midwinter in the freezing cold starts at 6:30 AM to help a student to get his job done before the workshop gets crowded.

The next people who do earn my gratitude are the technical support staff from PME consisting of Harry, Patrick, Rob and Spiridon. Some days I were constantly knocking on their doors to get parts and materials for my setup. The constant struggle to find the correct connecting pieces for the pneumatic lines in my setup, I will not quickly forget. Moreover, with their help I was even able to remove super glue efficiently and without damage from my laptop screen.

Also, the fellow students with who I shared the lab and our little 'office' I would like to thank. Special thanks to Jelle, Roy, Ruben and Thomas, who managed to keep me smiling during the whole project. Next to them I would also like to say 'thank you' to all my other friends and family who supported me the past months. There were so many of you, who always asked interested questions.

At this moment I would also like to thank my parents, who gave me the past seven years all the trust required to finish my studies successfully and in the pace I wanted it. I do hope that all their economic, but above all emotional, support will pay off.

And last but certainly not least, I would like to thank Vesna for her patience and listening to my boring stories about equations, micro meters, adiabatic expansion, viscous forces and so much more.

N. Verbruggen
Delft, July 2017

Abstract

This MSc. thesis describes the steps that have been taken to explore a new concept in the field of contactless positioning of thin substrates using a thin air film. The thin air film is able to levitate objects with a force equal to the average pressure between the actuator and object. The actuation force is created by the viscous drag of the air flow. The state of the art of contactless positioning using a thin air film shows potential for improvements, in terms of bandwidth or manufacturability. To make use of this potential, the outlet restriction variation concept is created. Next to the seen potential for a concept with a high bandwidth that is still manufacturable, another benefit is that the presence of an outlet restriction leads to a lower waste of vacuum flow in case of absence of a flying object above the actuator.

The Reynolds equation is introduced and the derivation of relevant equations to determine force and mass flow density is done. Afterwards the outlet restriction variation concept is analysed and compared with the state of the art, the stepped and tilted surface concepts. In the two-dimensional analysis a similar performance, force over mass flow, is found. This is a good result since the benefits of the outlet restriction variation concept are expected in the terms of high bandwidth and manufacturability.

Afterwards a three-dimensional actuator design based on the outlet restriction variation concept is discussed. A capillary inlet restriction, modelled with the adiabatic Fanno flow theory has been chosen in combination with a continuous outlet restriction surrounding the inlet in a circle. Such an outlet can be made with a cylindrical actuator pin that is positioned in the centre of a circular hole. The inlet is connected to the source pressure p_s and the outlet to the vacuum pressure p_v, meaning that air will flow between actuator and object from the inlet to the outlets. The outlet restriction is based on a thin film restriction that can be modelled with the Reynolds equation. Changing the position of the actuator pin relative to the hole, changes the gap widths of the outlets. Figure 1 shows a cross section of such an actuator pin and hole combination. Moving both parts relative to each other leads to restriction differences on opposite sides of the inlet, such that a net air flow will be generated towards the outlet with larger gap width, see figure 1. Controlling the restriction is done close the surface which is beneficial for the bandwidth.

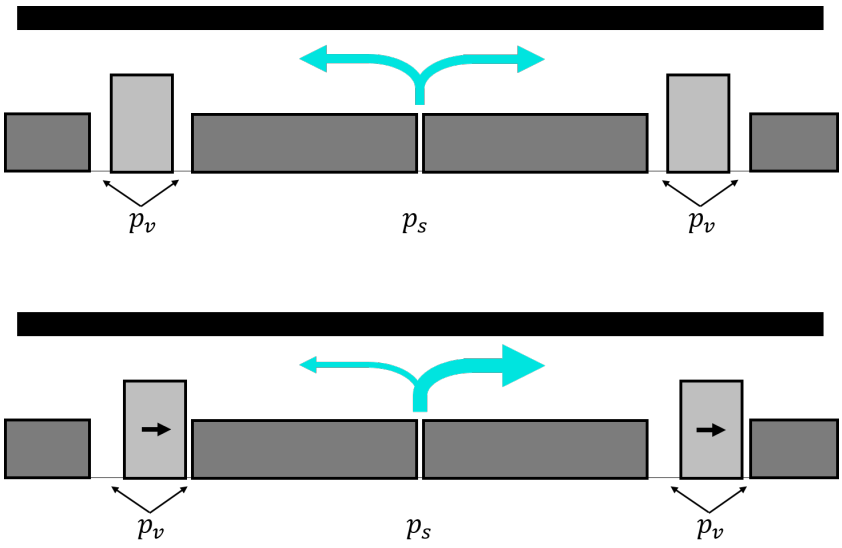

Figure 1: Cross-section of the working principle of the outlet variation concept: A relative movement of the dams with respect to the inlet restriction creates different outlet restrictions which lead to a net air flow resulting in a viscous force.

In the next phase, a setup was created. An actuator with seven pin hole combinations is made in house with conventional machining techniques using a mill and lathe. Crucial in the manufacturing process is the concentricity of the pins and holes creating the gap width. An average gap width of 50 μm has been realised. A study into the possible off-centre placement of actuator pins showed that the maximum force will reduce

as a result of a lower actuation range. Moreover, the influence of the off-centre placement itself is not as significant as the reduction of the actuation range when averaging over all off-centre placements directions.

The created outlet restriction setup has been tested and relevant parameters are measured. Using a precise dial indicator fly height/film thickness is measured at 19.0 μm with a standard deviation of 1.46 μm. The pocket depth, height difference between dams and pocket, is measured less accurately at 19.1 μm with a standard deviation of 4.0 μm per actuator. Using a high-speed camera and open source video analysis, angular accelerations up to 7.4 rad/s^2 and angular de-accelerations up to 14.7 rad/s^2 are measured. Friction between limit stops and actuated object is seen as the cause of the difference between accelerations and de-accelerations. Assuming that averaging the angular accelerations and de-accelerations compensates for the friction, 67% of the numerically obtained angular accelerations is achieved. Taking into account a possible off-centre placement of actuators this is a high percentage. Next to the inaccuracies of the measurements, the comparison is subjected to other inaccuracies, such as manually set pressure levels, varying inlet restrictions, and the implementation of flat surfaces in the model as well as the assumption of parallel pin surfaces, top and bottom plates in the model.

To conclude, this research started with an objective to explore the outlet restriction variation for contactless positioning of thin substrates using a thin air film for actuation and levitation. The general conclusion is that the outlet restriction is a viable and promising concept. After four phases of research involving concept exploration, actuator design, design realisation and experimental validation, benefits were seen compared to the state of the art in manufacturability and vacuum flow losses. Moreover, benefits in terms of bandwidth are expected, but not verified.

Contents

1

Introduction

1.1. Research context

1.1.1. Photovoltaics

Global warming pushes industry to develop cleaner and cheaper alternative energy sources. One of these sources is solar energy, which has made giant improvements the past decades. Efficiency has risen and production costs dropped, which resulted in a lower price for solar energy. The price of solar cell energy has dropped from more than 76 USD per watt in 1977 to less than 0.75 USD per watt in 2013, see figure 1.1. In 2006 Swanson [27] concluded that over a period from 1979-2005 module prices have dropped 20% for every doubling of cumulative volume. This observation is called Swanson's law in the photovoltaic (PV) industry, similar to Moore's law in the chip industry. However, recent price trends of PV systems in Germany, one of the front runners in terms of solar energy implementation [20], show a stagnation in price reduction over the past years, see figure 1.2.

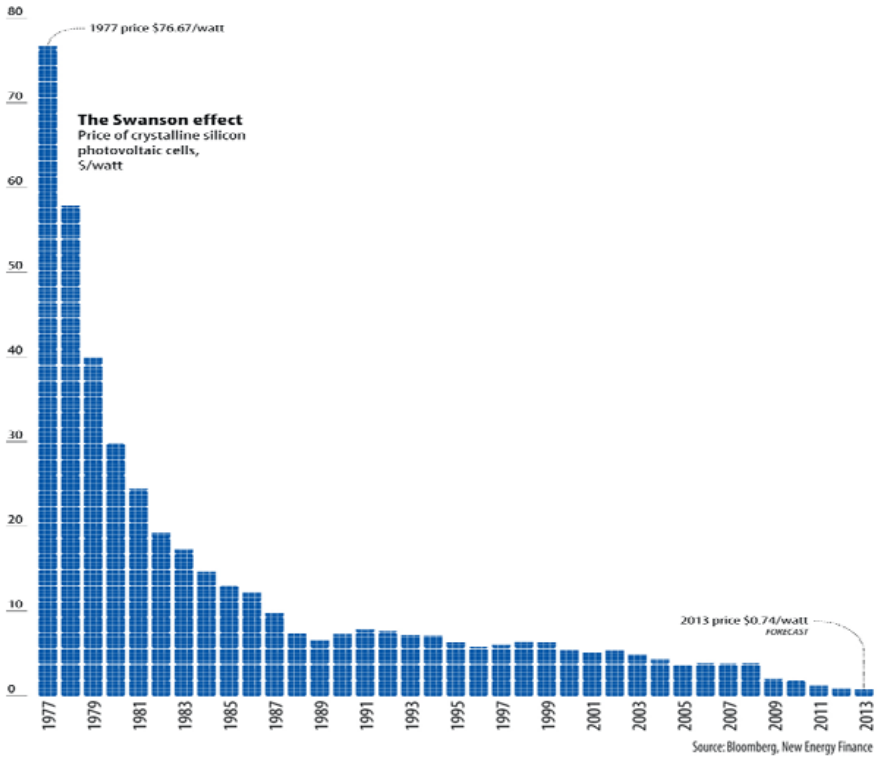

Figure 1.1: Solar cell energy price per Watt in USD from 1977 to 2013 [9]

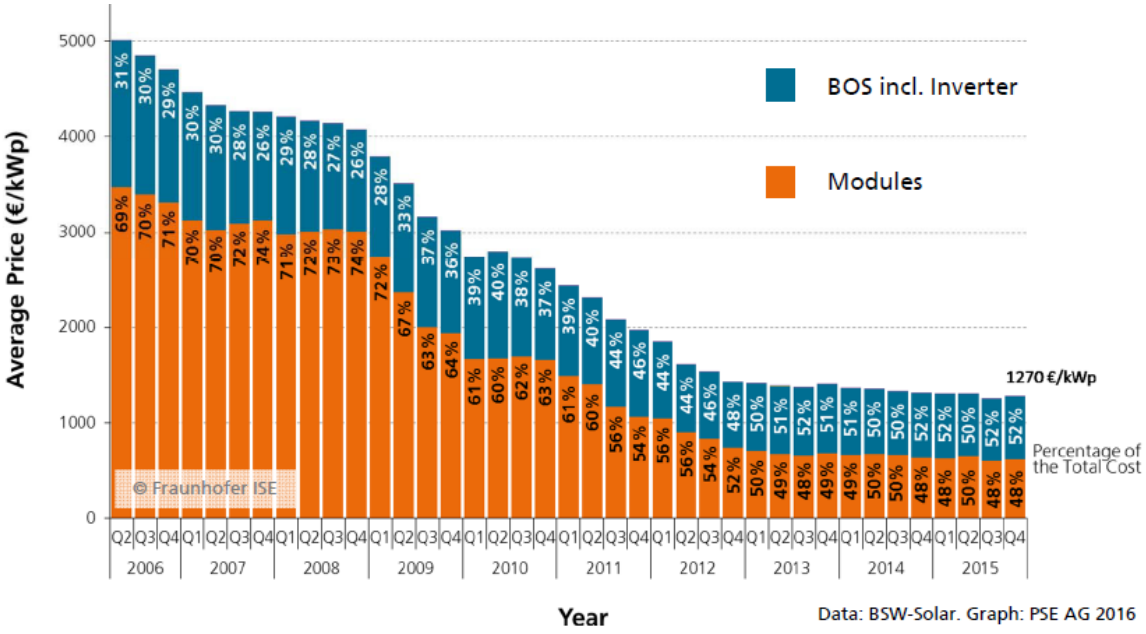

Figure 1.2: Average price for PV rooftop systems Germany (10kWp-100kWp) [25]

Many factors have played a role in the price reduction per energy quantity, such as the increasing size of plants, efficiency of the modules, wafer size and the usage of polycrystalline silicon [23]. Another option to reduce solar cell prices would be to use less silicon. Although the base material for silicon is sand, production of very pure silicon required for PV application is costly and adds up to 20% of the cost price for a PV module made in China, the largest solar panel manufacturer in the world [22]. A reduction of silicon usage can be achieved by reducing kerf widths of the cutting process or via a reduction of the thickness of the solar cell itself. The latter option has been stagnated the last years, see figure 1.3.

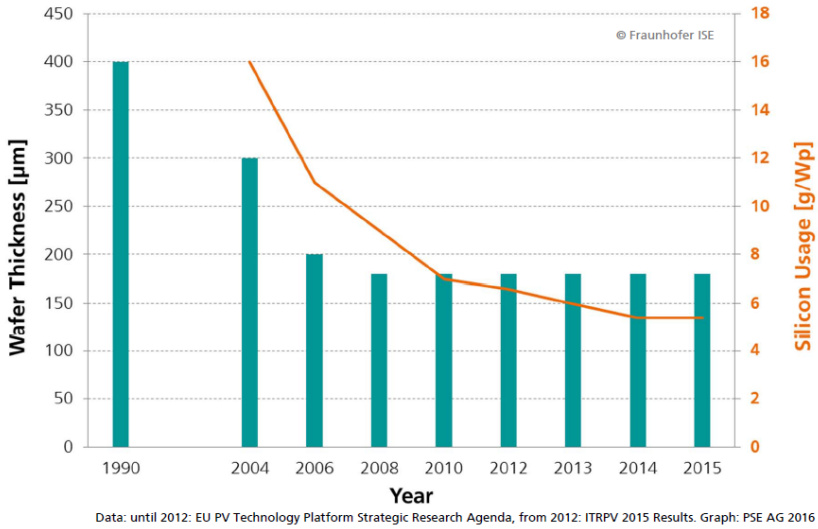

Figure 1.3: Wafer thickness [μm] and silicon usage [g/Wp] [25]

Manufacturing of thinner wavers is not a problem, since researches have come up with new methods to grow silicon foils, rather than cutting slices from an ingot [21, 24], which leads to the fact that a lot of silicon is machined into dust. The difficulties however lie in processing those very thin and therefore fragile wavers, [13, 16], breakage rates up to 96% have been reported for the handling of 70 μm thick substrates in a semi industrial process [3].

1.1.2. Contactless handling

It looks like the traditional mechanical handling of wafers has reached its limits and therefore this research has been focussed on exploring new concepts to handle/transport/position wafers without mechanical contact, i.e. contactless. Research into contactless handling started with the desire to reduce and eliminate friction between two solids. The absence of friction lowers wear and actuation forces, moreover it does result in the absence of stick slip behaviour as well, which is beneficial for the precise positioning of objects. In the photo voltaic industry contactless handling can also be used to reduce the risk of contamination due to mechanical contact. The removal of mechanical contact in the photo voltaic industry is the main driving force of this research, since it can reduce breakage rates of thin solar cells. The contactless technology should ultimately be able to replace the conveyor belt in the industrial process, see figure 1.4.

Figure 1.4: Contactless conveyor belts could replace the traditional mechanical conveyor belts.[1]

Contactless handling of objects can be divided in two main function. First of all, the object should be lifted, this is called the bearing function, a force larger or equal to the gravitational force is necessary to eliminate the contact with the surroundings. Secondly, after lifting the object, it should be actuated, which is called the motor function. To replace the conveyor belt in figure 1.4 an actuator is pursued in this research that combines the bearing and motor function, moreover actuation in all planar directions is pushed for. Contactless handling has been achieved using different principles, an overview has been sketched by Vuong [39], a short summary will be given here, for more details the author refers to the report of Vuong.

Electromagnetic force is a contactless force that is used widely in the field of contactless handling. An electromagnetic force is created due to interaction between electric and magnetic fields. Electromagnetic forces are mostly limited by the thermal dissipation of heat in the electromagnetic coils. Since this dissipation is normally rather high, high forces can be generated. However, there is one downside of electromagnetic forces and that is that the object to be handled should be made of ferromagnetic or electrically conductive materials, mostly metals fulfil this requirement. Since solar panels are made from silicon, this poses problems.

Electrostatic force is the next contactless force that will be discussed. It has first been discovered by Coulomb and it described as the force that electric charges exert on each other. Fully electro static handling systems have been built, however the forces that can be generated are rather limited. The levitating force is proportional to the surface area of the object, the actuator force however can only be generated at the edge of the object. Due to the limited actuator force for thin substrate and the fact that the forces are related to the conductivity of the material, silicon is a semiconductor, electromagnetic forces are left out as a suitable option to handle solar panels.

Ultrasonic vibrations have been used as contactless actuators in systems were the object to be handled is immersed in a fluid. Two working principles using ultrasonic vibrations can be distinguished. The squeeze film effect can only be used in a gaseous environment, since the compressibility of air plays a crucial role. Vibrating an actuator with a sufficiently high frequency, gives air no time to escape and a pressure is built up

[1] http://www.arabnews.com/node/1111161/business-economy

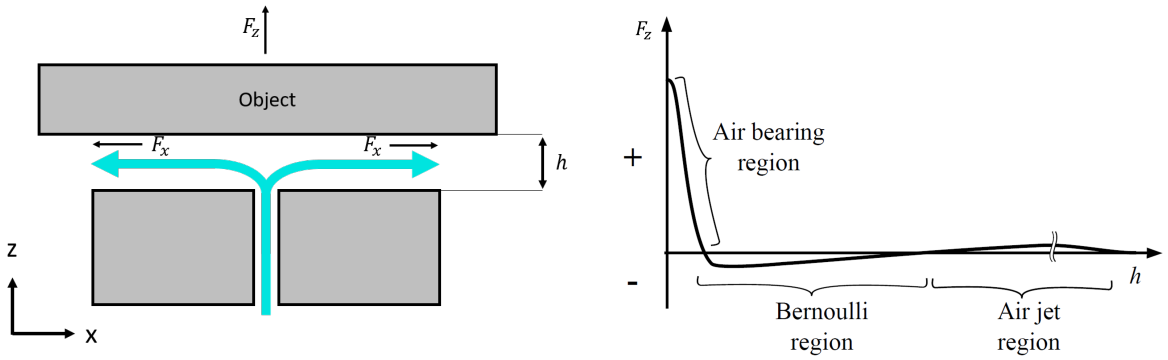

Figure 1.5: Contactless air flow forces.

between actuator and object. Generated forces can be enough to levitate thin substrates, however actuation will be difficult since this is limited to the sides of a solar panel.

The second contactless actuation method using ultrasonic vibration uses sound standing waves, air and liquid environments are suitable. Using a sound source and a reflector, standing waves can be created and maintained. The standing waves create a pressure distribution that is able to trap a lightweight flying object just below every pressure node. So far, this technology has only been able to lift weights of a few grams. Due to the limited forces that can be generated with both ultrasonic technologies, this technology will also not be pushed forward in this research.

Air flow is the final contactless force that is discussed in this section. With an air flow four types of forces can be generated, based on figure 1.5 three forces in vertical direction can be created and one force in horizontal direction. Operating conditions, especially the height of the air gap defines which vertical force will be generated. As said, Vuong has given an overview of these forces, however Snieder [33] made a more complete overview of the possible contactless forces created with air flow. The four possible forces will shortly be discussed here, starting with the vertical forces.

For very small air gaps the system behaves as an air bearing, the air flow becomes laminar and a pressure distribution will be present under the object. Integrating this pressure gives the load capacity of the air bearing, which can be very high since pressure levels can be increased. Stiffness is obtained with an inlet restriction, which is explained in more detail in chapter 2. However, high forces can be generated, these forces have only been used to handle the required levitating force.

As can be seen in the graph in figure 1.5, for increasing air gaps a negative force is generated. This means that although a pressure above ambient pressure is used a suction force can be generated, which means object can be lifted from the topside. The origin of the suction force is pressure reduction as a results of an increasing air flow, which is called the Bernoulli airflow principle. However, lifting is possible using the suction force, the motor function is difficult to solve using forces in the Bernoulli region.

Increasing the air gap even further the air jet region is reached. In this region the inertia forces of the air flow are dominant. These inertial forces can levitate and actuate an object as long as enough surface area is present. Forces are related to the mass flow per surface area, which means that high forces are related to high mass flows. Precise positioning is a challenge and actuating a thin substrate is hardly possible.

The last force generated by air flow is based on the viscous traction of air flowing along an object. In figure 1.5 the viscous force is shown as the horizontal force F_x. Although often neglected, this force has been used to actuate objects. An actuator with a smart position of in and outlets connected to high pressure and vacuum sources can be used to generate significant accelerations of thin objects, since the force is proportional to the surface area.

Due to the combination of low mass flows, obtained for smaller gap widths, and significant actuator forces it has been decided to pursue an actuator that levitates the object using a thin film, comparable to air bearings, and actuates the object making use of the viscous forces of the same air film. This is seen as the most promising concept due to the material and geometry of solar panels, which does have a large surface in combination with a limited thickness. The limited thickness and silicon as base material make actuation with other contactless actuators challenging. A requirement on the solar panels for the chosen concept is a flat surface, which is the case for most solar panels.

1.2. State of the art

A research group at the TU Delft has been focussing on the concept of levitating and positioning of a substrate using a thin air film. Research started in 2006 with an idea of R.A.J. van Ostayen. The idea was based on levitation and actuation of a wafer using the same air film. Levitation of the wafer is done using the principle of an air bearing and actuation is done using viscous traction of this air film. The simplest air bearing consists of a surface connected to an outlet and an externally pressurized inlet with a restriction, which has been observed in 1828 for the first time [28]. The restriction provides stiffness to the system which will be explained in more detail in section 2.1.1 of this report. An air flow will be generated between the in- and outlet, this flow follows a certain pressure distribution which is able to levitate an object. Note that the air bearing is externally pressurized and that no contact between bearing and substrate is present, contrary to an air cushion spring system, where air is trapped in an enclosed space.

The research group at the TU Delft discovered that if one could control the air flow in such a way that the flow is not equally distributed a net force can be exerted on the flying object. This force originates from the viscous traction between air flow and substrate. Two concepts have been explored and delivered working mechanisms, these will be discussed in the next sections.

1.2.1. Gen-1: Pressure variation

The first air based planar actuated contactless stage was presented in 2011 [40]. It was based on a static geometry and rapidly controlling air flow with valves below the actuator surface. A schematic view of the basic principle of the actuator can be found in figure 1.6.

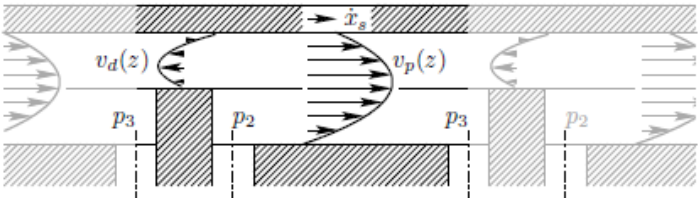

Figure 1.6: Basic principle of contactless actuator [40].

In figure 1.6, pressure p_2 is above ambient pressure and pressure p_3 below. This results in two air flows from which a velocity profile is sketched. The mass flow and flow velocity in the pockets (v_p) is higher than the flow and velocity over the dams (v_d), since a lower restriction is present for the pocket flow. Viscous forces on the substrate are related to flow velocity, which means that the actuator presented in the figure 1.6 creates a net force to the right on the levitated substrate. By placing many of these actuators in a grid with a varying direction an actuator can be made which controls all planar movements, see figure 1.7. Four inlets are connected to a controlled variable pressure (p_{21}, p_{22}, p_{23} and p_{24}) higher than ambient and the outlets indicated with a minus sign are connected to a controlled variable vacuum pressure lower than ambient.

A contactless stage has been created based on these principles, an exploded view of this design, called the Waferstage, can be found in figure 1.8. A positioning bandwidth of 50 Hz was achieved with a servo error of 6 nm (1 σ). For point-to-point positioning accelerations of up to 0.6 m/s^2 and velocities of up to 30 mm/s have been achieved. A drawback of this design is the fact that the valves are placed relatively far from the surface, and therefore significant pressure noise in the control lines limits a higher bandwidth. The achieved performance is similar to the specifications of flat panel display production machines, which means that contactless positioning of a thin substrate using an actively controlled air film is a not only a promising concept for the solar panel industry.

1.2.2. Gen-2: Deformable surface

In 2011 a research has been started at the TU Delft to explore new potential concepts [39]. It was realized that actuation close to the surface was required and therefore Vuong has chosen a concept based on a deformable surface. This means that variations in air flow restriction are created on the surface itself, which gets rid of pressure noise in the control lines which enables a higher bandwidth. A schematic drawing of this principle can be seen in figure 1.9. The flower lookalike structures, are suspended in two membranes such that the flowers can be tilted by in plane movement of the membranes relatively to each other. In figure 1.9 the flowers are tilted, which results in a difference of air flow restriction for opposing air flows. Similarly, to the concept

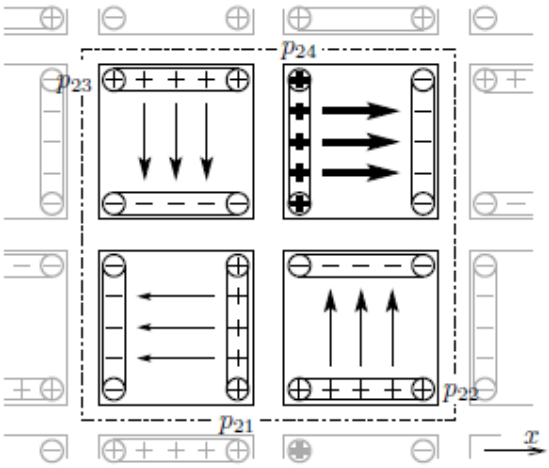

Figure 1.7: Configuration of multiple actuators, actuation to the right will be initiated with the sketched pressure levels [40].

in generation 1 this can create a net viscous friction force on a substrate which is levitated above the flowers, in this case to the right.

Based on this concept, 61 flowers were made and placed in the same plane, resulting in the so called "flowerbed", see figure 1.10. The theoretical bandwidth between actuating the membrane and the generation of a planar force on a levitated substrate is around 1000 Hz. Due to practical limitations, the bandwidth has been verified op to 400 Hz, which is a large improvement compared to the first generation. Krijnen created electromagnetic actuators and a fractional order control system to create the required in plane movement of the membranes [17]. A control bandwidth of 60 Hz has been achieved which was less than aimed for. The main reason for this is probably the added mass of the electromagnetic actuators and the rather low response time of these actuators. Current research is done to increase the bandwidth using other actuators mechanisms. Accelerations have been achieved op to 1.17 m/s and a positional accuracy of 104 nm (2σ).

Although the flowerbed has not reached its full potential yet, the bandwidth is already higher than the first generation contactless actuators. A drawback of the flowerbed is its manufacturability. It appeared to be challenging to reach the required flatness of the surface, a reason for this is the fact that the flowers are suspended in between two frames. Moreover, every flower is made of 5 parts, subtle variations in one of these parts leads to pretension in the system and tilting of the flowers.

1.2.3. Generation comparison

The performances of both generations have been listed already. However, in this section a comparison will be made with respect to the underlying manipulation principle. This will be done using a schematic diagram, since the used pneumatic components can easily be coupled to an electrical counterpart. Air flow can be compared to current flow, which is driven by a pressure that is linked to the voltage potential. Then, Ohms law for electrical resistances can be used for the restriction of air flow. This means that both generations of contactless actuators can be explained using figure 1.11. The pressure and vacuum source are both connected to ambient pressure and the usage of the different restrictions will be explained per concept by making a virtual round starting from the pressure source. Please note that any leakages present from either p_+ or p_- to ambient have been left out in this figure.

Wesselingh used the variable resistance, named 'pressure regulator' in figure 1.11, to control the control pressure P_c. By controlling this pressure, the airflow in a single actuator is controlled. An inlet restriction close to the surface creates stiffness. A surface restriction is also present since the flying substrate floats on a thin layer of air. Since this layer is in the order of tens of micrometres this causes a restriction. Since the outlet restriction adds negative stiffness, this restriction has been minimized.

In the deformable surface concept, a constant and negligible pressure regulator restriction is used. The inlet restriction provides the required stiffness in this concept as well. As explained, Vuong used the tilting flowers to control the direction of the air flow, this means that a variable surface restriction is implemented. The dimensions of the outlet restriction have been chosen such that the restriction is minimized, in the conceptual analysis it has been neglected.

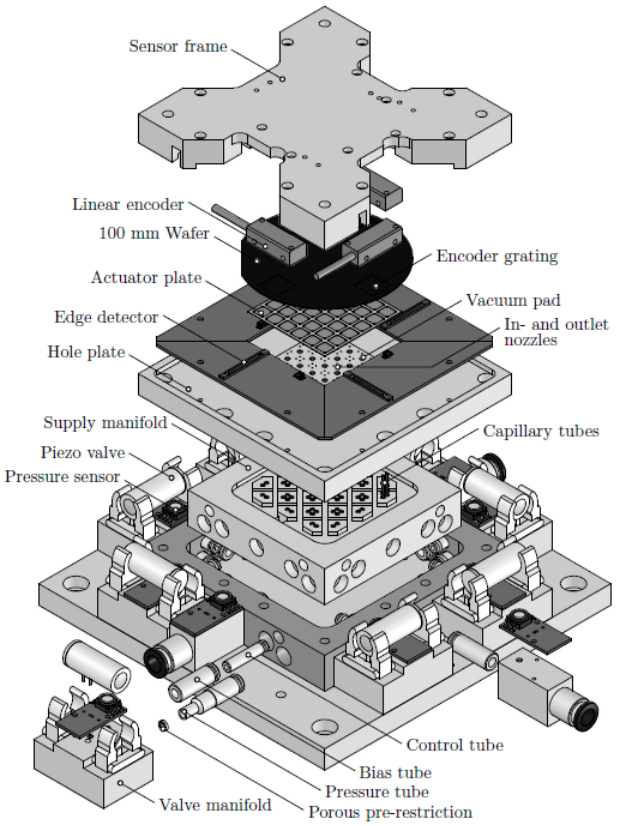

Figure 1.8: Exploded view of the contactless Waferstage setup [40].

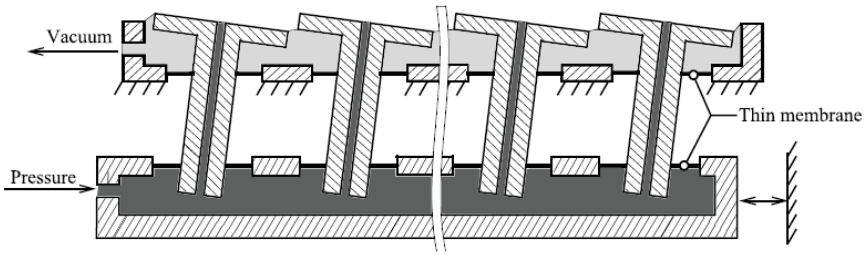

Figure 1.9: Deformable surface concept: tilted flowers [39].

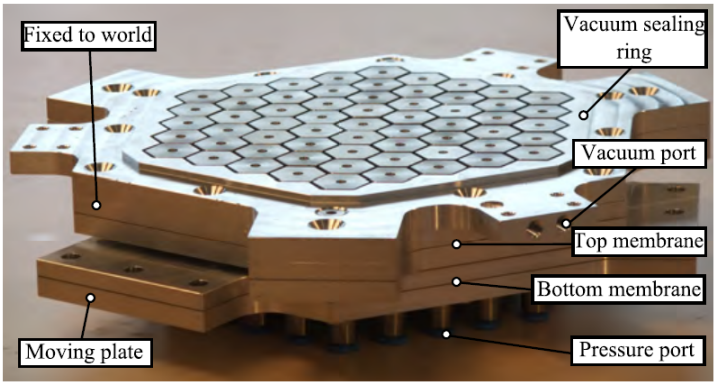

Figure 1.10: Constructed flowerbed [39].

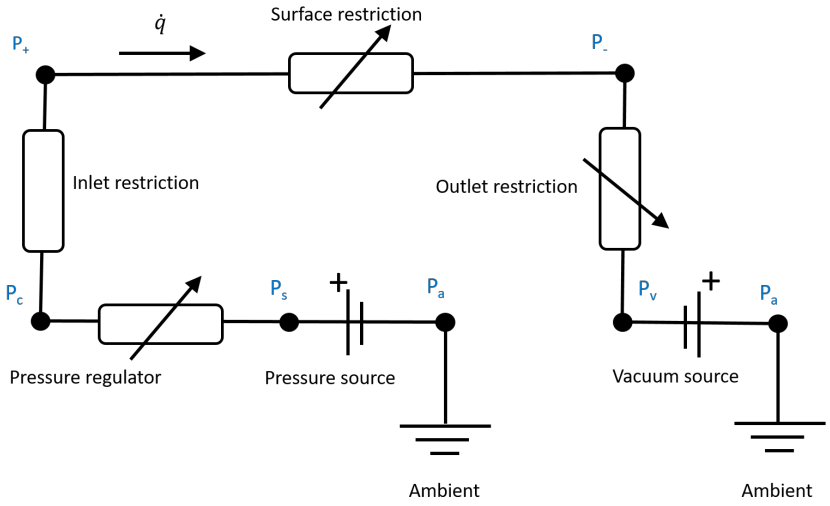

Figure 1.11: Representation of a contactless actuators using electrical schematic symbols

1.3. Research objective

As mentioned in the foregoing sections it is clear that industry would welcome new solutions to levitate and position thin substrates using air bearing technology. Although the previous concepts have proven that the concept of levitating and actuating using the same air film is possible, some shortcomings are present in the current solutions. Pressure variation, using valves, turned out to be too slow with respect to bandwidth, due to the distance between the valves and surface. Research to make micro valves, which could be placed close to the surface is ongoing, some preliminary results can be found in [6]. The deformable surface concept was hard to fabricate and the theoretical maximum has not been validated yet, which is ongoing as well. Moreover, a disadvantage of both concepts is that the outlet restriction is minimized, leading to the spilling of vacuum flow in case of absence of a levitated object. For these reasons, this research has been started to increase the knowledge with respect to contactless handling using a thin air flow and focusses on a new concept, with potential benefits in terms of bandwidth, manufacturability and vacuum flow spillage. This concept is based on the variation of the outlet restriction in figure 1.11. This means that instead of the pressure regulator or surface restriction the outlet restriction will be varied to create a net air flow and a propulsion force. Since this has not been done so far, the goal of this research is chosen to be:

To explore the outlet restriction variation for contactless positioning of thin substrates using a thin air film for actuation and levitation.

The performance of this concept will be measured based on the following indicators:

- Force over mass flow $\left[\frac{\mathrm{N}}{\mathrm{kg/s}}\right]$
- Near/in surface actuation
- Manufacturability, which can be measured by the number of parts and production steps.

1.4. Report outline

This remainder of this report focusses on the modelling, designing, manufacturing and experimental validation of the outlet restriction concept. The Reynolds equation is introduced in appendix A. The stepped tilted surface concepts will be investigated and compared with the new outlet restriction concept in a two dimensional analysis. The next chapter discusses the three-dimensional design of the outlet restriction variation. Different restrictions as well as geometries are discussed. The next chapter discusses potential manufacturing methods. The chosen manufacturing procedures are explained. Finally, the created setup is experimentally tested and the results are compared with the numerical model.

2

Concept exploration and comparison

The general working principle of an air bearing, the pressure variation concept and the deformable surface concept have been discussed in the introduction. These will briefly be reinterpreted in this chapter, moreover the new outlet variation concept will be introduced in more detail. Analytical equations, which describe the behaviour of the different concepts, will be derived and compared. The basis of most derivations starts with the Reynolds equation. The origin and assumptions made to derive the Reynolds equation starting from the Navier Stokes equation are given in appendix A. Although the Reynolds equation for a three-dimensional analysis is given, in this chapter it will be simplified for usage in a two-dimensional analysis. The chapter starts with the analysis of the bearing and motor function for a simple air bearing.

2.1. Simple air bearing

Let us discuss the simple two-dimensional externally pressurised air bearing shown in figure 2.1. As can be seen the fly height h is constant. If we furthermore assume that the pressure difference is relatively small compared to the ambient pressure, the air can be assumed to be incompressible. This means that the general Reynolds equation can be simplified after removing the constants which are independent of x, to:

$$\frac{\partial^2 p}{\partial x^2} = 0 \tag{2.1}$$

This can be solved by integrating twice over x. With the boundary condition of p_+ at the inlet and p_- at the outlet a pressure distribution that is a linear decay from p_+ to p_- will be found for both sides. However, the pressure differences are most likely not small compared to the ambient pressure, which has also been discussed by [39]. This means that the incompressibility assumption is not valid any more, which complicates the differential equation, since the density can no longer be assumed constant. Assuming an ideal gas, the density can be described with $\rho = p/R_g T$. After removing the constant components, the differential equation to solve becomes:

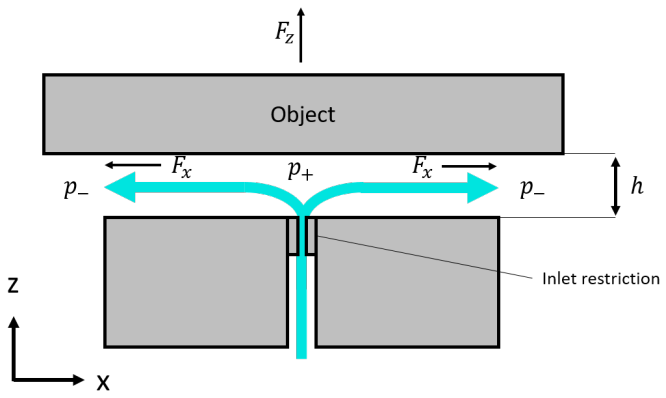

Figure 2.1: Simple air bearing with inlet restriction.

$$\frac{\partial}{\partial x}\left(p\frac{\partial p}{\partial x}\right)=0 \tag{2.2}$$

Although slightly more complex to solve than the incompressible variant, this can also been done analytically by integrating twice. One finds the following pressure distribution for the right side of the simple air bearing, with $x=0$ at the inlet, using the boundary conditions p_+ at the inlet and p_- at the outlet:

$$p(x)=\sqrt{\frac{p_-^2-p_+^2}{L}x+p_+^2} \tag{2.3}$$

Length L is taken as the distance from inlet to outlet. Based on equation 2.3. pressure distributions for different pressure differences between in and outlet can be created. By subtracting p_- from the total pressure distribution and afterwards dividing by the pressure difference, the pressure in the gap can be normalized, which means that different pressure differences can be plotted in the same graph, which is done in figure 2.2. The influence of the assumption of compressibility can be seen. A higher pressure difference between in and outlet results in a larger deviation from the incompressible line. Since the pressure differences in common air bearings are quite high nowadays, the assumption of incompressibility will lead to errors. Although not always correct, the assumption will sometimes be used in this report to simplify derivations.

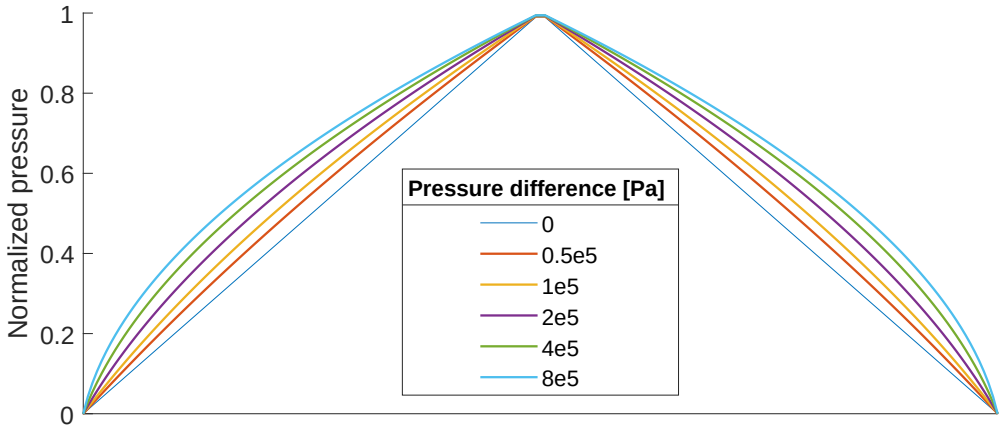

Figure 2.2: Normalized pressure distribution for different pressure differences

2.1.1. Bearing function

The load capacity F_z of an air bearing can be found by taking the integral over the surface of the pressure distribution. For the two-dimensional example, the next formula can be used to find the vertical force density:

$$\overline{F_z}=\frac{1}{L}\int(p)dx=p_{avg} \tag{2.4}$$

The average pressure for an incompressible medium is just simply the average between the in and outlet pressure. For a compressible situation, the average pressure can be derived, see equation 2.5. This equation shows that the assumption of incompressibility induces larger errors for larger pressure differences, which can also be seen in figure 2.2; a higher pressure difference leads to a higher normalized average pressure.

$$p_{avg}=\frac{2}{3}\frac{p_+^3-p_-^3}{p_+^2-p_-^2}=\frac{2}{3}\left(\frac{p_+^2}{p_++p_-}+p_-\right) \tag{2.5}$$

For both the compressible and incompressible situation the average pressure at the surface lies within the pressure levels at the in and outlet. However, trivial, an important conclusion can be drawn from this reasoning, since every air bearing is made for a certain load. This means that in case of a high load per surface area, it is wise to increase the pressure levels to obtain a high average pressure. In case of a very thin film (e.g. solar cell) the load is negligible meaning that a pressure below ambient pressure should be chosen for p_-. Since this report focusses on the handling of thin films, a vacuum source has to be connected to the

outlets. Moreover, in the remainder of this chapter a zero load condition will be applied to compare different bearings. This condition ensures that the average pressure above and below the object to be carried is equal, meaning that the weight of the object is neglected. Since the objects are thin substrates, this gives reliable results, moreover computation can easily be compensated with an offset on the ambient pressure for larger weights.

Next to a certain load capacity generated by the pressure distribution a reasonable stiffness is required for proper functioning of bearings. Stiffness per surface area in the out of plane direction k_z can be defined using the load capacity:

$$\overline{k_z} = -\frac{d\overline{F_z}}{dh} = -\frac{dp_{avg}}{dh} \tag{2.6}$$

This means that a positive value for the stiffness k_z is desired, since an increase of the fly height should result in a decrease of the load capacity and vice versa. To explain how stiffness is realised and to derive easy understandable equations, the assumption of incompressibility will be made. This means that a schematic diagram using electrical symbols can be used. The simple air bearing shown in figure 2.1 can be compared to an electrical system with three resistances in series. Pressure can be compared to the electrical potential in such a system, the current relates to the air flow and the electrical resistance can be coupled to the air resistance. Although no outlet resistance is present in a simple air bearing, it will be taken into account, since it is interesting to know what influence the outlet restriction has. Zooming in on the right side of the simple air bearing an electrical schematic drawing can be made, which is shown in figure 2.3. Since the actuator is symmetric, a similar electrical drawing can be made for the left side, which means that the stiffness per unit area will be equal for both sides.

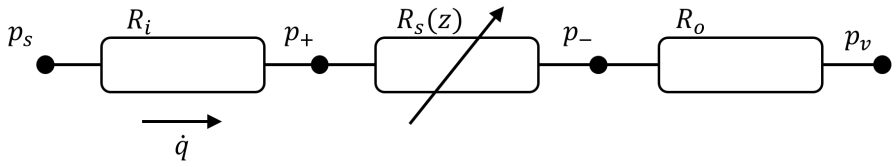

Figure 2.3: Simplified electrical overview, air flows from the pressure source p_s through the inlet, surface and outlet restriction.

The resistance to air flow of a two-dimensional air gap can be expressed using the fly height, viscosity and length of the gap:

$$R_s = \frac{12\mu l}{h^3} \tag{2.7}$$

Assuming a linear relation between air flow and pressure difference over the in and outlet resistance the following system of equations can be created.

$$p_s - p_+ = \dot{q}R_i \tag{2.8}$$
$$p_+ - p_- = \dot{q}R_s(z) \tag{2.9}$$
$$p_- - p_v = \dot{q}R_o \tag{2.10}$$

Note that the volume flows in these equations are equal due to the assumption of incompressibility. In a compressible situation the volume flow changes with the pressure level, in this case the mass flow is equal at all locations and the pressure levels have to be squared to obtain a correct system of equations. In this analysis however, the assumption of incompressibility has been made, which makes the electrical diagram more intuitive. All restrictions are placed in series, this means they can be added:

$$\dot{q} = \frac{p_s - p_v}{R_i + R_s(z) + R_o} \tag{2.11}$$

With p_s and p_v known the next formulas can be derived

$$p_+ = \frac{p_v R_i + p_s(R_s(z) + R_o)}{R_i + R_s(z) + R_o} \tag{2.12}$$

$$p_- = \frac{p_v(R_i + R_s(z)) + p_s R_0}{R_i + R_s(z) + R_o} \tag{2.13}$$

With formulas for p_+ and p_- in terms of the resistance and known source and vacuum pressure the stiffness can be derived. Since the assumption of incompressibility has been made the average pressure at the surface is equal to the average of p_+ and p_-. Taking the derivative of this average pressure with respect to the fly height gives the stiffness:

$$k_z = -\frac{d}{dz_s}\frac{p_+ + p_-}{2} = -\frac{d}{dz_s}\frac{(p_s + p_v)R_s(z) + 2p_s R_o + 2p_v R_i}{2(R_i + R_s(z) + R_o)} \tag{2.14}$$

thus

$$k_z = -\frac{R_s'(z)(R_i - R_o)}{2(R_i + R_s(z) + R_o)^2}(p_s - p_v) \tag{2.15}$$

The derivative of the surface resistance R_s' is negative since this resistance decreases if the fly height increases. Moreover, it is clear that if the fly height remains constant the stiffness will increase if the pressure difference increases. To obtain the required positive stiffness, the inlet resistance R_i should be larger than the outlet resistance R_o.

An intuitive way of understanding why these resistances create stiffness can be explained looking at figure 2.3 again. Assume that the inlet resistance is higher than the outlet resistance and that the in and outlet pressures remain constant if the fly height changes. This means that the pressure difference over the in and outlet resistance will increase if the surface resistance lowers (increase in fly height), this is analogue to the potential ratios in an electrical circuit. So, p_+ decreases and p_- increases. Moreover, since the inlet resistance is larger than the outlet resistance the pressure over the inlet will increase relatively more than the pressure over the outlet. This results in a lower average pressure of p_+ and p_-, which lowers the fly height and explains the stiffness.

The assumption of incompressibility made it possible to derive equation 2.15. Without this assumption the equation will become more complex and less intuitive, however a higher in and outlet resistance will always increase and decrease stiffness respectively. Moreover, a higher pressure difference will always increase the stiffness as well.

2.1.2. Motor function

The bearing function of an air bearing has been explained, in this section the motor function of an air bearing will be investigated. Air flowing parallel to a surface exerts force on this surface due to viscous forces. The in-plane force density $\overline{F_x}$ on the substrate generated by the air flow in a two-dimensional situation can be found using the next formula:

$$\overline{F_x} = \frac{1}{L}\int_0^L \frac{h}{2}\frac{\partial p}{\partial x}dx \tag{2.16}$$

This result can be obtained by starting from integrating the shear forces over the relevant in-plane length.

$$\overline{F} = \int \tau dx \tag{2.17}$$

According to Newton's law of viscous flow for a Newtonian fluid, the shear force can be described:

$$\tau = \eta\frac{\partial u}{\partial z} \tag{2.18}$$

Assuming zero slip conditions on the bounding bodies, the velocity profile for a pressure driven flow (Poiseuille) can be stated as:

$$u(z) = \frac{z^2 - zh}{2\eta}\frac{\partial p}{\partial x} \tag{2.19}$$

The derivative of the pressure driven flow attached to the upper bounding body is stated below.

$$\left.\frac{\partial u}{\partial z}\right|_{z=h} = \frac{2z - h}{2\eta}\frac{\partial p}{\partial x} = \frac{h}{2\eta}\frac{\partial p}{\partial x} \tag{2.20}$$

Inserting this in equation 2.18 and the result in equation 2.17 gives equation 2.16 after dividing by the actuator length L. Applying this formula on the simple air bearing (figure 2.1) it can be found that zero in-plane force is generated. This makes sense since the left half of the bearing creates a viscous force to the left which is equal but in opposite direction to the force to the right, created on the right side. It can also be proven that the force equals zero independent of the position of the inlet, assuming constant fly height and pressures on the in and outlet. This means that, although $\partial p/\partial x$ changes with a different position of the inlet, the in-plane force will not change.

Based on equation 2.16 two options are left to create a net in-plane force. First of all, a combination of different in and outlets supplied with different pressure levels can be used. For example, a lower pressure on the left outlet with respect to the right outlet will result in a force to the left. The second option is to apply a non uniform fly height. A larger fly height on the right side compared to the left side, will lead to a force to the right, which can be understood by the higher flow velocities as a result of lowering the resistance.

2.1.3. Performance

In the next section the stepped surface, tilted surface and outlet restriction variation concept will be compared in terms of performance. The performance of the active air bearings will be compared using two indicators. First of all, the **performance ratio** of the concepts will be compared. The performance ratio is defined as the force density over the mass flow density. The second indicator is the **performance limit**, which is defined as the maximum force that can be generated for a given mass flow. In the analysis that follows it will become clear that both concepts do not have a similar optimum. The performance limit can be found by optimising the force density squared over the mass flow density. The mass flow density of an actuator can be derived using the resistance equation for thin film flows and the pressure gradient, see equation 2.7.

$$\overline{\dot{m}} = \frac{1}{12\mu L}\rho\left(h^3\frac{\partial p}{\partial x}\bigg|_l - h^3\frac{\partial p}{\partial x}\bigg|_r\right) \tag{2.21}$$

This is a summation of the flows flowing to the left and to the right taken at the inlet. The pressure at the inlet is known (p_+), this means that the density at the inlet can be described using the ideal gas law, thus $\rho = p^+/R_g T$.

2.2. Active air bearing

In this section, all pressure distributions have been obtained with the same load condition, namely a zero load condition, which is adopted due to the limited thickness of the substrate. Moreover, a minimum fly height h_0 is assumed throughout this section. The static performance of contactless actuator principles will be discussed. First a general introduction and the corresponding actuator geometry is given.

An analysis is done of three types of actuators: the stepped surface actuator, the deformable surface and the outlet restriction concept. The geometries of the three concepts will be introduced first, afterwards pressure distribution are presented. Lastly the geometries will be optimised with respect to the performance ratio and limit.

2.2.1. Geometry

The **stepped surface** concept was presented in 2011 [40]. The actuator was based on the geometry shown in figure 2.4. The stepped surface of the air bearing ensures that an in-plane force can be generated to the right side, since air flows with a higher velocity along the substrate to the right compared to the velocity over the dam. The fly height above the dams is h_0, the fly height above the pocket is taken as a multiplication of h_0, such that it can be optimised independently of the fly height. The outlet restriction has a negative influence on the stiffness, therefore the restrictive value has been minimised such that it can be neglected. This means that the pressure at the outlet p_- is equal to the vacuum pressure p_v.

The second concept with a **tilted surface** was introduced in 2016 [39]. In some way, this concept is comparable to the stepped surface concept, since a different air flow resistance between the left and right sides of the outlet, forces air to flow to one of these sides, in figure 2.5 more air will flow to the left side. Again, this air flow will induce a net viscous traction which drags the flying membrane to the left side in this case.

The fly height h_0 is defined as the shortest distance between the actuator surface and the flying substrate. The distance between the lowest point at the actuator surface and the substrate has been defined as βh_0. The inlet is placed at a location αL from the right side of the membrane. However, in this study only the situation of α equal to 0.5, which gives a symmetrical situation, will be discussed. This means that tilting of the actuator

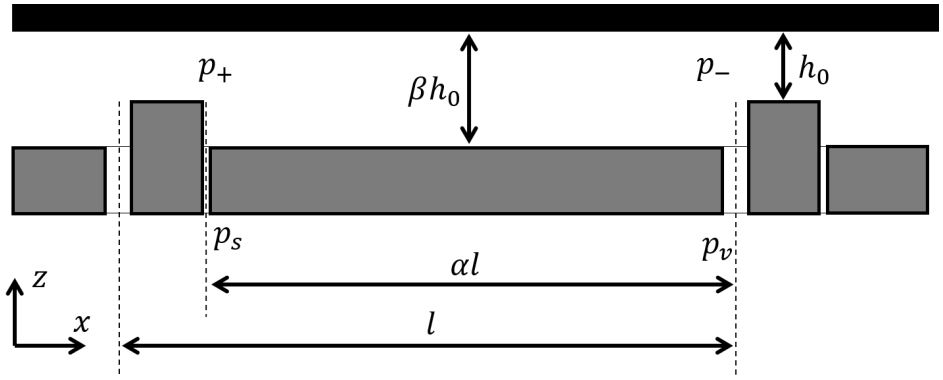

Figure 2.4: Actuator geometry of stepped surface concept [40].

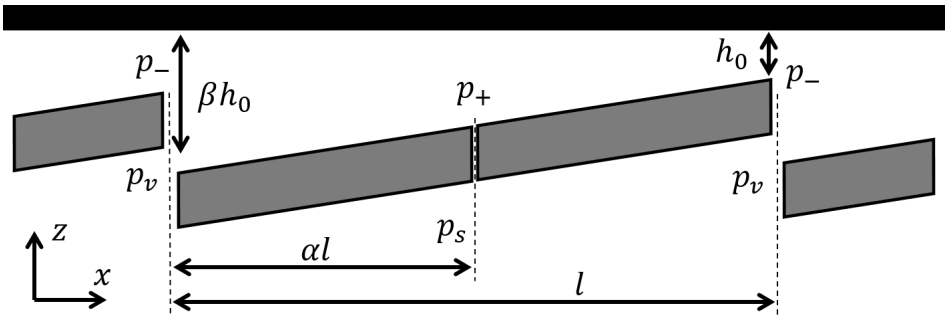

Figure 2.5: Actuator geometry of deformable surface concept [39].

results in similar actuation for both sides, which is handy since this two-dimensional analysis is the basis for a planar actuator. Moreover, the outlet restriction in this concept is very small, such that it is neglected as well. This means that the pressure at the outlet p_- is equal to the vacuum pressure p_v at both sides.

In this two-dimensional analysis, two one degree of freedom actuators have been seen so far. The tilted surface actuator however can actuate in both directions within this single degree of freedom, by tilting its surface around the y-axis. The stepped surface actuator requires a second actuator which is placed in the opposite direction to obtain this bidirectional actuation. Both concepts have been expanded to three-dimensional concepts for all planar directions, the stepped surface actuator required a configuration of even more actuators (figure 1.7) while a single tilted surface actuator was able to actuate in all planar direction. With the new **outlet restriction variation** concept, a single actuator is pursued that actuates in all planar directions.

In a three-dimensional setup, this leads to two options for the outlet restriction variation concept. First of all, a single inlet surrounded by multiple or a continuous outlet, analogous to the tilted surface configuration. A second option is a low pressure outlet surrounded by multiple or a continuous high pressure inlet. The first option is chosen due to the fact that vacuum pressure is limited at 0 Pa, which lowers the maximum pressure difference. The reason for this is that the actuator will be used for thin films which means that the average pressure should be around ambient pressure, moreover the pressure around the inlet determines a relatively small surface area compared to the pressure at the outlet. Reasoning further an outlet in the middle would lead to a relatively low pressure level at the surrounding inlet to obtain an average pressure equal to ambient pressure, meaning that a small pressure difference is present. A small pressure difference between inlet pressure p_+ and outlet pressure p_- leads to limitations in the force density, see equation 2.16. This will be avoided and therefore a concept will be pursued with a high pressure inlet in the middle surrounded by multiple or a continuous outlet restriction. In the two-dimensional analysis, this leads to an actuator configuration shown in figure 2.6. α and β are chosen similarly to the stepped surface concept.

The stepped and tilted surface actuators were both modelled with a negligible resistance at the outlet. This concepts however is based on a variable outlet resistance on both sides of the actuator. A comparable electrical schematic can be found in figure 2.7. Air flow starts at the pressures source with a pressure p_s and flows through the inlet resistance R_i and the actuator resistance R_a before it leaves the actuator through one of the two outlet restrictions. An elevation will be incorporated to separate two actuators, this is called the dam resistance R_d.

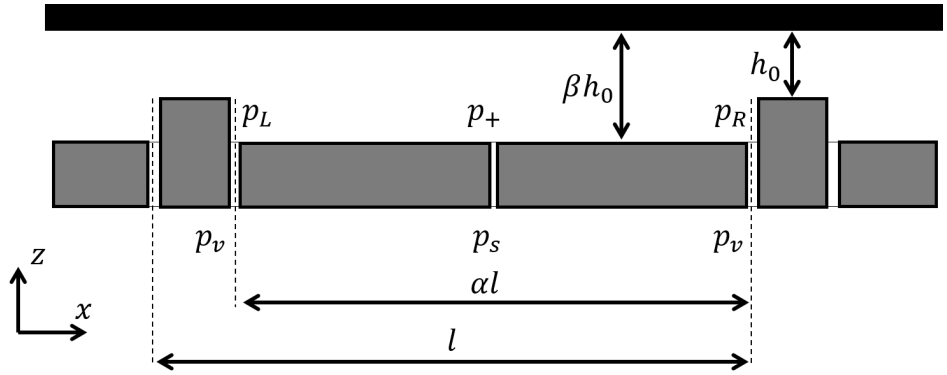

Figure 2.6: Geometry of the outlet restriction variation concept, α and β will be optimised.

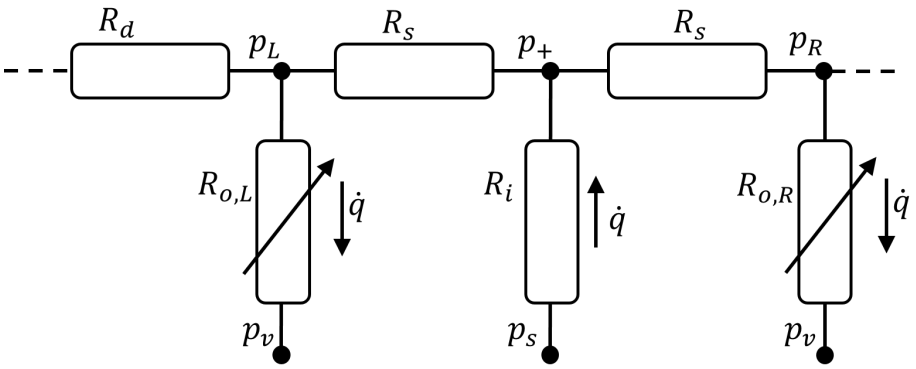

Figure 2.7: Representation of the outlet restriction variation concept using an electrical scheme

.

2.2.2. Pressure distribution

The pressure distribution of all concepts over the actuator surface will be derived in this section. The pressure distribution is interesting, since the actuator force and mass flow can be derived from a given pressure distribution, this can be done numerically and sometimes analytically. Leaving out all the constants independent of x, the compressible Reynolds equation that has to be solved for the **stepped surface** is equal to the simple air bearing:

$$\frac{\partial}{\partial x}\left(p\frac{\partial p}{\partial x}\right)=0 \tag{2.22}$$

Solving this similarly as for the simple air bearing, with the assumption of a negligible outlet restriction and the lowest vacuum pressure possible (0 Pa) for p_v, the pressure distribution can be found using the no load condition. Some pressure distributions have been plotted in figure 2.8 for different values of α, while β was taken constant. Note that the pressure at the inlet p_+ remains constant at 150 kPa due to the no load condition, which gives an average pressure equal to 100 kPa, indicated with the black dotted line. Equation 2.5 states that the average pressure is only depending on the in and outlet pressures for an air bearing with constant fly height. This means that the average pressure above the dam is equal to the average pressure above the pocket. Moreover, if one varies β while taking α constant, this will have no influence on the pressure distribution, thus equal p_+ and average pressure will be found.

For the **tilted surface**, the compressible Reynolds equation to be solved is given by equation 2.23. As can be seen, the fly height is not excluded from the equation, the reason for this is that the fly height is depending on the position.

$$\frac{\partial}{\partial x}\left(ph^3\frac{\partial p}{\partial x}\right)=0 \tag{2.23}$$

This equation can partially be solved analytically. The first step is integrating once and bringing the term with the film thickness to the right hand side, a second integration can be done afterwards. The boundary

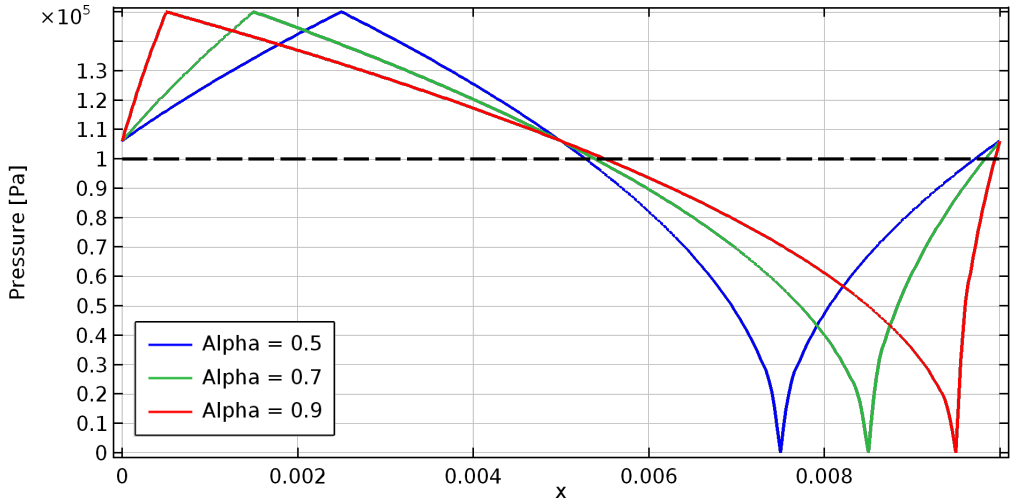

Figure 2.8: Pressure distribution of the stepped surface concept for different values of α. Varying β will not influence the pressure distribution found.

conditions are the no load condition and p_v at both outlets. Finally, the pressure distributions for different values of β have been found numerically, these are given in figure 2.9. All pressure distributions are created with the same no load condition.

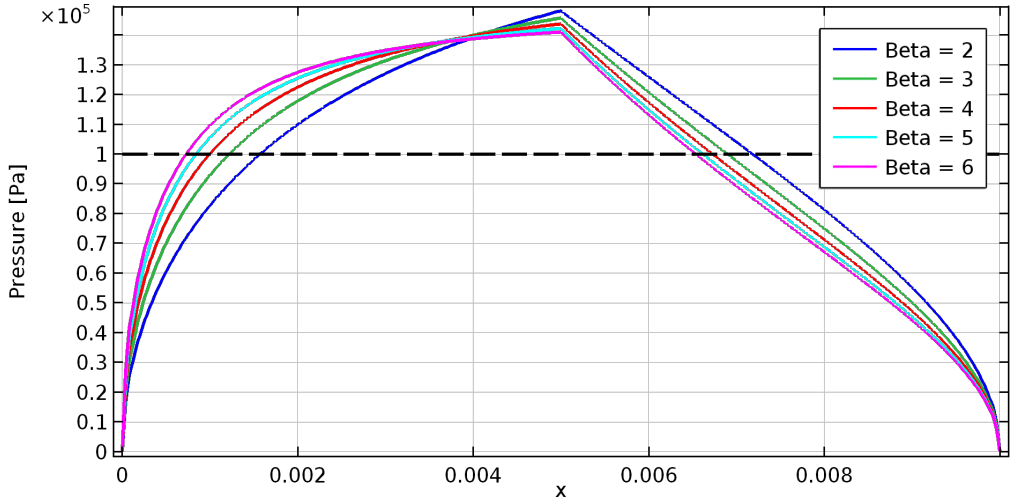

Figure 2.9: Pressure distributions obtained for the tilted surface concept for different values of β.

It is interesting to note that the pressure at the inlet varies for different values of β for the tilted surface, which is contrary to what has been seen for the stepped surface. This pressure varies to maintain an equal average pressure which defines the load capacity. In other words, the average pressure is depending on the value for β, contrary to the stepped surface.

For the **outlet restriction variation** concept, the Reynolds equation to be solved is again equal to equation 2.22. The pressure distribution over the dam and between in and outlets can easily be found if the pressure levels at the in and outlets are known. Equation 2.3, which describes the compressible pressure distribution for the simple air bearing with constant fly height, can be used as an indication. However, the pressure levels at in and outlet depend on the resistances and their ratios. This means an iterative procedure has to be used to find the pressure distribution, therefore this has been solved numerically. The numerical model has been solved in such a way that the load applied to the system is equal in all situations, again a no load condition has been used. In figure 2.10, some pressure distributions for different values of β are given for an arbitrary but constant outlet restriction. Moreover, the outlet resistance on the left is taken equal to the outlet resistance on the right.

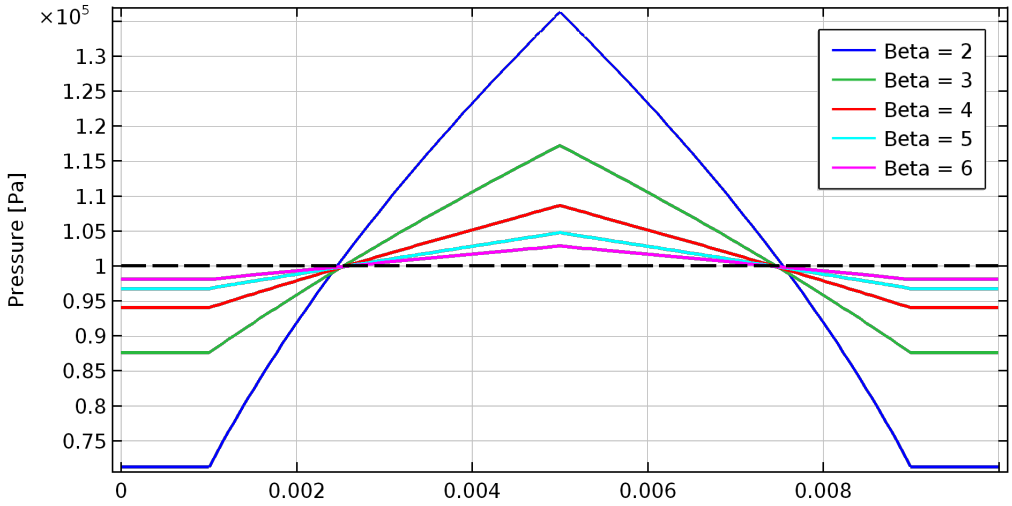

Figure 2.10: Pressure distributions for the outlet restriction variation concept with equal and constant resistances for $R_{o,L}$ and $R_{o,L}$. α is taken at 0.8 for all the pressure distributions, moreover the load is constant and the inlet resistance does not vary either. The pressure is constant over the dam, meaning no air flow is present.

Figure 2.10 shows a constant pressure over the dam. This means that the partial derivative $\partial p/\partial x$ is zero over the dam and no air flow is initiated. The pressure distribution in the pocket has an equal shape as the distribution found for the simple air bearing. On the other hand, the maximum and minimum pressure levels of the pressure distribution do differ quite a lot from the maxima and minima found for the stepped and tilted surface concepts. The reason for this is that the outlet restriction is not neglected and a pressure difference over the outlet is present. This pressure difference leads to a higher minimum pressure at the surface. Moreover, since the minimum pressure is higher the maximum pressure will reduce to satisfy the no load condition. Note as well that the pressure distribution is highly dependent on β. The reason for this is the ratio between outlet restriction and surface restriction, which changes as a result of changing β. A higher β results in a lower surface restriction and thus a smaller part of the total pressure difference between p_+ and p_v will be over the surface restriction.

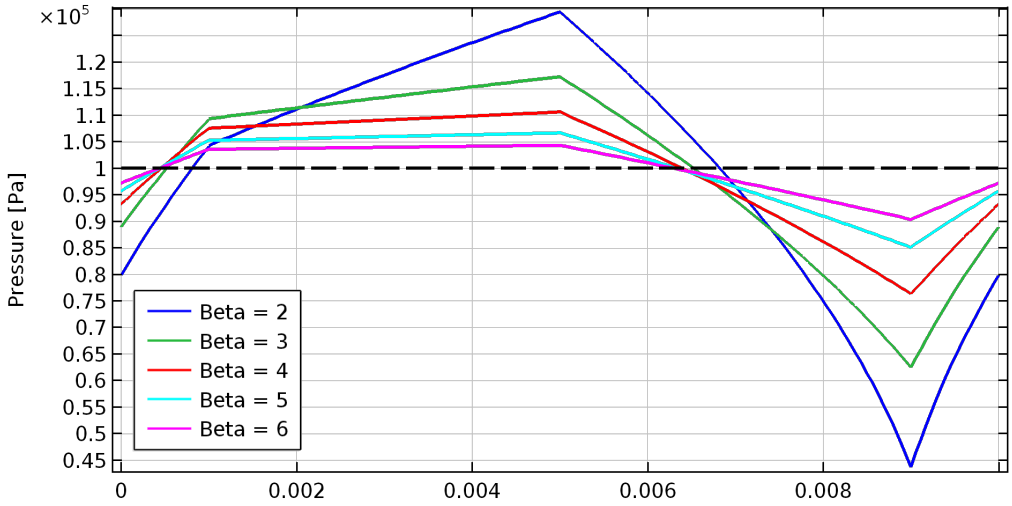

Figure 2.11: Pressure distributions for the outlet restriction variation concept with a $R_{o,L}$ that is 27 times larger than $R_{o,L}$. α is taken at 0.8 for all the pressure distributions, moreover the load is constant and the inlet resistance does not either. A pressure distribution is seen over the dam meaning an air flow is present.

Figure 2.11 shows the pressure distribution for a situation that the outlet resistances are not equal. The resistance on the right side $R_{o,R}$ is taken lower than the outlet resistance on the left $R_{o,L}$. The ratio $R_{o,L}/R_{o,R}$ is taken at 27 to create figure 2.11. A direct implication of this is a higher pressure difference between inlet and $R_{o,R}$ and a lower difference between inlet and $R_{o,L}$, which means a net air flow to the right since the actuator

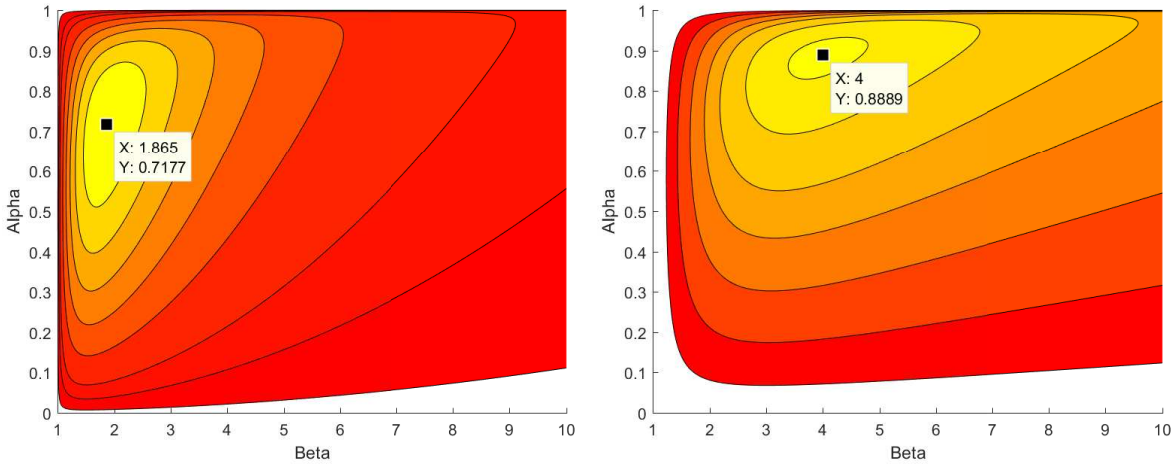

(a) Performance ratio

(b) Performance limit

Figure 2.12: Contour plots showing the optimal values for parameters α and β for the stepped surface concept.

resistance R_a is equal for both sides. Moreover, one identifies a pressure differential over the dam, which means air is flowing over the dam. This air flow is always opposing the net air flow and is therefore unwanted. Choosing α and β wisely helps to minimize this flow.

2.2.3. Performance

The next step is to find the optimal values for α and β. This means that preferably analytical equations must be found for the force and mass flow density. Using equation 2.16 and 2.21 this can be done for the **stepped surface** concept. The force density $\overline{F_s}$ and mass flow density $\overline{\dot{m}_s}$ for the stepped surface concept are found. The *performance ratio* η is defined as force density over mass flow density is also derived:

$$\overline{F}_s = \frac{(\beta-1)h_0(p_+ - p_-)}{2L} \tag{2.24}$$

$$\overline{\dot{m}_s} = \frac{1}{R_g T}\frac{h_0^3}{24\mu L^2}\left(\frac{1}{1-\alpha}+\frac{\beta^3}{\alpha}\right)\left(p_+^2 - p_-^2\right) \tag{2.25}$$

$$\eta = \frac{2R_g T}{p_+ + p_-}\frac{6\mu L}{h_0^2}\frac{\beta-1}{\frac{1}{1-\alpha}+\frac{\beta^3}{\alpha}} \tag{2.26}$$

Some interesting facts can be deducted from the performance ratio equation. The first term shows the influence of the compressibility. With the incompressible assumption in place, this term would simplify to 1 over the density based on the average pressure. Based on an equal load on the compressible and incompressible bearing, we can deduct that the first term in equation 2.26 is higher in case of compressibility. Moreover, the remaining terms in the performance ratio equation are equal, thus the performance ratio would decrease using the assumption of incompressibility.

The second term helps to predict the influence of fluid conditions, actuator length and fly height. It is clear that the performance increases with a larger actuator length L and a lower fly height. The fly height however will be limited by manufacturing tolerances and the actuator length will be bounded by substrate deformation, which will both be explained in later chapters.

The last term of equation 2.26 explains how α and β should be optimised to obtain the highest performance ratio. Figure 2.12a has been created to show the optimum, which has been found to be at approximately α equal to 0.72 and β equal to 1.9. This optimum will be the same for an incompressible situation, since the pressure levels are independent of α and β.

As explained, another way of looking at the performance of an actuator geometry can be done investigating the *performance limit*, which defines the maximum force density that can be obtained for a certain mass flow density, which is equal to minimizing mass flow density for a given force density. At the performance limit the lowest pressure possible will be taken for p_-, this means the outlet restriction will be taken so small

that it can be neglected. This results in a p_- which is equal to p_v. Pressure is naturally limited with 0 Pa as a lower bound, this means that for the performance limit p_- will be taken equal to this lower bound. Equation 2.5 can be used to determine p_+, since the average pressure will be taken equal to the ambient pressure due to the no load condition. Since p_+, p_- and the fly height h_0 are set, a required actuator length L^* can be defined using equation 2.16 to obtain a certain force density F^*.

$$L^* = (\beta - 1)\frac{h_0(p_+ - p_-)}{2\overline{F}^*} \tag{2.27}$$

Inserting this equation for the required actuator length in equation 2.25, gives the required mass flow:

$$\overline{\dot{m}^*} = \frac{p_+ + p_-}{2R_g T}\frac{h_0\overline{F^*}^2}{3\mu}\frac{\frac{1}{1-\alpha}+\frac{\beta^3}{\alpha}}{(\beta-1)^2}\frac{1}{p_+ - p_-} \tag{2.28}$$

Analysing equation 2.28 some familiar terms are present. The first term is the known density term, the second term describes the relation between mass flow, fly height, viscosity and the required force density. The third term states the influence of the actuator geometry and the last term indicates that a lower mass flow is required to obtain the same force density if the pressure difference increases. When minimizing this function with respect to α and β figure 2.12b can be created. It is clear that the optimum can be found if α is equal to 8/9 and β to 4. Maximizing the force density for a given mass flow density will result in the same optimum. Moreover, the optimum for the performance limit will be the same if a compressible model was used. The reason that for the performance limit different values for α and β are found compared to the performance ratio, is the fact that we are basically optimising to $\overline{F^2}/\overline{\dot{m}}$ compared to optimising for $F/\dot{m}$. This can be explained by recognising that the actuator length L, which has been substituted by a term depending on the force density, is present squared in equation 2.25. In section 2.3 the performance ratio and the performance limit curve of the stepped actuator will be compared to the other concepts.

For the **tilted surface** concept, a similar analytical derivation cannot be done, since the pressure distribution has not been obtained analytically. However, with a numerical analysis 2.13 was created. Both the performance ratio and limit are plotted. The *performance ratio* is optimal with β equal to 2. For an optimal *performance limit*, which means maximizing the force density squared over mass flow density, β should be taken equal to 5.

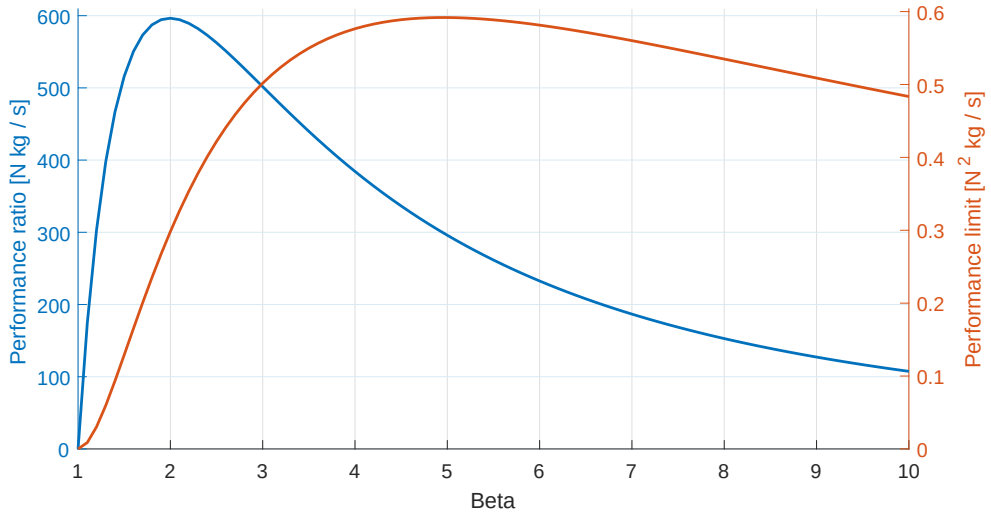

Figure 2.13: Performance ratio and performance limit plotted against β. A sensitive performance ratio can be found for a value of β equal to 2.0. A less sensitive performance limit is found for a value of β equal to 5.0.

The numerical analysis has been done based on the no load condition. If instead of a no load condition the inlet pressure (p_+) would be taken constant, the optimum for the performance limit would be found with β equal to 5.5. This value has been reported by Vuong [39] in chapter 2. However, a constant load capacity is regarded more important when comparing different configurations, therefore β will be taken equal to 5 for the performance limit curve comparison. Although the pressure distribution is more complex for the tilted

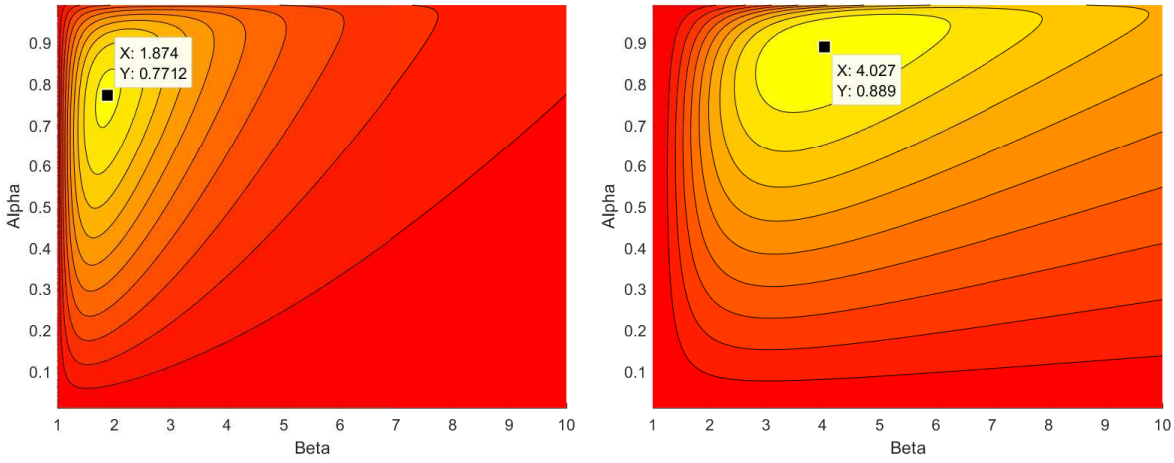

(a) Performance ratio

(b) Performance limit

Figure 2.14: Contour plots showing the optimal values for parameters α and β for the outlet restriction variation concept.

surface compared to the stepped surface and the inlet pressure p_+ is depending on the value chosen for β, the optimized performance ratio and limit will be found at the same values of β for the incompressible situation.

For the **outlet restriction variation** concept an analytical equation for the force density ($\overline{F_o}$) can be derived, this equation is depending on the pressures p_L and p_R, which can be found using an iterative procedure.

$$\begin{aligned}\overline{F_o} &= \frac{1}{L}\left(\frac{\beta h_0}{2}(p_+ - p_L) + \frac{\beta h_0}{2}(p_R - p_+) + \frac{h_0}{2}(p_L - p_R)\right) \\ &= \frac{h_0}{2L}(\beta - 1)(p_R - p_L)\end{aligned} \tag{2.29}$$

Using equation 2.21, the mass flow density can be found as well. The pressure gradient can be derived from the compressible pressure distribution obtained for the simple air bearing, see equation 2.3. The reason for this is that the simple air bearing has a flat surface around the actuator similar to the outlet restriction concept.

$$\begin{aligned}\overline{\dot{m}_o} &= \frac{1}{12\mu L}\frac{p^+}{R_g T}\left(\beta^3 h_0^3 \frac{p_+^2 - p_L^2}{p_+ \alpha L} + \beta^3 h^3 \frac{p_+^2 - p_R^2}{p_+ \alpha L}\right) \\ &= \frac{h_0^3}{12\mu L^2 R_g T}\frac{\beta^3}{\alpha}\left(2p_+^2 - \left(p_L^2 + p_R^2\right)\right)\end{aligned} \tag{2.30}$$

As can be seen both the force density and mass flow density are expressed in terms of the pressures at the outlets (p_R and p_L) instead of the vacuum pressure. The simple reason for this is that the outlet restriction cannot be neglected in this concept, since it is the variable restriction that will control the net air flow to the right and left side. However, based on the equation for force density, it can be stated that a larger difference between p_R and p_L leads to a higher force density.

Similar to the analysis of the stepped and tilted surface concepts, α and β will be optimised. However, first the ratio $R_{o,L}/R_{o,R}$ should be determined. Based on the equations for force density and mass flow, it can be derived that the difference between p_L and p_R should be maximized to a maximum performance ratio and performance limit. The largest difference between these outlet pressures will be found if the ratio $R_{o,L}/R_{o,R}$ is at an absolute maximum or minimum. In other words, one outlet restriction should be zero and the other restriction should be infinitely high, which means mass flows are respectively unconstrained and zero. An unconstrained mass flow means that the resistance can be neglected, so the pressure can be taken equal to p_v, which will be taken equal to 0 Pa to obtain performance limits.

Contour plots were created for the performance ratio and performance limit, these are given in figure 2.14a and 2.14b. Please note that the contour plots have been made based on a numerical model, so the plots

are not as accurate as the plots we have seen before which are based on analytical equations. The values found for α and β when the performance ratio force over mass flow is optimised are respectively 0.77 and 1.9 These values found are very similar to the results found for the stepped surface, see figure 2.12a. The value found for α is slightly higher for the outlet restriction concept. Comparing the two concepts this can be explained by looking carefully at both geometries. In case of actuation to the right side in the limit situation for the outlet restriction concept, which is studied in this section, the only difference with the stepped surface is a pocket on the left side of the inlet. This extra pocket creates extra resistance and therefore the dam can be taken smaller, which results in a higher value for α. For the performance limit however, the same optimum and contour plot has been found, in this case β should be taken equal to 4 and α equal to 0.89. Table 2.1 gives an overview of values found for α and β for all concepts and both performance indicators.

Table 2.1: Overview of optimal values found for α and β

	Performance ratio			**Performance ratio**		
	Stepped	Tilted	Outlet	Stepped	Tilted	Outlet
α	0.72	-	0.77	0.89	-	0.89
β	1.87	2.0	1.87	4.0	5.0	4.0

2.3. Comparison

In this chapter the basic principles of three potential concepts have been discussed on a theoretical basis, starting with the Reynolds equation. A simple air bearing and three active concepts have been discussed separately. In this section, the bearing and motor functions of these concepts will be compared.

2.3.1. Bearing function

The bearing function of an air bearing originates from the pressure distribution. Based on this pressure distribution an average pressure can be found which defines the load capacity. We have seen that for all three concepts the average pressure can be influenced by picking different source p_s and vacuum p_v pressures. This means that the load capacity can be tuned to quite a wide range of forces, meaning that based on the load capacity all three concepts can be rated equally.

Stiffness is another interesting factor regarding the bearing function of an air bearing. In section 2.1.1 an equation has been found linking the stiffness of a bearing to the resistances present in an air bearing. From pressure source to vacuum source, generally three resistances are present: An inlet resistance, surface resistance and an outlet resistance. It has been concluded that a higher inlet resistance increases stiffness and a higher outlet resistance lowers resistance. This means that in terms of stiffness the stepped and tilted surface concept are rated higher than the outlet restriction concept, since the latter one has an outlet restriction in contrary to the other two concepts. Although, the presence of an outlet restriction does lower the stiffness, it does not mean that the outlet restriction cannot be stiff, since a larger inlet resistance can be used to compensate. Reasoning further, a larger inlet resistance leads to a higher pressure source to obtain equal load capacity. Since air pressure is widely available this is not seen as an obstacle.

Moreover, the presence of the outlet restriction can actually also be seen as a benefit. The reason for this can be found by looking at the application of this concept in an industry environment. In the introduction, it has been discussed that this type of active air bearings can be used in solar cell production. A contactless conveyor belt can be made using active air bearings which do not damage or contaminate the solar cells. This means that the air bearing is not always covered by a substrate during operation. In this situation less vacuum flow will be spilled when an outlet restriction is present. Air pressure is not expensive and widely available, vacuum however is more difficult to generate and therefore more expensive. This means that the presence of an outlet restriction can actually be beneficial in terms of operating costs.

2.3.2. Motor function

The in-plane force in an active air bearing is generated by viscous traction of air flowing along a substrate. In a simple air bearing the net air flow is zero, since air flows in equal proportions to the left and right sides. However, it has been shown that by introducing a stepped or tilted surface a net air flow can be created in any desired direction. With the outlet restriction concept, it is also possible to create an in-plane force. All three concepts have been optimised for an optimal ratio of force over mass flow, which is called the **performance ratio**. Using the optimal configurations found, the performance ratio curves can be found by varying the

actuator length L. A typical set of working conditions has been used to generate figure 2.15; the fly height is taken equal to 10 μm and the vacuum pressure is set at 0.5×10^5 Pa. Next to the performance ratio curves also a blue asterisk can be seen in the figure. This asterisk indicates the point on the curve where the outlet restriction concept has an actuator length equal to 7 mm.

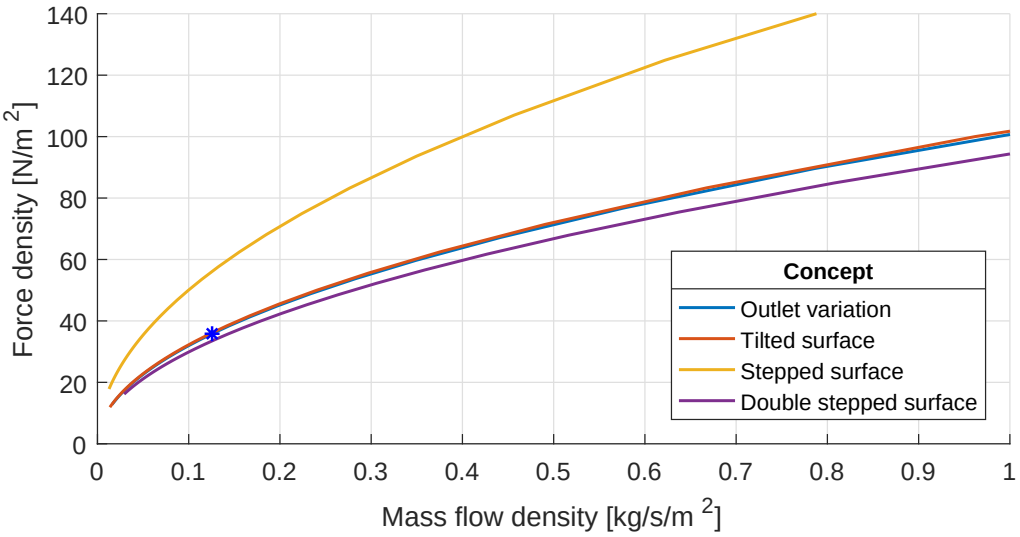

Figure 2.15: Performance ratio curves for the different concepts

.

It is very clear that the performance ratio of the stepped surface actuator is the highest for all actuator lengths. However, this actuator is only able to actuate in a single direction. To make a fair comparison with the other concepts the stepped surface should be made bidirectional as well. The simplest way of doing this is by placing two stepped actuators opposite of each other. Note that this situation can be optimised by removing the dam between the outlets and merging the two outlets to a single outlet. The bidirectional actuator has a configuration similar to the outlet restriction concept with the in and outlets switched. If α and β would be defined in a similar way as well, the optima would be at α equal to 0.63 and β equal to 1.8. The pressure distribution for this type of actuator can be found in figure 2.16 for different values of β. The purple line in figure 2.15 is the performance ratio for this configuration.

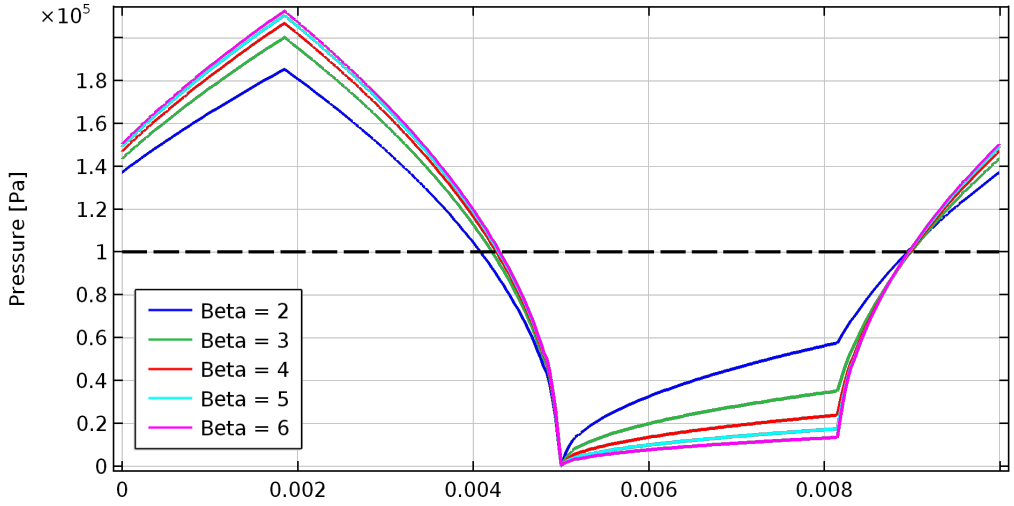

Figure 2.16: Pressure distribution for a bidirectional stepped surface actuator for different values of β and a α value equal to 0.63.

Comparing the three bidirectional actuators it can be concluded that the performance ratio of the tilted surface and the outlet restriction concept is comparable, although the latter performs slightly better. Moreover, it can be seen that the bidirectional stepped surface actuator has a lower performance ratio. The reason for this low ratio could be the influence of compressibility, since p_+ has to be higher for the bidirectional stepped surface actuator to obtain equal load capacity. The inlet pressure p_+ has to be higher to compensate for the low pressures at the right side of the actuator seen in figure 2.16.

The three concepts have also been optimised to find the maximum theoretical **performance limit**, which can be found by optimising the following ratio $\overline{F}^2/\overline{\dot{m}}$. The performance limit curves have been plotted in figure 2.17 for the different concepts. Also, a blue asterisk is placed on the performance limit curve of the outlet restriction concept where the length is equal to 7 mm.

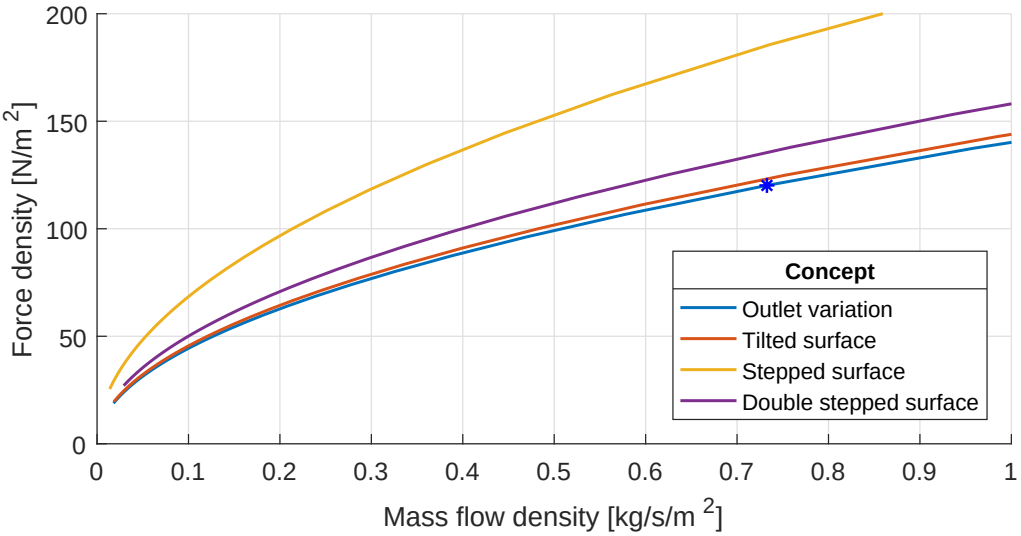

Figure 2.17: Performance limit curves for the different concepts.

Again, it is clear that the stepped surface concept with single actuation has the highest performance limit. The purple line presents the performance limit of the bidirectional stepped surface that has been obtained with α equal to 0.83 and β equal to 5.1. Again, the tilted surface concept and the outlet restriction actuator are quite similar, the tilted surface performs slightly better. The bidirectional stepped surface actuator does not have the lowest limit, actually it has the highest performance limit when comparing the bidirectional actuators, however a significantly higher pressure source is required to generate the mass flows in this situation.

A complete study into the performance ratio has been done, although the performance limit yields a higher force density over mass flow density. To understand this, it is interesting to compare the location of the asterisk in figure 2.15 and 2.17. The actuator length is equal in both situations, however the mass flows and force densities are considerably different. The reason is the different values of α and β used to obtain the curves. For an optimal performance limit especially β is taken higher than for an optimal performance ratio. A higher β results in a higher mass flow density, and thus a higher force density. The performance ratio deteriorates if the length would be taken equal. If the actuator length is set, the conclusion is that α and β should be taken larger if a high force density is required and a high mass flow is not an obstacle. However, if the actuator is placed in a system with a limited mass flow α and β should be reduced to obtain the highest force density related to the available mass flow. This guideline holds for all actuator concepts discussed.

2.4. Conclusion

Using a simple air bearing example, the Reynolds equation has been applied and used to derive compressible and incompressible pressure distributions. Moreover, equations for force density and mass flow density have been derived. For the simple air bearing the bearing function has been explored, moreover the stiffness has been explained in terms of pressures and resistances to air flow, present in the in and outlet as well as in the air gap, called the surface resistance. The derived equations for force and mass flow density have been applied on the stepped and tilted surface concept. The pressure distribution was derived analytically as well

as an equation for the performance ratio and the performance limit. The performance ratio can be found when $\overline{F}/\overline{\dot{m}}$ is optimised and the performance limit can be found when optimising to $\overline{F}^2/\overline{\dot{m}}$. When doing so, the optimal configuration has been found for both situations. A new concept, the outlet restriction concept has been introduced and its behaviour and optimal configuration have also been found. It turns out that the bearing function is comparable with the other concepts. The advantage of a lower vacuum flow is interesting in a later stage if the concept would be introduced in an industrial environment. The motor function has also been compared among the three concepts. It turned out that the tilted surface and the outlet restriction concept are very similar. Depending on whether the performance ratios or performance limits were compared the stepped surface performs respectively slightly worse or better. This means that this research which is focussed on the exploration of the outlet restriction variation concept for contactless positioning is interesting, since potential benefits have been seen in terms of manufacturing and bandwidth.

3

Actuator design

In the previous chapter it has been concluded that the outlet restriction concept is a concept with potential in a two-dimensional setup. In this chapter the focus will be placed on the three-dimensional geometry and the possibilities for restrictors. A three-dimensional geometry shape will be chosen based on the performance ratio and the stiffness. Since air flow is expensive, especially if a vacuum source is used, and the solar cell industry is a competitive business the performance ratio instead of the performance limit is taken as the performance indicator in this chapter. In this chapter, the type of in and outlet restriction will be chosen, and the influence of different design options on the concept characteristics will be discussed. All the analyses have been done with the zero load condition and a vacuum pressure equal to 0.5 bar.

3.1. Inlet restriction

As explained, an inlet restriction is necessary to create stiffness in an air bearing. An inlet restriction is basically some sort of a barrier that obstructs flow and creates a pressure difference. Three types of restrictors are commonly used to restrict air flow: Porous, orifice and capillary restrictions. In appendix B a complete overview including formulas to obtain the restrictive level are given. Based on the ease of implementation and adaptability of the restriction, a capillary inlet restriction has been chosen. The resistance of the restriction will be calculated using the adiabatic Fanno flow theory, since previous research [29, 39] showed that the assumption of laminar flow is not correct.

3.2. Outlet restriction

The inlet restriction creates stiffness and has been investigated in the previous section. The outlet restriction variation concept, is based on the ability of changing the restriction of the outlet restriction such that a net air flow in a desired direction can be generated. Outlet restrictions can be divided in two classes: the distributed restriction or a continuous restriction.

3.2.1. Distributed restrictions

In the previous chapter, a two-dimensional bidirectional actuator has been discussed, this resulted in an inlet in the middle of the actuator and outlets on each side. In a three-dimensional setup, this concept can be created with an inlet surrounded by at least three distributed restrictions, which are variable. With some knowledge on trigonometry a force in all planar direction can be generated. This maximum force will vary depending on the actuation direction, since a finite number of actuators will be used. Using multiple actuators rotation can also be initiated, meaning that motion in all planar directions can be controlled.

A way of changing resistance would be to use a valve. In a valve, the flow area can normally be reduced, resulting in a flow restriction and a lower mass flow. It can be seen as an orifice restriction with a variable diameter. Valves are widely available in many configurations and operating conditions. However, a valve that can handle large pressure differences and is small enough to be fitted close to the surface of an air bearing does not exist, which means that the valves would be placed on a significant distance from the actuator surface. This distance introduces a certain lag between controlling the valves and influencing the pressure distribution. This means that the system would be limited in terms of bandwidth, which was indeed the limitation for Wesselingh [40].

3.2.2. Continuous restriction

Another option would be to have a continuous restriction surrounding the actuator surface and inlet. This could be realised with a small gap surrounding the actuator surface, which is connected to the vacuum source on the outlet side. Nothing new so far, since a continuous outlet restriction was also present in the flowerbed [39]. This restriction however was neglected due to the large gap width. A significant outlet restriction could be created by decreasing this gap width. By doing so a thin film flow can be realised through the gap, leading to an outlet resistance R_o that can be found solving the Reynolds equation again. The outlet resistance can be calculated using the following equation, where w is the width of the outlet and the other variables equal to equation 2.7.

$$R_o = \frac{12\mu l}{wh^3} \tag{3.1}$$

If the gap could be reduced on one side while simultaneously increasing the gap on the other side of the inlet a net air flow can be generated which creates the required viscous drag necessary for actuation. Actually, this can be done quite easy by creating an actuator with a certain shape and a plate that has a hole with exact the same shape although slightly larger. This idea to control air flow has never been used in a contactless actuator. Moreover, the outlet restriction can be placed directly at the surface, which is beneficial for the bandwidth. By moving the actuator with respect to the plate the gap width can be changed around the actuator. The gap however should be in the order of tens of micro meters, which could lead to manufacturing challenges if an exotic actuator shape would be chosen. An option to enlarge the gap would be to use a flexible porous medium in the gap, meaning that the same restriction can be obtained with a larger gap.

3.2.3. Comparison outlet restrictions

As discussed, using distributed outlet restrictions can be easy, since valves are commercially available. However, this results in a variable restrictor that is relatively far from the actuator surface meaning that the system will be bandwidth limited. The continuous restriction however can be made directly at the surface which means a higher bandwidth can be achieved. Manufacturing challenges can be overseen by choosing a smart actuator shape. Moreover, a smart actuator shape can also lead to a design where the forces generated can be equal in all directions. For these reasons, it has been decided to continue with a continuous outlet restriction based on a thin film. The concept of using a variable continuous outlet restriction based on a thin air film has not been used in the field of contactless actuation, therefore this idea is seen as an interesting contribution of this research. The usage of a continuous outlet restriction filled with a flexible porous medium is left as a recommendation, since it did not fit in the scope of this research.

3.3. Geometry

The type of in and outlet restriction are fixed, since a capillary will be used as inlet restriction and a continuous air gap will be used as outlet restriction surrounding the inlet. In this section, the actuator geometry will be discussed. Different actuator shapes have been discussed by Vuong [39, Ch. 4] and Snieder [33, Ch. 5]. In both studies, it is clear that the actuator shape has influence on how the force differs for different actuation directions. A link can be seen between the number of actuator corners and the differences in force between actuation directions. More corners in the actuator shape means less difference in force per actuation direction. The limit case, an infinite number of corners on the actuator shape, results in a circle as actuator shape. With a circle as actuator shape the force is equal for all directions and the mass flow was minimised according to the analysis done by Vuong. However, instead of implementing a circular shape he did chose for a hexagonal pattern, since this is the shape that looks most like a circle and is able to fill a surface.

Also for the outlet restriction concept a round actuator is preferable due to a similar flow for all actuation directions. In section 3.5 the statement of equal force over all actuation directions has been verified. Another large advantage is the manufacturing which becomes less complicated using a round shape. A round actuator can for example easy be made with high accuracy on a lathe. Using any other shape requires other (more complex) manufacturing methods. Although, it is not possible to fill a surface with circles, this is no problem with the outlet restriction variation concept. This concept includes dams which obstruct flow from one actuator to the neighbouring actuator, this means the surface in between the circles will be filled with dams. Filling a surface in the most efficient way using equally sized circles will be done with a hexagonal packing. With some space in between the circles for dams, a top view for the surface can be seen in figure 3.1. Concluding, due to the foreseen manufacturing benefits and a low average mass flow for all actuation directions a round actuator shape has been chosen.

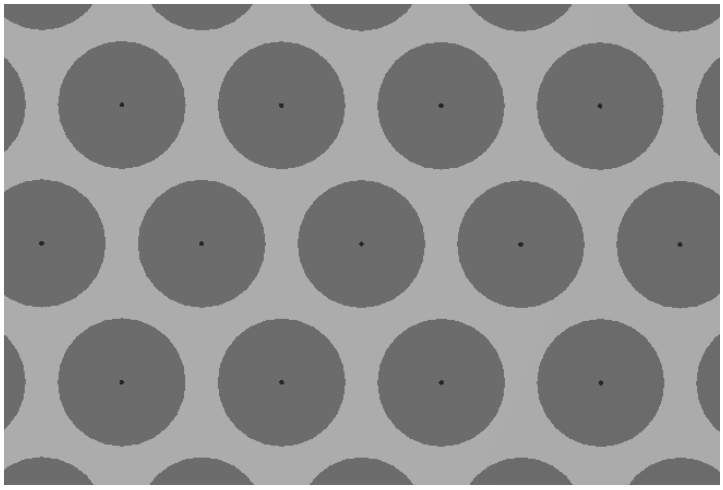

Figure 3.1: Top view of the actuator surface with grey dams and dark grey actuators with an inlet in the middle.

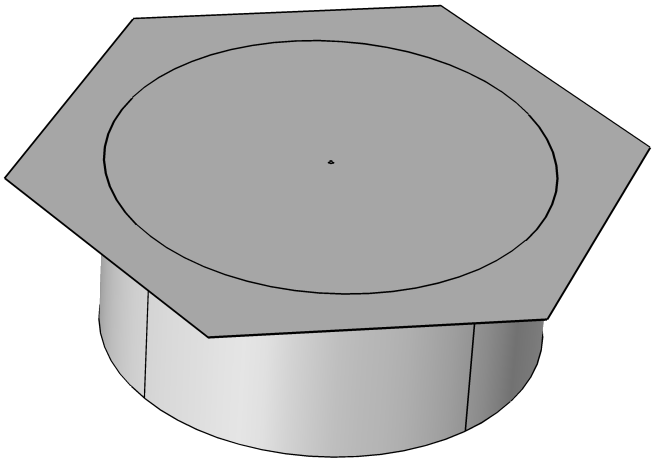

Figure 3.2: Actuator geometry in COMSOL.

To obtain a pressure distribution for a single round actuator shape with dams and outlet, a geometry has been created in COMSOL that has a hexagonal shape with a circle in the middle representing the actuator surface, see fig 3.2. A hexagonal shape is used such that a periodic boundary condition can be used for two opposite sides of the hexagon, thus the results obtained hold for a surface filled with identical actuators. The pressure is assumed constant throughout the film height; a two-dimensional evaluation of the Reynolds equation can be done on this plane after prescribing a fly height for the surface. Within the circle the fly height is larger than outside the circle. Moreover, a cylinder is connected to the circle representing the outlet restriction. A gap width will be prescribed at this surface such that the outlet restriction can be modelled using the Reynolds equation as a thin film. A small circle has been drawn in the middle of the actuator representing the inlet, the inlet radius has been chosen hundred times smaller than the actuator radius.

Prescribing a constant and equal gap width for the outlet, results in an actuator which is exactly in the middle of the gap. The pressure distribution on the surface for this situation is visualised in figure 3.3a. The pressure distribution in the gap has been found as well and can be seen in figure 3.3b. Note that a different colour scale has been used in both figures, which has been done to obtain a higher contrast such that the pressure differences per figure are visualized in the best way. If the same colour scale would be used, one would see the same colour at the circle on the surface as at the top of the cylinder, indicating their physical link.

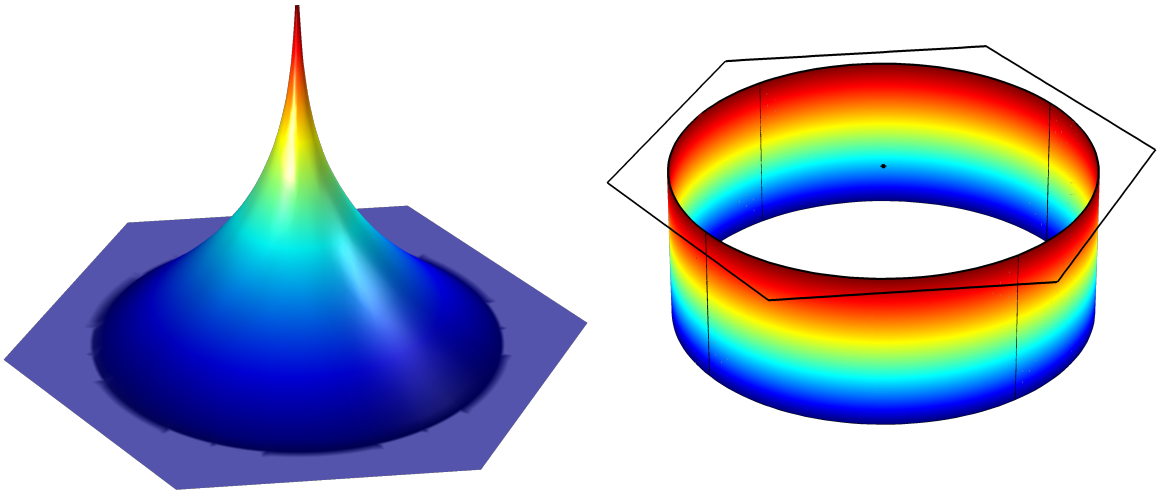

(a) Surface

(b) Gap

Figure 3.3: Pressure distribution obtained with a constant l gap width in the gap, a different colour scale has been used for both plots.

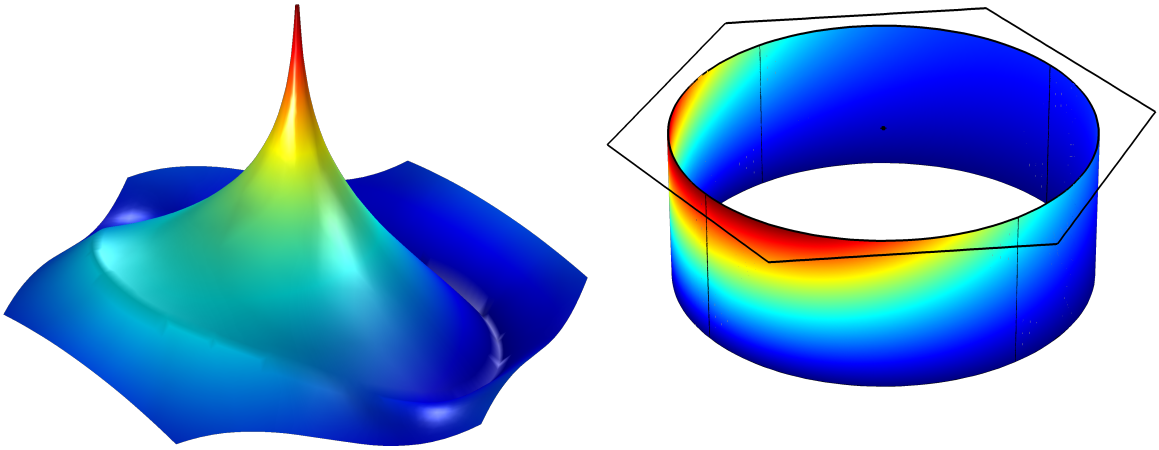

(a) Surface

(b) Gap

Figure 3.4: Pressure distribution obtained when the actuator is moved its full actuation range, a different colour scale has been used for both plots.

An axial symmetric pressure distribution can be seen in figure 3.3a, which is as expected since the restriction is equal in all directions of the actuator. Moreover, no air flow will be present over the dams, since the pressure on both sides of the dam is equal. This is similar to what has been seen in the two-dimensional analysis. The thin film restriction in the gap creates an axial symmetric pressure distribution as well, meaning that the air flow is equal and the flow direction is perpendicular to the surface. The pressure distribution shows a different situation after actuation. A larger pressure difference is present for air flow to the right side relative to air flow to the left side, as can be seen in figure 3.4. Since the thin film restriction is equal for all directions at the surface, this means that more air is flowing to the right which will create a force in that direction. A counter force will also be created since an opposing air flow is present over the dams. The pressure distribution in the gap is also different, at the right side there is a small pressure distribution since the restriction is decreased. At the other side, a large pressure difference is seen, which can be explained with an increased resistance. Moreover, circulating air flow is present as well, since the pressure gradient is not only pointed downwards.

3.4. Actuator dimensions

3.4.1. Actuator size

Since the actuator shape and geometry are known, this section will focus on the dimensions of the actuator. Since the actuator geometry is known α can be defined again. α is defined as the ratio of the diameter of the actuator divided by the shortest diagonal of the hexagonal surface in figure 3.2. For the remainder of this chapter α and β have been set to 0.8 and 2 respectively, which is based on the two-dimensional analysis. α is rounded for simplicity and chosen slightly higher since the shortest diagonal has been used for the definition. β has also been rounded to the nearest integer. Moreover, the values chosen for α and β do not influence the design guidelines created and conclusion drawn. An optimization that has been done after writing the main part of this chapter showed optimal values of 0.87 and 2.25 for α and β respectively. As expected an optimal value for α has been found that is higher than the value in the two-dimensional analysis.

In chapter 2 we have seen that the force density reduces for a larger actuator length (equation 2.16). However, the mass flow density decreases faster for a larger actuator length (equation 2.25), resulting in a higher performance ratio for a larger actuator. This means that in terms of performance a larger actuator would be preferable. The actuator length has been defined as the diameter of the circle on which all the corners of the hexagon can be placed, which is equal to the longest diagonal of the hexagon.

The disadvantage of a large actuator is the influence of the actuator on the substrate. If pressure peaks would be spread over larger distances on the surface this will result in larger substrate deformations and higher tensions in the substrate. This is unwanted for two main reasons. The first reason involves the fact that the contactless planar stage based on air actuation has potential benefits over conventional mechanical contact due to a lower risk of breakage. High stresses in the substrate could lead to breakage of the substrate. The second reason is that large deformations of the substrate could lead to contact of the substrate with the actuator, losing all the benefits from contactless actuation. This means that the actuator size has to be limited by the resistance to bending, which is determined by the substrate thickness and strength.

A COMSOL model has been set up to verify the behaviour. A constant pressure and vacuum source have been assumed, the fly height was calculated by COMSOL. Figure 3.5 shows the deformations of the substrate as well as the maximum von Mises stress. Actuation has been varied from zero to maximum and the actuator length has been increased with 10%.

In figure 3.5 it can be seen that the deformation and stresses are indeed larger when the actuator is larger. Moreover, the deformations and stresses are higher when actuation is prescribed. Not only the actuator length and actuation position determine the deformation and stresses in the substrate, the pressure difference applied has a direct effect as well. This means that a clear guideline between substrate thickness and strength on one side and the actuator size on the other hand cannot be formulated since this is also depending on the pressure difference and chosen fly height. The pressure difference itself is depending on geometric variables as well as force density and mass flow density requirements.

Although deformations and stresses are a challenge for an air based contactless actuator, it poses also benefits; during simulations, it has been noted that a lower substrate thickness increases the performance ratio. An explanation of this effect can be found in the deformations of the substrate which changes local fly heights. A negative deformation is mostly present above the dams and a positive deformation is present above the pockets, resulting in a situation where the deformations help the dams in minimizing the opposing air flow, which increases the performance ratio.

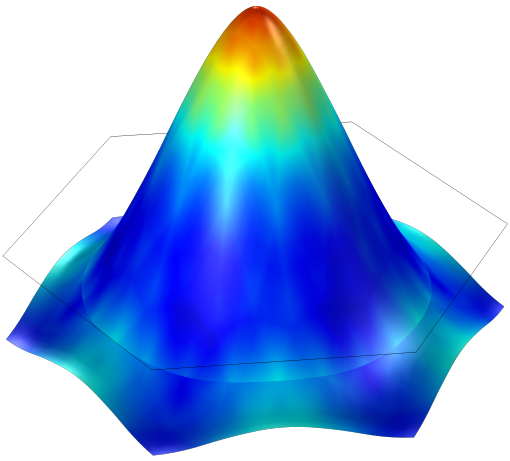

(a) Actuator without actuation

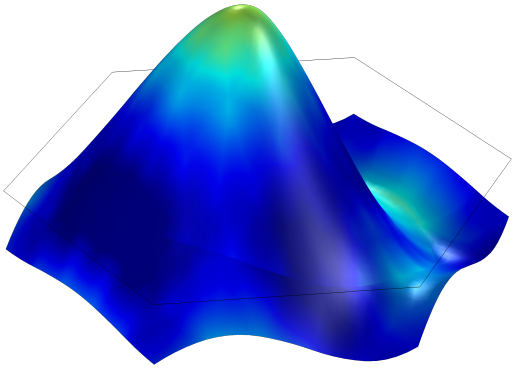

(b) Actuator with actuation

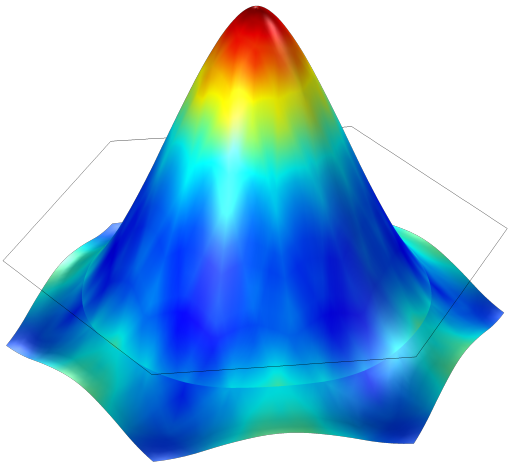

(c) 10 % larger actuator length without actuation

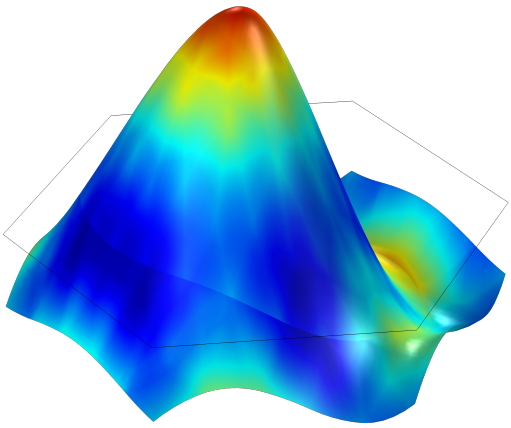

(d) 10 % larger actuator length with actuation

Figure 3.5: Deformation and maximum von Mises stress visualized in a single figure. The deformation is visualized using the position and the maximum van Mises stress is visualized using colours. The deformation and colour range are equal for all figures.

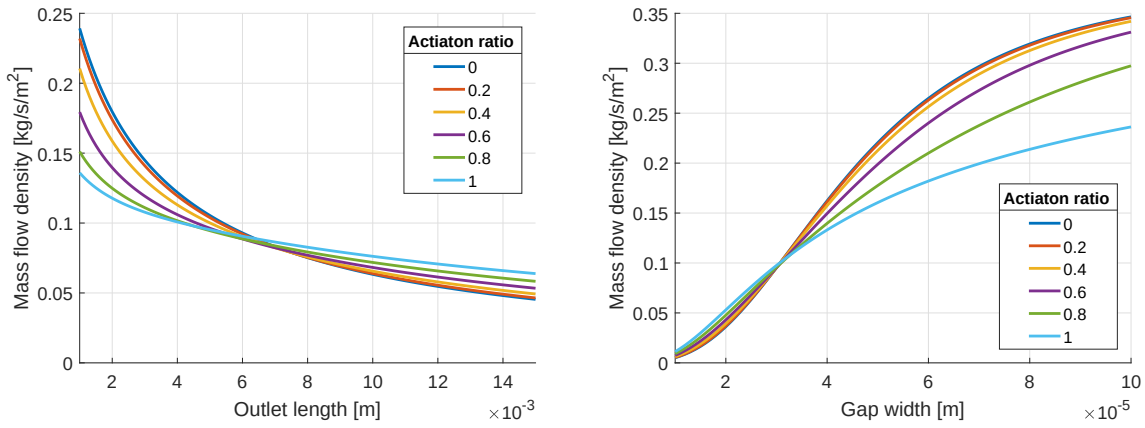

(a) Varying outlet length with a constant gap width (25 μm). (b) Varying gap width with a constant outlet length (10 mm).

Figure 3.6: Influence of outlet length and gap width of the outlet on the mass flow density.

Since a contactless actuator based on the outlet restriction variation concept has never been build, the design focus is based on a functioning actuator and not on minimizing the substrate thickness for a first setup. This means that actuator sizes should be chosen such that manufacturing can still be done. An actuator diameter equal to 10 mm and a minimal dam length of 2 mm gives promising results in terms of performance in combination with manufacturability. This means that α, which is the ratio between pocket and dam, ranges between 0.83 and 0.72 for different actuation directions. These values will be fixed in the remainder of this report.

3.4.2. Outlet

The outlet can be defined using three parameters, the outlet length and the gap width define the global restriction and the actuation ratio will be used to indicate the level of actuation. An actuation ratio of 0 indicates zero actuation and an actuation ratio of 1 or -1 indicates maximum actuation. An actuation ratio of 0.5 indicates that half of the gap width is used for actuation. In this section, an overview will be sketched explaining the influences of these three variables on the performance of the actuator. In this section, a COMSOL model will be used, all simulations have been done for a constant fly height ($h_0 = 10\,\mu$m) and vacuum pressure ($p_v = 0.5$ bar), meaning that a corresponding pressure source is found by COMSOL, while the load will be kept equal.

Increasing the outlet length and decreasing the gap width will result in an increase of the outlet restriction. This means that a higher pressure difference will be present over the outlet, leading to a lower pressure at the start of the outlet. The pressure source will be corrected and lowered by COMSOL to fulfil the load requirements. Overall this will result in a lower pressure difference between pressure and vacuum source, indicating a lower mass and volume flow. Decreasing the outlet length and increasing the gap width will have contrary results, thus higher mass flow should be found. Some results can be seen in figure 3.6, where indeed the mass flow increases for a larger gap width and shorter outlet length.

Another interesting output from figure 3.6 is that for most outlet length and gap width combinations the mass flow varies for different actuation ratios. This indicates a different total air resistance of the actuator while actuating, which means that the pressure source has to be adjusted to maintain the same load. In practice, with a fixed pressure source, this means that the fly height will be compensated to maintain the load, which is unwanted. There is however a combination of outlet length and gap width in both sub figures indicating the possibility to keep the mass flow more or less constant while actuating. This is the point where all the mass flow curves for different actuation ratios are close to each other. Unfortunately, they do not cross in the exact same point when zooming in, however this is still an interesting combination between mass flow and gap width, since a constant fly height is be beneficial for positioning.

Besides a constant fly height, a maximum performance ratio is interesting. Figure 3.7 shows the performance ratio while varying the outlet length and gap width for certain actuation ratio values. In terms of performance it is clear that the outlet length has an optimum, contrary to the gap width. Although an optimum is present it is clear that an outlet length longer that the optimal length will not reduce the performance

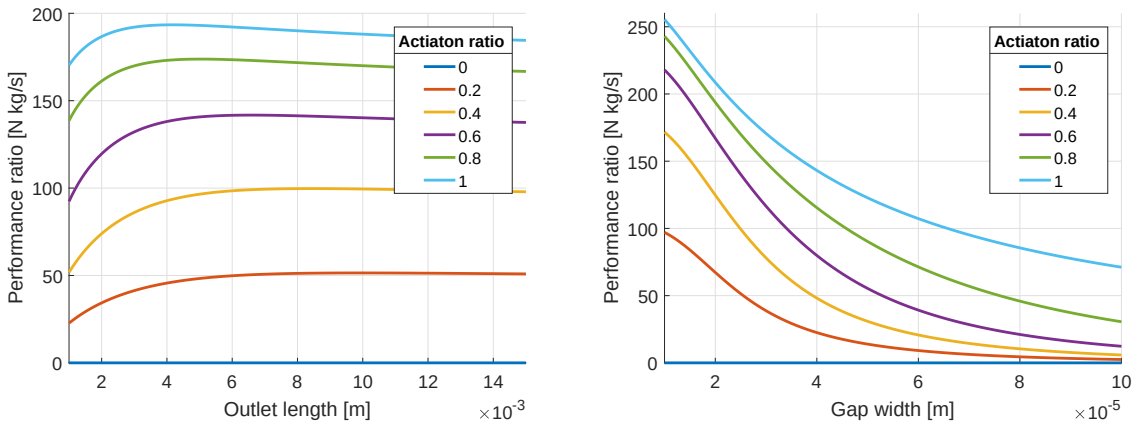

(a) Varying outlet length with a constant gap width (25 μm). (b) Varying gap width with a constant outlet length (10 mm).

Figure 3.7: Influence of outlet length and gap width of the outlet on the performance ratio.

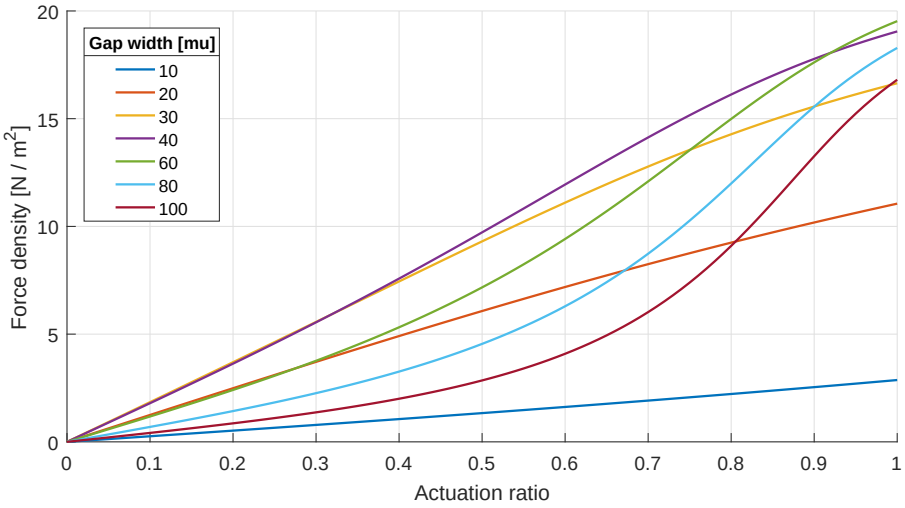

Figure 3.8: Force density distribution for different actuation ratios, the outlet length is taken equal to 10 mm.

ratio drastically. A shorter outlet length however will have serious influence on the performance. The simulations have been done for a certain configuration (α, β and actuator length) of the actuator. It has been noted that varying this configuration will lead to another optimal outlet length. For the gap width different results are found, since a smaller gap width will always increase the performance ratio. A smaller gap width however will lower the stiffness and will be challenging for production.

Next to a high performance ratio, a constant force distribution would be an advantage, doubling the actuation ratio would lead to a doubled force. During simulations, it has been noted that this is the case for small gap widths. When increasing the gap width above a certain limit the force distribution is not linear any more, see figure 3.8. This behaviour can be explained with the fact that for larger gap widths the relative restriction difference becomes smaller if not fully actuated. For the outlet length such behaviour has not been seen, the force distribution decreased overall if the outlet length was made longer.

It is clear that the outlet restriction design should be done carefully while prioritizing the preferences and requirements. The outlet can be designed such that a stable fly height is possible or such that the performance ratio is optimised. A linear force distribution can also be obtained, moreover the manufacturing should also be taken into account. Based on the figures 3.7b and 3.8 it can be stated that a smaller gap width is generally better, since a higher performance ratio and a more linear force distribution will be obtained. A downside however, which has not be named in this chapter, is that the stiffness will reduce as a result of increasing outlet restriction. This should be compensated with a higher inlet restriction.

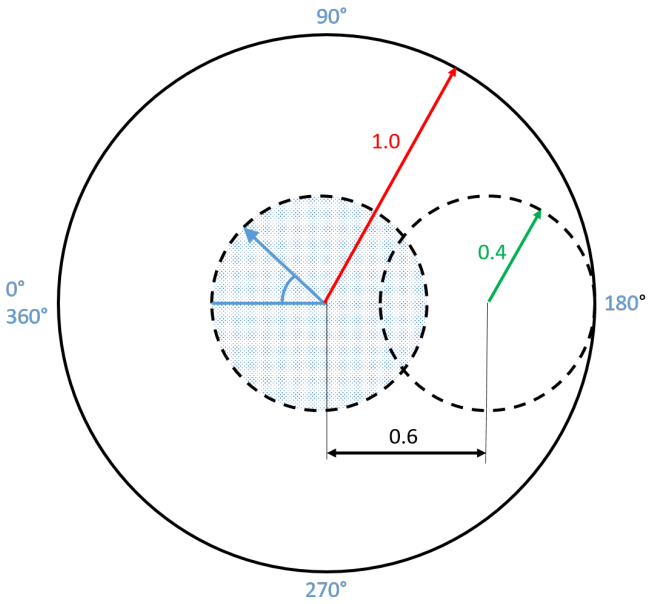

Figure 3.9: The maximum actuation space is equal to the gap width, therefore the actuation ratio (0.6 in black) and the off-centre ratio (0.4 in green) should never exceed 1.0.

3.5. Tolerances

Tolerances on a design provide a permissible limit of variation between design and prototype. Tolerances are necessary since manufacturing has its limitations. In this section, the influence of tolerances on the performance of the outlet variation contactless stage will be investigated. The focus will be placed on the concentricity of the gaps between the actuator and its counterpart. Other important tolerances, such as flatness, roughness and variations of flow restrictions, have been investigated [29, 39, 40] and are quite intuitively.

In this section, it is assumed that a setup consists of an infinite number of actuators which are all fixed to each other. Moreover, it is assumed that all the actuator axes are perfectly parallel to the axes of its corresponding holes, resulting in a gap width which does not vary over the outlet length. More over, the term off-centre ratio will be discussed, which is defined with a value between 0 and 1. An off-centre ratio with a value of 0 indicates that for all the actuators in a setup the actuator axis is exactly equal to the axis of the corresponding hole, zero tolerance is allowed. An off-centre ratio equal to 1 indicates that the tolerance on concentricity equals the gap width. This means that no actuation is possible, since with an infinite number of actuators it can be assumed that the full tolerance will be used in all directions. Note that the summation of actuation ratio and off-centre ratio can never be larger than 1, since at a value of 1 the actuator closes the full gap meaning that further actuation is not possible.

In figure 3.9 the actuation space of an actuator is shown, every point in the figure represents a possible location for the axes of the actuator. This means that without actuation and with an off-centre ratio equal to 0.4, all actuator axes are placed in the blue circle. Placing an infinite number of actuators with a normal distribution in this area, indicates that actuators will be placed on the boundaries as well, which limits the actuation range. In case of maximum actuation to the right, the new location of all the actuators will be within the small circle on the right. Maximum actuation is obtained with an actuation ratio equal to $(1-0.4=)0.6$. It is clear that an increasing off-centre ratio results in a smaller actuation range.

To make a fair comparison, first the influence of the actuator geometry will be investigated for different actuation directions. A constant force has been assumed over all actuation directions. However, the hexagonal packing of actuators results in an uneven distribution of dams around an actuator, see figure 3.2, therefore a different force could be possible for different actuation directions. Figure 3.10 shows the maximum force per actuator over a range of 60 deg, this result can be copied for the other actuations directions, since the actuator surface is a regular hexagon. To create figure 3.10 the fly height, vacuum pressure, β, outlet length and gap width were respectively fixed at 10 μm, 0.5 bar, 2, 10 mm and 50 μm. For these typical working conditions, it is clear that the force differs not significantly with actuation direction, meaning that this can be neglected in further analysis and that the assumption of constant force for round actuators made earlier is correct.

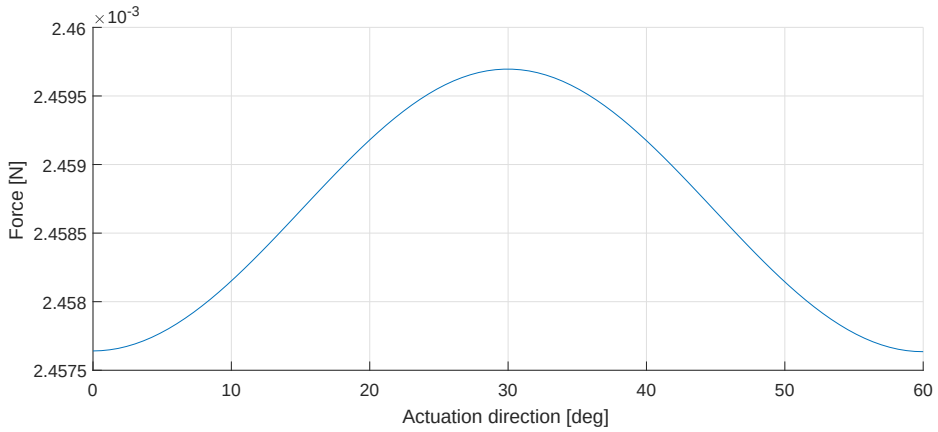

Figure 3.10: Maximum actuator force per actuator for different actuation directions.

So far it has been seen that a perfectly centred actuator with a small gap width provides an approximately linear behaviour between actuation and force, see figure 3.8. To predict the maximum force, it is interesting to verify whether this linearity is still present when a tolerance on concentricity (a non zero value for off-centre ratio) is present. First the term off-centre direction should be introduced as well. This term describes in which direction the off-centre ratio is applied for a single actuator hole combination. The directions correspond to the angles shown in figure 3.9, for example an actuator with an off-centre ratio of 0.4 and an off-centre direction of 45 degrees has its axis at the end of the blue arrow in figure 3.9. Moreover, actuation of the actuator is done in the direction of zero degrees in the remainder of this section. This means that the forces will be created in the direction of 180 degrees, in figure 3.9. Figure 3.11 shows the force density for varying actuation ratio as well as for different off-centre directions and ratio's.

First, let's focus on the three straight lines which indicated a zero off-centre ratio. An increasing actuation ratio induces higher forces, which is as expected since the actuation ratio indicates the amount of actuation. Moreover, the force is equal for all off-centre directions, which makes sense since the straight lines are obtained for an off-centre ratio equal to zero. Secondly, it can be seen that an increasing off-centre ratio leads to a deviation of the straight lines. This deviation looks like a sine wave with an increasing amplitude for increasing off-centre ratios. The sine wave can be explained with the directions in figure 3.9. For an off-centre direction equal to zero degrees the off-centre placement is in the direction of actuation, thus a higher force density is obtained. Contrary, for an off-centre direction equal to 180 degrees the off-centre placement is in the opposite direction of actuation, thus a reduction of force density is obtained, if the off-centre ratio is higher than the actuation ratio even negative forces can be seen.

Moreover, it can be seen that the added force due to actuation is not constant over the off-centre directions in figure 3.11. Figure 3.12 focusses on this difference in added force. In this figure, the red and green dotted lines are copied from figure 3.11. The difference between those lines is the added force as a result of actuation, subtracting those two lines give the solid black line in figure 3.12. The other solid lines represent the added force for lower actuation ratios, a similar pattern can be seen.

For a setup with an unlimited number of actuators with a prescribed tolerance on the concentricity, all the actuators will have an off-centre ratio smaller or equal to the prescribed tolerance. Assuming that the actuators are spread over the possible off-centre ratios and off-centre directions according to a normal distribution, the actuator force in a certain actuation direction can be averaged over the off-centre directions. Figure 3.13 shows a plot where the forces are averaged for different off-centre and actuation ratios. The dotted black line is identical to the solid black line from figure 3.12, neglecting that the x-axis has changed. The yellow circle, in figure 3.13, for actuation ratio of 0.6 and off-centre ratio 0.4 has been placed at a force density that is equal to the average of the dotted black line. In a similar fashion, the other yellow circles have be obtained by averaging the force density over all off-centre directions in figure 3.12 for its corresponding actuation ratio. The other lines in 3.13 are created in a similar way, however a different off-centre ratio has been used as a starting point. Note that the curve for a zero off-centre ratio curve (blue) has been seen before in figure 3.8. The curve in not fully linear since the gap width is slightly too large for a linear curve.

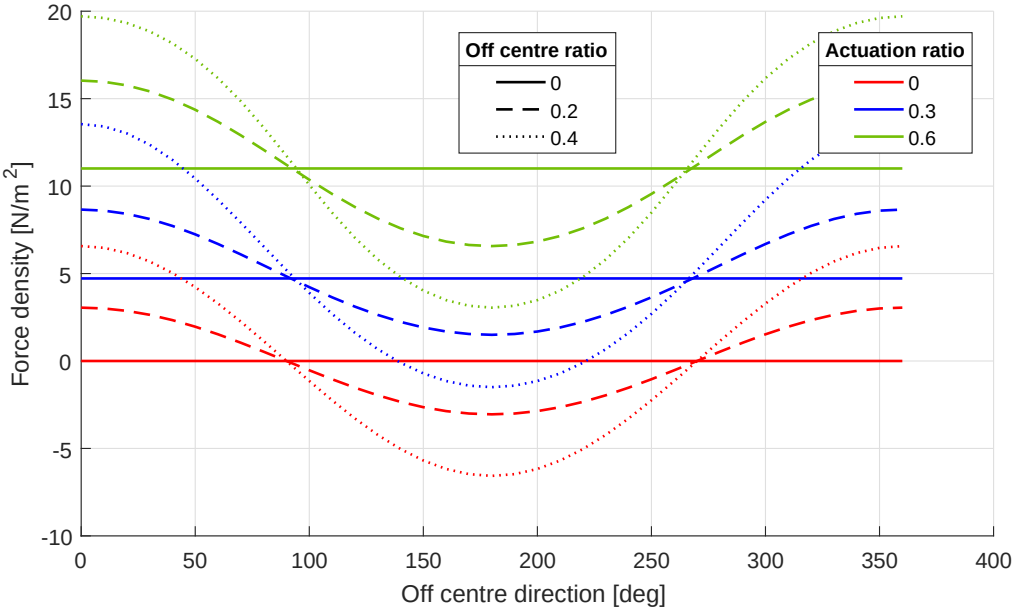

Figure 3.11: Force density for different gap and off-centre ratios plotted against off-centre direction. An increasing off-centre ratio increases the deviation from the zero tolerance line (zero off-centre ratio).

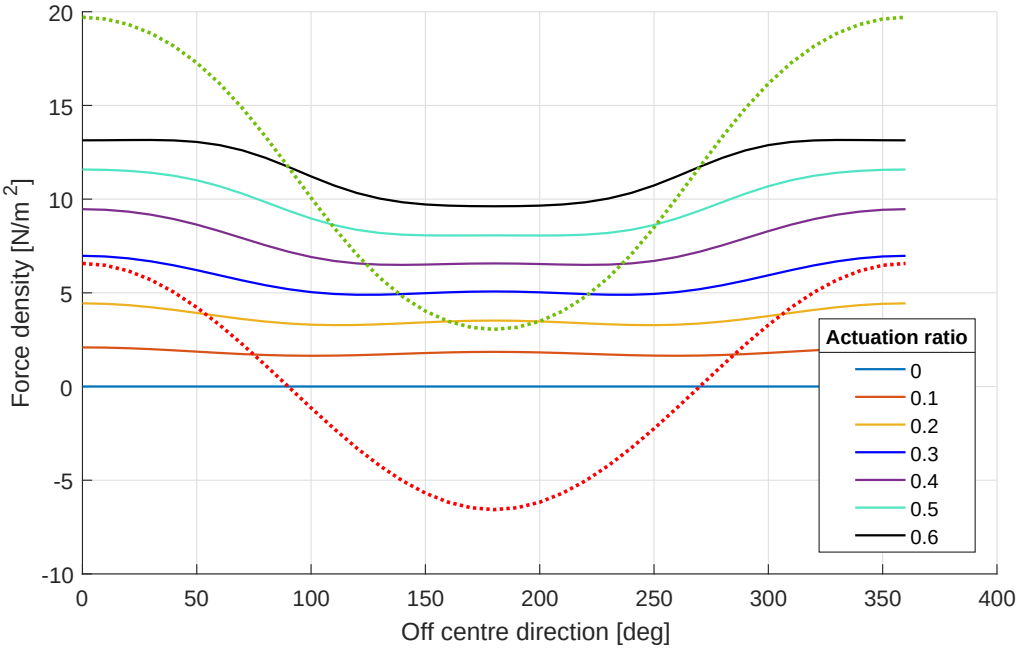

Figure 3.12: Added force as a result of different actuation ratios for an off-centre ratio equal to 0.4.

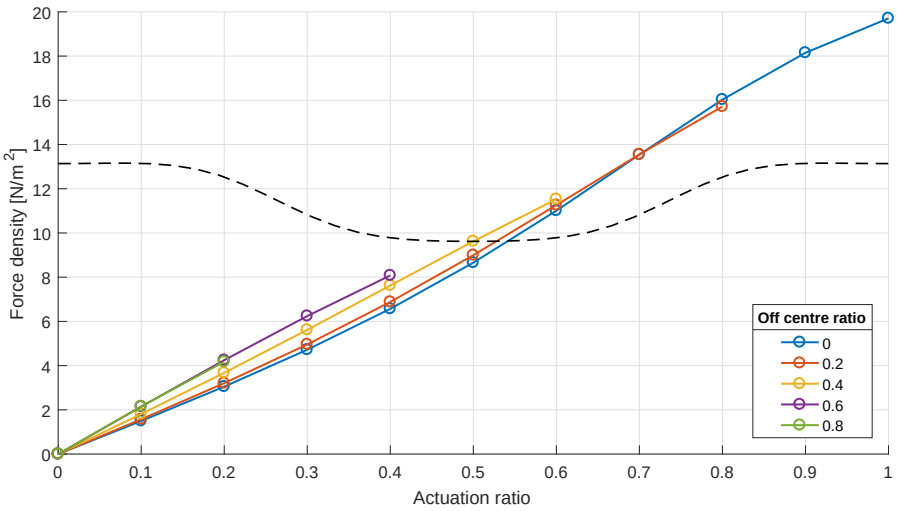

Figure 3.13: Averaged force density over all off-centre directions for different off-centre ratios. A higher off-centre ratio leads to a lower maximum force since the actuation ratio cannot fully be used, the force actuation curve becomes more linear which is positive.

Figure 3.13 shows the data necessary to conclude something useful about the influence of the off-centre ratio on the performance of a setup. First of all, it is clear that a smaller off-centre ratio leads to a higher possible force density since a larger portion of the actuation ratio can be used. Another interesting finding is that for a given actuation ratio up to approximately 0.7 a larger off-centre ratio gives a higher average force density. This feels counter intuitive since it means that a larger tolerance gives a slightly better performance for a given actuation ratio. The maximum force density however will always decrease due to the limit on the actuation ratio. A last remark on figure 3.13 is that the lines are obtained for a certain off-centre ratio which has fully been used in all directions. In reality, a small fraction of all actuators will be located on its maximum tolerance assuming a normal distribution, this means most actuators will be placed closer to the ideal position in the middle, thus the performance of these actuators will be closer to the blue line with a zero off-centre ratio. Reasoning further this means that the force density curve for a given maximum off-centre ratio will be closer to the zero off-centre ratio curve. Concluding, an off-centre ratio above zero will lower the performance due to a limit on the actuation ratio, moreover the influence of the off-centre ratio up till the maximum actuation level makes the force density curve more linear, this has also been seen for other gap widths. This means that the force density curve for a certain off-centre ratio can be derived from the force actuation curve which is given in figure 3.8 with a deviation that makes the curve more linear.

3.6. Conclusion

In this chapter, a design has been proposed for the outlet restriction concept. Based on the expected benefits for implementation a capillary restriction has been chosen, moreover the adiabatic Fanno flow will be used to predict the resistance. Afterwards the outlet restriction has been discussed. Out of the distributed and continuous restrictions, the latter has been chosen due to the foreseen bandwidth advantages. The outlet restriction will be placed in a circle surrounding the inlet to create equal forces and mass flow for all actuation directions, moreover benefits are seen in terms of manufacturing. The actuators will be placed in a hexagonal pattern, since this gives the largest actuator density. The effect of increasing the actuators size has been shown, first of all the performance ratio will improve, a downside however is that the flying substrate will deform more as a result of higher stresses. Afterwards the influence of the gap width dimensions has been discussed. The outlet has influences on a stable fly height over the whole range of actuation, moreover the performance ratio can be influenced. It has been seen that a smaller gap width leads to a more linear force/actuation curve. Finally, the influence of an actuator pin that is not perfectly centred has been discussed. It turns out that the maximum force density reduces mostly due to a limited range of actuation. The effect of off-centre placement is less significant when averaged over all actuation directions, it turned out that the force actuation curve becomes more linear.

4

Design realisation

In this chapter, the design realisation of the outlet restriction variation concept will be discussed. First the goals of building a setup are described. Two main goals have been defined for the outlet restriction variation setup. First of all, a proof of concept for the outlet restriction variation concept is required, since a contactless actuator based on this principle has never been made. This means that actuation in all planar degrees of freedom is pursued which is bidirectional translation in two planar directions and bidirectional rotation around the out of plane axis. The second design goal for the setup would be to compare the performance of the contactless stage with a numerical model based on the Reynolds equation. The chapter will start with a short explanation on how many actuators will be created. Afterwards the crucial parts of the design are discussed, leading to an overview of the manufacturing methods for these parts. Air restriction theory from the previous chapter is used to dimension the restrictions, which are experimentally verified afterwards. Lastly a system to control the pocket depth is discussed and implemented before the air and vacuum supply is attached to the setup.

4.1. Number of actuators

Figure 3.1 shows a surface with many actuators. However, to achieve proof of concept and force validation a small amount of actuators can also be used. Since manufacturing becomes more complicated for larger numbers of actuators, a limited number will be chosen. The first three axisymmetric options are a setup with one, three or seven actuators. Rotation is impossible to achieve with a single actuator, moreover rotation will also be challenging for a setup with only three actuators, therefore a setup with seven actuators is chosen.

4.2. Crucial parts

The basis of a working setup does consist of only two components; a plate with seven holes and another plate with seven raised pins with an air inlet. The relative position of the pins should be the same as for the holes, moreover the pins should have a slightly smaller diameter than the holes, the outlet gap is determined by this diameter difference, a diameter difference in the order of tens of micro meters is pursued. The plate with holes, called the top plate, will be positioned above the plate with pins, called the bottom plate. Connecting the inlets to a pressure supply and creating a vacuum between the two plates makes the actuator active. In figure 4.1 the two plates are shown, the red top plate should be lowered such that the surface of the pins is some micro meters lower than the top surface of the top plate. This distance will be determined by the chosen value for β. The large distances between the plates has been taken to show the two parts separately.

In the previous chapter it has been concluded that a concentric placement of the pins and holes plays a significant role in the force generation. Moreover, the concentricity in combination with gap width is seen as the largest challenge in terms of manufacturing. Therefore, the options to create the top and bottom plates will be discussed before other challenges are discussed. Other challenges include the supply and sealing of pressure and vacuum source, embedding the inlet restriction as well as positioning the top plate relative to the bottom plate.

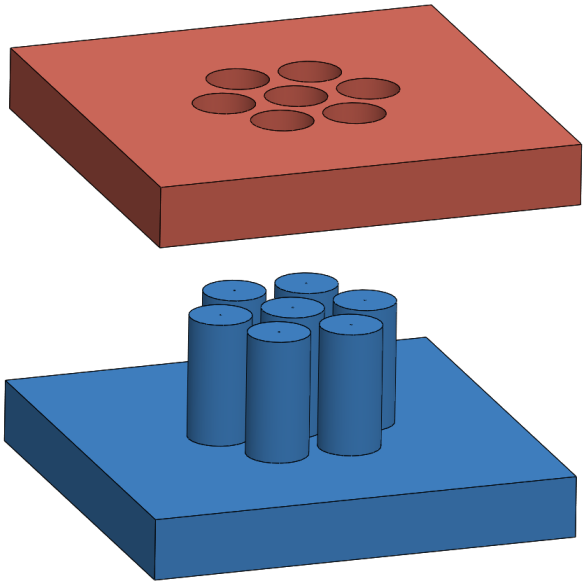

Figure 4.1: Red top plate with seven holes and blue bottom plate with seven pins and air inlet.

4.2.1. Gap width and concentricity

In this section, some methods to manufacture the bottom and top plate will be discussed. While reading, note that only gap width and the concentricity of pins and holes is relevant, an absolute offset in position will not cause serious problems as long as a similar off set is present for the gap and hole. For this reason, it could be interesting to manufacture the gaps and pins in the same production step ensuring coaxial location. There are no special requirements on the material as long as it is thick enough and does not bend as a result of the pressure differences.

Laser cutting

The first method explored is laser cutting. Vagher [36] has obtained interesting results manufacturing active air bearings for thin film actuations. Especially the stepped approach has been identified to be promising using a laser cutter. Multiple layers could be (partially) glued together, afterwards the pins and actuators can be created simultaneously. Figure 4.2 shows the production steps for a section view. Gap widths in the order of 25 μm can be achieved in thin objects nowadays [2, 31, 32]. The aspect ratio, which is the depth of the cut over the width, is for small gap widths limited around 2. This means that the top plate has to be thin, which will cause bending of the plate, since a substantial pressure difference has to be separated by the plate. Although perfect concentricity could be obtained, laser cutting has been rated ineffective due to large gap width for thicker plates.

Figure 4.2: Production steps using laser cutter, first glue two plates partially together at the yellow locations, then use the laser cutter to make cuts over the black lines. Then the top and bottom plate can be separated.

Additive manufacturing
The second manufacturing method that will be investigated is an upcoming technology, namely additive manufacturing. The technology can be dated back to the 1980s, whereas conventional machining for example has its origin in the 18th century. Nowadays, multiple technologies are available, although they can be generalised to the building of an object using multiple layers of material. The method that is used to bind consecutive layers defines the technology used. Although additive manufacturing has been done at nanoscale [18] in an academic environment, the feature size possible with industry standards is typically 0.1 mm [12, 42]. 3d printers are available with higher resolutions, however these are not available at the department, moreover machine time on these machines is not without costs. To conclude additive manufacturing is an interesting technology although costs and access to machines is a challenge.

Die sinking
A third manufacturing method that will be evaluated is a die sinking process. Die sinking is an electrical discharge machining technology that uses sparks to remove material. A high potential will be created between a tool electrode and a workpiece electrode, moving the electrodes closer to each other will results in sparks between the two electrodes. At the spark location some material will be removed due to the high energy density. The spark location is the location where the distance between both electrodes is shortest. If the top plate would be made as desired by drilling some holes, the bottom plate (tool electrode in this case) can be made with the die sinking process by slowly lowering the top plate to the work piece. The bottom plate becomes the exact negative of the top plate with a small gap width in between. This means that this manufacturing method ensures the concentricity perfectly, as long as the top plate is moved in a straight line. The size of the gap width can be controlled varying the potential between the two electrodes. A higher potential means that the sparks are created on a larger distance between the electrodes and thus a higher gap width will be created. Moreover, the surface roughness will be larger as well since the amount of material removed per spark is larger. Gap widths of 10 /mum can be achieved [19], however larger gap widths are more common, since this speeds up the production process. Die sinking machines are not available at the department meaning that it should be outsourced. For small gap widths a lot of machining time should be reserved, which will make the manufacturing expensive. Concluding a very promising technology to create bottom and top plate for the outlet restriction variation concept, in house manufacturing is unfortunately not possible.

Milling and turning
The conventional machining techniques milling and turning can be used to make the top and bottom plate. The top plate could be made with a simple drilling operation followed by a reamer to get the diameter of the gap within a certain accuracy. The bottom plate however is difficult to fabricate as a single part with conventional techniques. The pins can however be made separately from the plate, meaning that a second plate with holes is necessary. Those holes have to be coaxially with the holes in the top plate, afterwards the pins can be glued or pressed within the top plate. Using a lathe the diameter of the pins can be controlled very precise. If the diameter of the holes in the bottom plates are made some micrometres larger than the pins, the pins can be placed in a nearly perfect out of plane direction. All these steps can be done in house, which is seen as a large advantage for a first prototype. Recent technologies however did improve and computer numerical control (CNC) has been added to milling machines meaning that also the bottom plate could be made as a whole in a milling operation. Dimensional accuracy can be achieved up to sub micron level [1]. CNC machines are available at the workshop, however these machines are older and accuracy up to a micrometre will not be achieved, meaning that manufacturing should be outsourced if CNC milling will be chosen as manufacturing method.

Comparison
In this section multiple manufacturing methods have been discussed. Several methods are suitable to create pins and holes which are coaxially. Especially laser cutting and die sinking seem very promising, since the production process itself ensures concentricity. Laser cutting however, will create gap widths that will be too large and therefore this is not an option. Due to the possibility of in house manufacturing it has been chosen to make the initial prototype using conventional machining with a lathe and mill. However, the author realises that for a surface with more pins and holes or for the production of multiple actuators outsourcing of production will be more efficient. In that case a decent investigation should be done comparing prices as well.

4.2.2. Manufacturing

In collaboration with the workshop it has been decided to make the actuator from aluminium, since this material is easier to machine than steel. Moreover, sheet material with different thicknesses was available. Next to the requirement of coaxial pins and holes another requirement is placed on the plates, since the plates will be a barrier to separate a pressure difference. This means that with fly heights in the order of 10 μm the plates should not bend too much as a result of the pressure differences. Especially the bottom plate will be loaded with significant pressures, since it separates the vacuum and pressure source. Figure 4.3 shows the deformations based on a pressure of 0.5 bar between the plates and 4 bar at the bottom to supply the inlets, the plate thickness is taken at 10 mm.

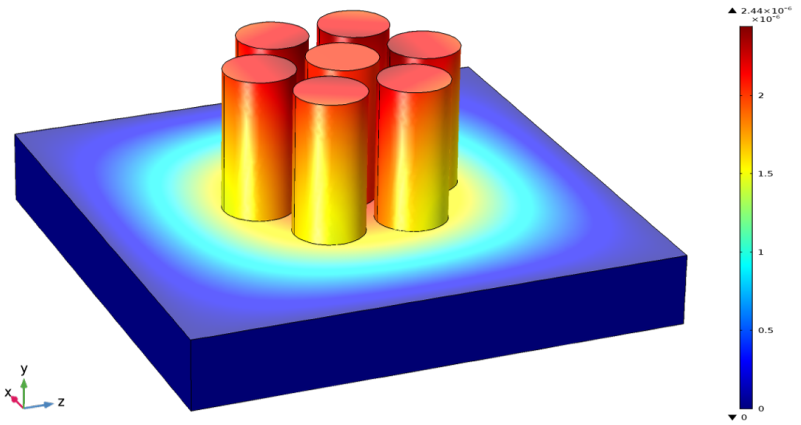

Figure 4.3: Deformation [m] of the bottom plate as a result of a 4 barpressure at the bottom and 0.5 bar at upper side of the plate. The pins are left unloaded and the plate is constrained on all sides.

Figure 4.3 shows that a plate with a thickness of 10 mm deforms almost 2.5 μm as a result of the pressure distribution. The highest deformation is present in the middle since the plate bends upwards and is constrained at the sides. The displacements in x and z direction are less than 1.5 μm and the difference between y displacements at the pin surfaces is less than a micro meter. Although the displacements are limited, they will still limit the maximum force possible since the actuation range will become smaller, which has been discussed in section 3.5. However, a plate thickness of 10 mm has been accepted since this thickness has a nice balance between deformation and manufacturability, which becomes harder for thicker plates. Moreover, the outlet length is also partially settled with this decision, since it cannot become longer than 10 mm. Introducing extra manufacturing steps the plate can be made locally thinner, shortening the outlet length. This is in the first place unwanted due to the extra steps and in the second place since the stiffness of the top plate will reduce at the most vital location, therefore the outlet length is set at 10 mm.

The pin diameter had been set to 10 mm, a dimension without decimals, due to foreseen manufacturing advantages and tolerable bending of the substrate. The reason for this is the availability of standard tools for this diameter. This is the case for clamps for the lathe as well as drills and reamers. Therefore, the pin diameter will be 10 mm and the holes in the bottom plate as well. This means that the top plate has to be made with holes slightly larger than 10 mm. Again, due to the ease of manufacturing and the availability of tools a hole diameter of 10.1 mm has been chosen. This leads to a gap width of 50 μm, which is in the desired range.

Using a milling machine of the type Emco FB-4 two plates have been manufactured with holes at the same location. Using a standard mill, the production started by making two identical plates with right angles and flat surfaces, such that the plates can be clamped in a similar way with respect to the machine. Using a drill and reamer holes have been made in the bottom plate at predefined coordinates. At the same coordinates the slightly larger holes have been made in the top plate using a drill and bore (Dutch: kotteren). It is clear that the dimensions of these gaps should be very precise, accuracies up to a few micrometres have been reached.

The next step involved the manufacturing of pins. A pin is a simple rod with constant diameter that fits perfect in the holes of the bottom plate. Using a lathe from the type Emco Mat 17D the pins have been machined within a few micrometres to 10 mm. Different methods have been tried to fasten the pins in the bottom plate, more detail can be found in appendix D. The final solution was fastening using Loctite 246, an

anaerobic adhesive.

After fastening, the top surfaces of the pins were not in the same plane, using a face mill (Dutch: mantelkopfrees) this was corrected after some attempts. It turned out that the older machines in the work shop, which were serviced more recently, obtained better results. Results have been checked using a Veeco - Bruker Contour GT-K1 white light interferometer, which is available at the optics lab at Delft University of Technology. An IXL2.5 lens has been used for magnification and the stitching function has been used to measure surfaces larger than the viewing area. For the final machining step, the older milling machine Aciera F3 has been used to ensure in plane flatness of all the pins. The corresponding surface profile can be found in figure 4.4. As can be seen in the figure, all pins have been machined flat with a maximum peak to peak distance of 8 μm. Small pockets have been drilled in the middle, which can also be seen in the figure, more information can be found in appendix D.

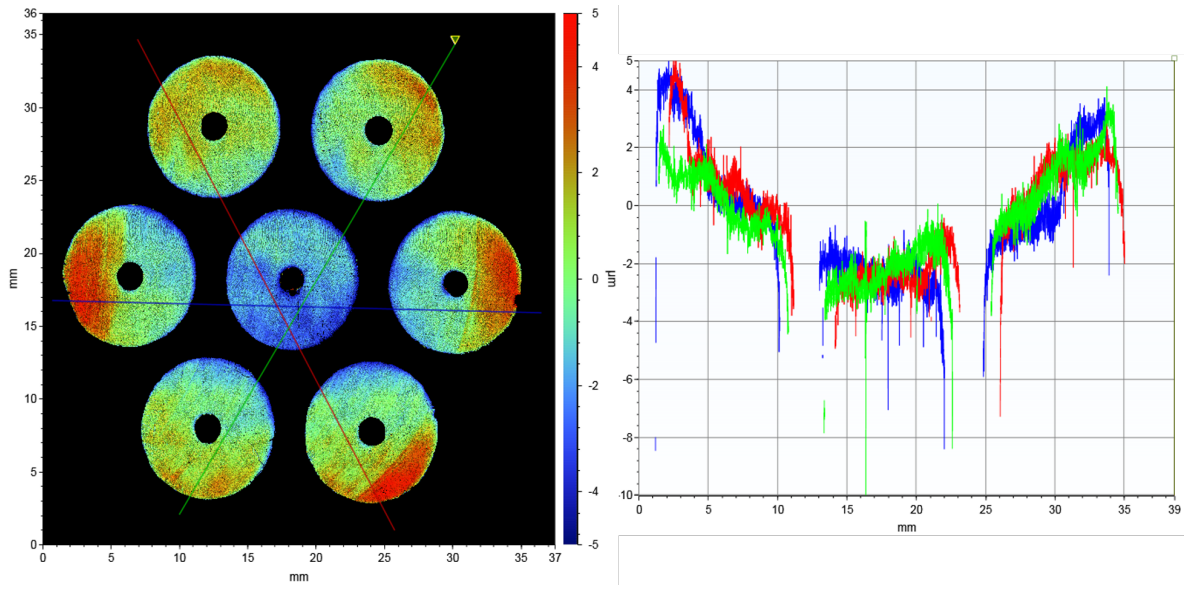

Figure 4.4: Surface profile of pin surfaces, measured with the white light interferometer. A peak to peak flatness of 8 μm has been obtained.

4.3. Restrictor integration

To obtain enough stiffness an inlet restriction is required. The outlet restriction is set, since the gap width and outlet length are defined, which means that a required inlet restriction can be found. Using a combination of Matlab and COMSOL the stiffness can be calculated for different inlet resistances. The fly height is set at 10 μm above the dams, beta at 2 and the vacuum pressure at 0.5 bar. Moreover, in the model, the inlet has been modelled as a circle, with a diameter equal to 0.1 mm. A larger diameter results in extra stiffness, since the high pressure peak will be spread over a larger area. Choosing the inlet diameter small in the model results in a safety margin. First COMSOL will be used to solve for the required source pressure to satisfy the zero load condition, the pressure found will be fixed during the second calculation. The second step starts with a small disturbance on the fly height, afterwards the new pressure distribution will be calculated, integrating this pressure over the surface of the actuator yields a force. Force over disturbance gives the stiffness for a certain inlet restriction. The result can be found in figure 4.5a, note that the distributed stiffness is given.

To satisfy the no load condition while varying the inlet restriction, the pressure at the end of the inlet, pressure p_+, remains constant at a level of 3.1 bar. A constant p_+ results in an equal mass flow as well, the mass flow found was 2.75×10^{-5} kg/s per actuator, which equals to a mass flow density of 0.22 kg/s/m^2. To obtain constant p_+ the source pressure has to increase to cope with the higher restriction, this can be seen in figure 4.5b.

With an inlet restriction of 1.5×10^{10} Pa $*$ s/m^3 a nice balance can be found between inlet pressure and distributed stiffness, therefore it has been decided to pursue this restriction. Using the Fanno flow theory a diameter length graph can be created, which states the required length of an actuator for a given diameter of the capillary restriction, an example can be found in appendix B (figure B.3). The restriction level found

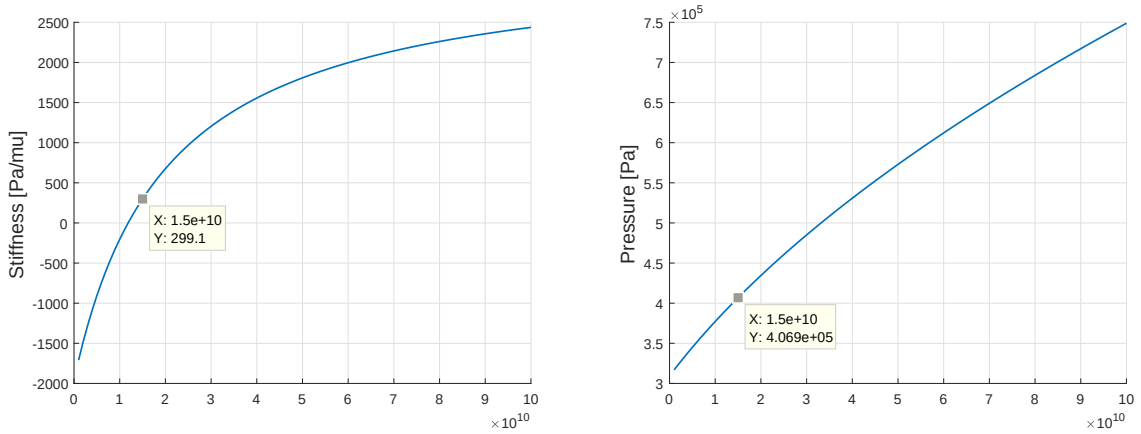

(a) Inlet restriction [Pa ∗ s/m^3]

(b) Inlet restriction [Pa ∗ s/m^3]

Figure 4.5: Distributed stiffness and pressure levels found while varying the inlet restriction.

with the adiabatic Fanno flow is based on a friction factor coefficient, which is obtained using an educated guess. This means an experiment will be conducted to verify the validity of the Fanno flow theory and make a better approximation of the friction factor. A schematic set up of the experiment to verify the friction factor can be seen in figure 4.6, a similar experiment has been done by Hoogenboom [29]. An experiment is done as follows:

- Open valve 1 and close valve 2. This will fill the tank, which has a volumetric capacity of 2 litres, with a pressure specified by the proportional valve. To obtain results over a significant range a pressure difference around 3 bar is taken
- Close valve 1, which ensures that the pressurized air is trapped in the tank.
- Start the measurement in Lab View, which means the program starts recording and saving the measured pressure to a file. Since valve 2 is initially still closed a differential pressure close to 0 bar will be measured.
- Open valve 2, which allows the air to flow out of the tank and through the restrictor. One will see that the measured differential pressure will make a jump to the value specified by the proportional valve.
- Stop the measurement in Labview if the differential pressure approaches zero differential pressure between ambient and tank pressure.

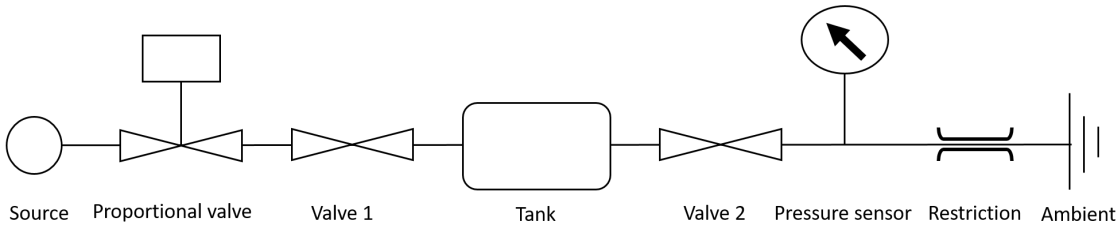

Figure 4.6: Schematic set up of experiment to determine restrictor properties

The valves that have been used are standard manual open/close valves, the tank is a CRVZS-2 tank with a 2 l capacity. The connecting tubes do have an inner diameter equal to 7.5 mm, the volumetric capacity has been compensated for this added volume. The sensor is a NXP MPX 5700DP differential pressure sensor with a range of 700 kPa. More information regarding the restriction measurement can be found in appendix C.

Performing the described steps carefully for different lengths of a tube with a diameter of 0.25 mm one can create figure 4.7. As expected a longer tube requires more time to reach 0 bar pressure difference, since

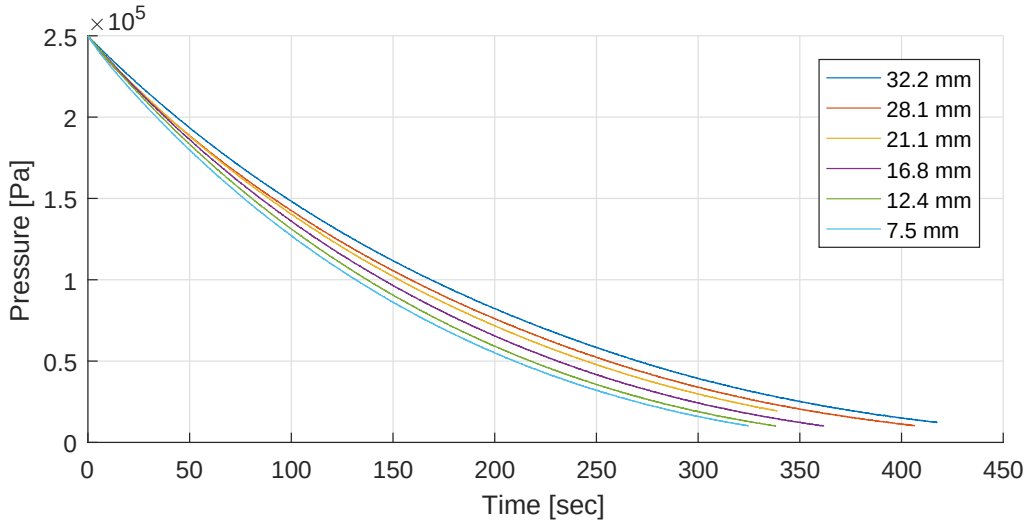

Figure 4.7: Measured pressure versus time for 0.25 mm inner diameter tubes with different lengths

a higher resistance is involved. Moreover, the pressure decay profile is also as expected, since one expects a higher mass flow for higher pressure differences, which are present in the beginning of the experiment.

Assuming a constant temperature in the tank, the mass of the air in the tank can be calculated at any time with the measurements of pressure and time, using the ideal gas law:

$$m = \rho V = \frac{pV}{R_s T} \tag{4.1}$$

where V is the pressurized volume between the two valves. This includes the tank and connecting tubes. After differentiating one finds the following relation for the mass flow:

$$\dot{m} = \frac{\partial p}{\partial t}\frac{V}{R_s T} \tag{4.2}$$

$\partial p/\partial t$ will be negative, so one could add a minus sign to obtain positive mass flow, which makes further calculations more intuitive. Concluding the resistance of any type or air flow restriction can be verified experimentally. Therefore, the tube length and diameter will now be fixed, such that the Fanno flow theory can be verified and the friction factor can be checked.

Tubes with inner diameters in the range of tens of millimetres are not widely available, however two options were found [37]; tubes with 0.18 mm and 0.25 mm inner diameter result in reasonable lengths. The tubes have to be fitted in the actuator pins which are 30 mm long, therefore 0.25 mm inner diameter tubes have been chosen since their length is longer which makes fastening the tubes in the pins less complicated, compared to the shorter 0.18 mm internal diameter tubes. Based on the adiabatic Fanno flow and an estimated friction factor of 0.04 one finds that a 0.25 mm inner diameter tube with a length of 13.1 mm has the required resistance of 1.5×10^{10} Pa $*$ s/m^3, see figure B.3 in the appendix.

Ten tubes with a length of 13.1 mm have been created from a longer tube with inner diameter 0.25 mm. Using the prescribed setup and experiment, measurements were done and the mass flow was calculated based on the measurements and the Fanno flow theory. During the measurements it was noted that in and outlet effects had significant influence. The restriction of a tube changed if the air flow was in opposite direction, moreover different mass flows were reported after deforming the inlet. A deformation has been obtained by pushing a needle into the inlet of the capillary tube.

Figure 4.8 shows a comparison between theory and the ten tubes which have been tested for air flow in both directions, meaning that the black lines represent 20 measurements. The red line is the predicted mass flow based on a friction factor of 0.04. The trend is more or less equal, which is positive, however it turns out that the friction factor is too low. With a friction factor of 0.028 the difference between theory and measurements can minimized, the light blue line represents this situation. The dotted lines in figure 4.8 show the pressure difference at which the Mach number equals unity at the outlet, meaning that the theory at the right side of this dotted line is invalid. Based on the results it can be stated that the Fanno flow theory matches

quite well with the measurements after updating the friction factor. Using a theory that includes the in and outlet effects could improve the prediction of the restriction even further. However, this does also mean that the geometry of the in and outlets should be measured carefully to compare the results with the theory, due to time limitations and the limited added benefits this has not been done in this research.

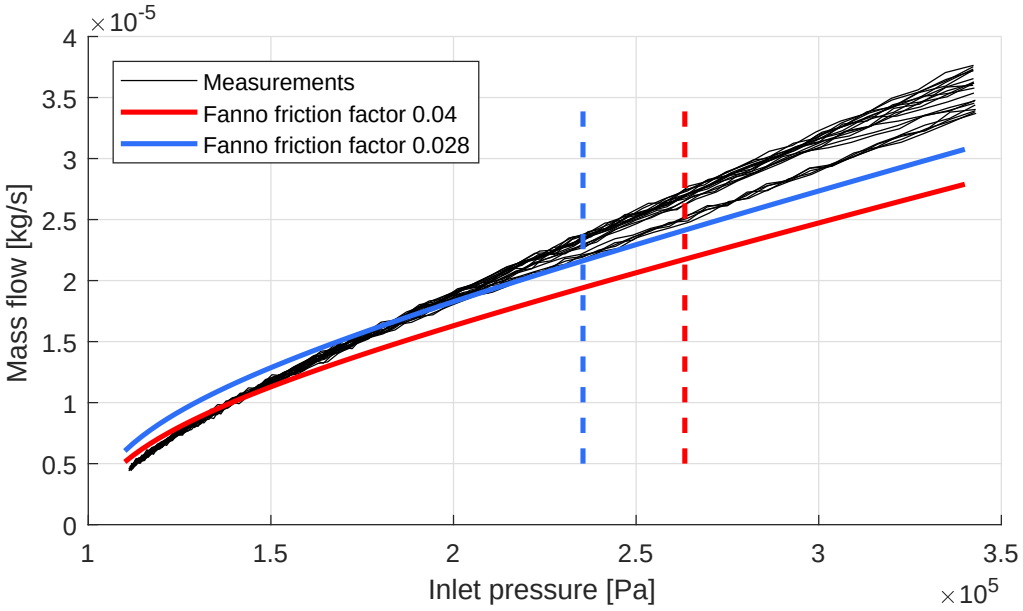

Figure 4.8: Measured and calculated mass flow based on adiabatic Fanno flow for a 0.25 mm inner diameter tube with a length of 13.1 mm. At the outlet of the tube ambient pressure was available. The initial estimated friction factor of 0.04 turned out to be too high, a friction factor of 0.028 has the closest match with the measured data.

Although the friction factor of the tubes was lower than expected, the seven most matching tubes were selected and implemented in the setup. The outside diameter of the tubes equals 1/16 of an inch, which meant that a hole with a diameter of 1.7 mm had to be drilled in the pins. Drilling deep holes with this diameter causes problems, thus a bigger hole was drilled from the other side. The design can be seen in figure 4.9, only one half of the pin has been shown. Glue has been used to fix the inlet restriction tube to the pin. A glue based on cyanoacrylate has been deposited with a needle on the interface between tube and pin from the bottom side. A cyanoacrylate glue has been used since it is known for its low viscosity and creeping in small gaps before drying.

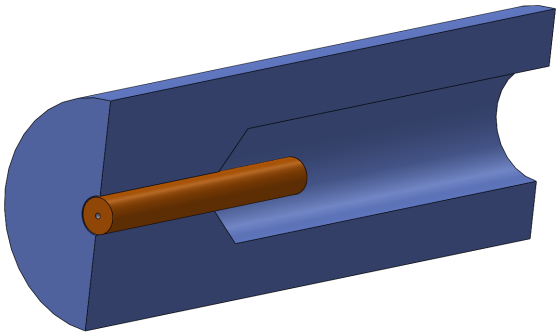

Figure 4.9: Actuator pin in section view with mounted inlet restriction

Pictures have been taken with an USB microscope from the installed pins with restriction already integrated, see figure 4.10. A magnification of 35 has been used. It can be seen that a pocket is generated at the

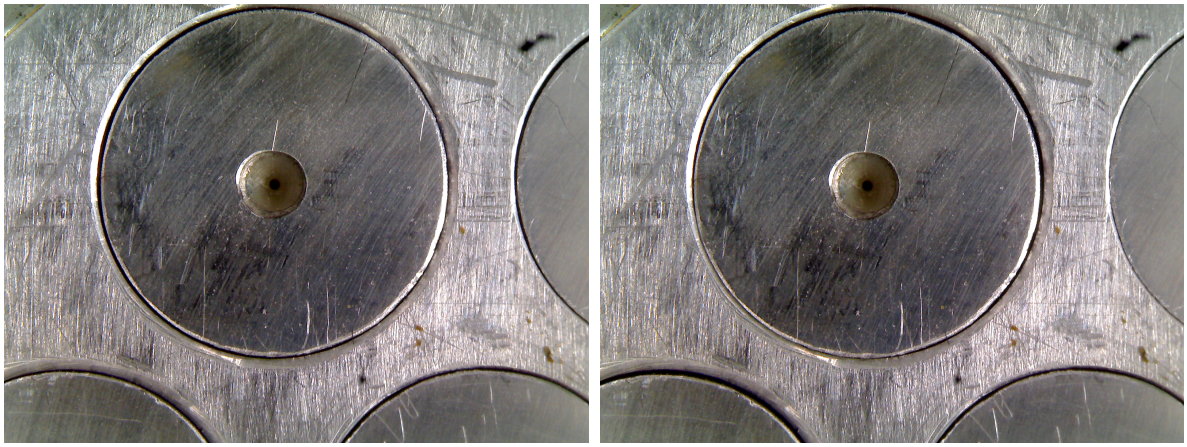

Figure 4.10: Restriction integration and changing gap width is visible with a microscope.

location of the inlet, see appendix D for more details. Moreover, the changing gap width as a result of a manual actuation can be seen when comparing both figures. The top plate has been rotated, which results in a changing gap width around all pins except the middle actuator. It can be seen that the middle actuator, seen at the lower right in both figures has indeed a constant gap width, while a gap width change can be seen at the other actuators. Using the same model configuration and settings as that have been used to create figure 4.5, with an added pocket around the inlet and a mass flow based on the measurements, a stiffness equal to 3.27×10^3 Pa/μm was found. A stiffness around 300 Pa/μm was designed for, which means that the pockets do have indeed a larger influence on the stiffness than the lower restrictive value of the inlet. The pocket depth was taken constant over the inlet pocket at 0.1 mm. The inlets have been implemented in the model using a curve fitted through the data that has been found in figure 4.5.

4.4. Plate positioning

Top and bottom plate have to be positioned in the correct position relative to each other. In the correct position the top surface of the pins is parallel to the surface of the top plate however slightly lower to create the pocket necessary for actuating. Parallel plates ensure also that the centrelines of the pins and holes are parallel, assuming right angles between these centrelines and the surfaces. Moreover, the top plate should be allowed to move in planar direction 50 μm relative to the bottom plate this means that a fixed connection is not possible. A final challenge involves the vacuum pressure in between both plates resulting in a force that pulls both plates to each other.

A first option that has been implemented was a temporary solution based on ball bearings to test other components of the setup. Three shallow holes have been milled in the bottom plate, afterwards three ball bearings have been placed in those holes. The top plate was positioned over the actuator pins and rested on the ball bearings. The round ball bearings allowed relative motion between the plates. However, after applying vacuum pressure between both plates and performing some initial tests, small deformation were seen in the aluminium top and bottom plate as a result of the locally applied forces. Those deformations were expected but showed clearly that a solution with ball bearings is not a long term solution, therefore another solution was looked for and found in the field of compliant suspensions.

The solution that has finally been adopted in the system is based on compliant wire flexures. Three wire flexures with a length of 10 mm have been installed to suspend the top plate above the bottom plate. A relative displacement of 50 μm between both plates leads to a sub-micrometre height difference change, which is acceptable. The minimum diameter with respect to buckling of these flexures can be determined with the Euler's formula for long slender columns, see figure 4.11.

$$F = \frac{\pi^2 EI}{(KL)^2} \tag{4.3}$$

where

- F is the critical vertical force

- E is the modulus of Elasticity, 180 Gpa for spring steel
- I is the area moment of inertia of the cross section
- L is the unsupported length, 10 mm
- K column effective length factor, 1.2 has been used [30]

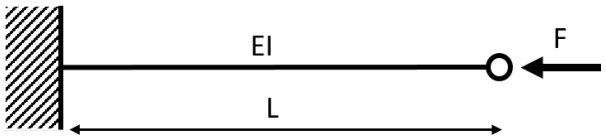

Figure 4.11: Axially loaded beam.

Using some margin, wire flexures with a diameter of 1 mm have been chosen, this meant that three blind holes with this diameter were drilled in the bottom plate. In the top plate bigger through holes were drilled using the same coordinates, afterwards those holes were tapped. A tiny threaded rod with hexagonal head was installed in the top plate. In the threaded rod a blind hole was drilled as well. A section view of the design can be seen in figure 4.12. The three wire flexures have been placed on a circle around the geometric centre of the rectangular plates. No glue or other connections than the described threads have been used, vacuum pressure ensures contact and removes play at the interfaces.

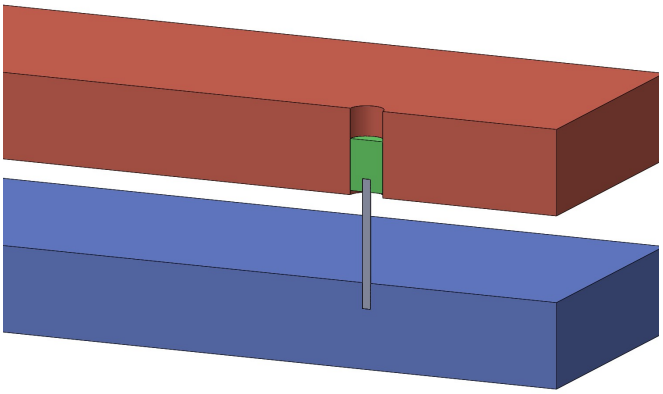

Figure 4.12: Section view of the suspension between the top and bottom plate using a wire flexure (grey) and a threaded rod (green).

4.5. Air supply and sealing

With the plates positioned, the last step before finalizing the setup involves connecting the inlets to a controlled high pressure source and the outlets to a controlled vacuum pressure source. Although it is a critical to the functioning of the concept simple and effective solutions could be found.

Let us start with the vacuum supply and sealing. A sealing between the two plates should allow some displacements of the plates relative to each other. Therefore, the sealing between the two plates should be at least partially flexible, this was ensured using commercially available duck tape. A stroke of the pressure sensitive tape, with a length slightly longer than the four sides of the plates summed, was used to seal the vacuum chamber. The air supply was created using a Festo threaded fitting, which is also commercially available.

The high pressure supply was slightly more difficult to implement however the basic idea is comparable. A manifold was created that surrounds the inlets of the actuator pins and was placed under the bottom plate. A notch in combination with an O-ring was used to ensure air tightness. The manifold was bolted against the bottom plate. On the side of the manifold a gap was drilled and tapped such that a high pressure line can be connected. An exploded view of the design with the dimensions as made can be found in figure 4.14. Moreover, the actual realised actuator can be seen in figure 4.13a and a figure with removed top plate is shown in figure 4.13b. As can be seen the actuator has been made according to the design with a slight deviation, since more bolts have been used to fasten the manifold, this was required to ensure an airtight connection.

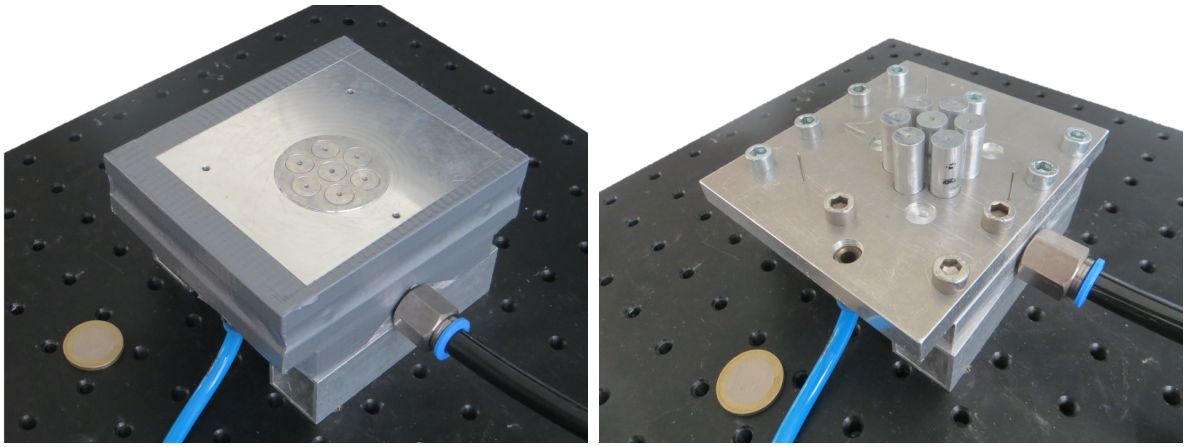

(a) Full actuator.

(b) Actuator without tape and top plate.

Figure 4.13: Pictures from the realised design.

4.6. Conclusion

In this chapter the design realisation of the outlet restriction variation concept has been discussed. The goal was to make a contactless stage that enables all planer motions. To ensure rotation can be actuated significantly the number of actuators has been fixed at seven. Moreover, the top and bottom plate including pins have been identified as crucial parts since a small gap width between pins and holes is necessary, which places restrictions on the manufacturing. Laser cutting and die sinking seemed very promising since the holes and pins can be manufactured simultaneously. However, due to possibility of in house manufacturing conventional machining has been chosen as manufacturing method. Using a white light interferometer flatness was checked and improved afterwards using a face mill. The inlet restriction has been dimensioned using the Fanno flow theory. The unknown friction factor has been determined using an experiment. It turned out that the Fanno flow theory with updated friction factor has a good match with the measurements. Afterwards wire flexures have been installed to position the top and bottom plate, using a hex key the distance between both plates can be adjusted, which influences the pocket depth. The whole setup has been made airtight using an O-ring and a manifold for the high pressure supply and pressure sensitive tape to seal the vacuum. Although the bottom plate has been manufactured independently from the actuation pins, the number of parts per actuator is still very limited compared to the state of the art. Combining pins and bottom plate in a future setup could lead to an even larger reduction in the number of parts. Production methods which are able to create the bottom plate including pins as a single part are die sinking and CNC milling, probably laser cutting can also be used. Concluding, although manufacturing of the first setup based on outlet restriction variation required quite some time, a simple manufacturing method has been developed and potential benefits in terms of manufacturing are still seen.

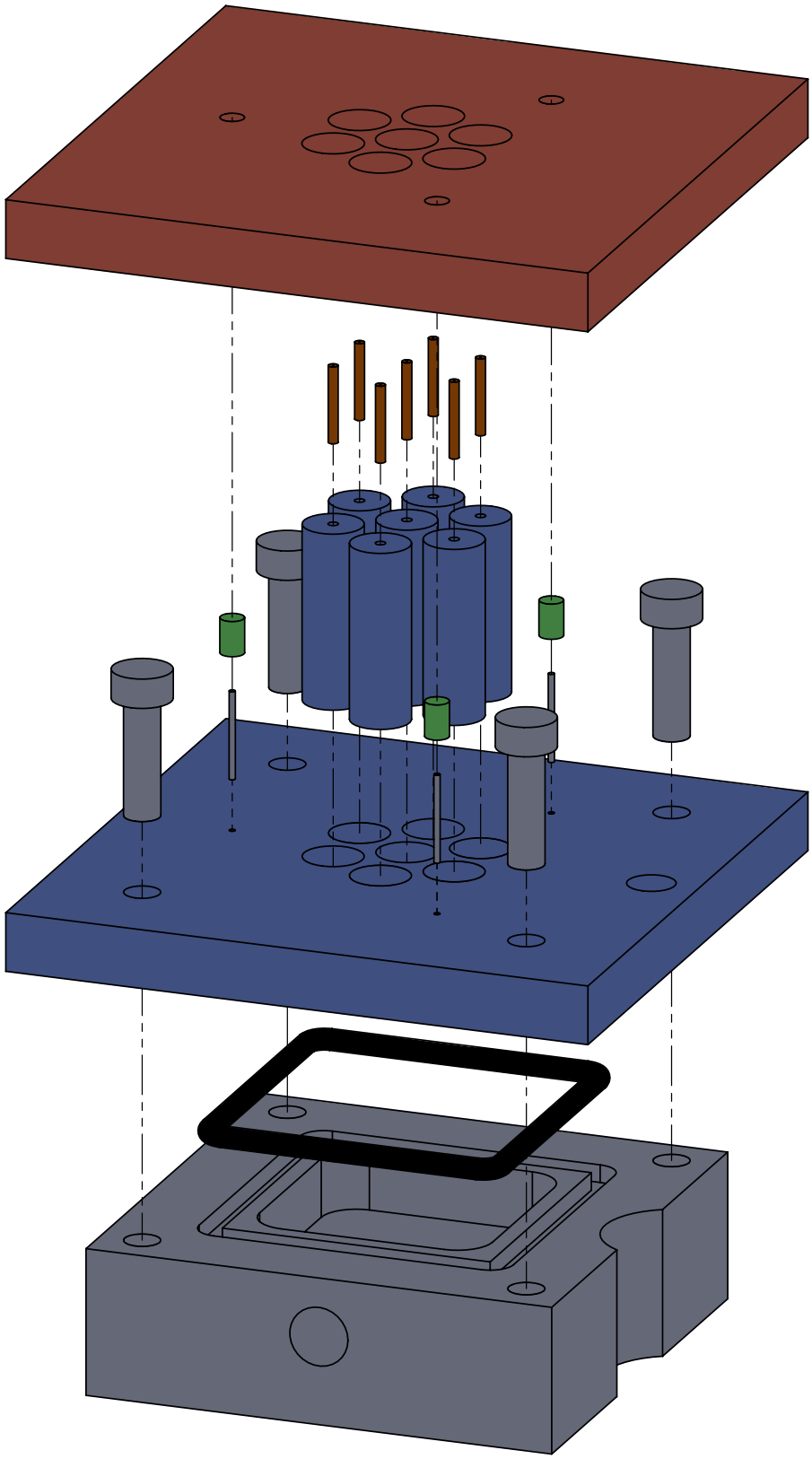

Figure 4.14: Exploded view of the design, tape to seal the vacuum between top and bottom plate as well as the connecting pressure and vacuum lines are omitted.

5

Experimental validation

In this chapter, the experimental validation of the outlet restriction variation setup will be discussed. The goals stated in chapter 4 were a proof of concept and a comparison with the numerical model. The outcome of some initial tests will be discussed as well as some modifications to the setup. Afterwards the measurement setup to measure actuator force, pocket depth and fly height is described. Afterwards the results of those measurements are stated and the obtained data will be compared to the numerical model.

5.1. Initial tests

During initial tests with the setup built as described in the previous chapter, it turned out that it was possible to adapt the gap width and therewith the air flow. A change in gap width has been seen visually and it could be heard that the air flow was influenced. However contactless actuation of a flying wafer in multiple directions was observed in a very limited sense. Wafers with a thickness of 6 mm have been made with various diametres from PMMA. Tilting of the wafer, as a result of actuation was seen frequently. The tilting resulted in contact with the actuator and minimal actuation, since the friction forces were dominant over the actuator forces. The tilting originates from an uneven pressure distribution, which is a result of actuation.

The first step to improve the behaviour, was an attempt to increase the allowable tilt angle. This has been done by milling material from the top plate in such a way that the dams were elevated above the surface of the top plate. Material has been removed at the hatched locations outside a circle with a diameter of 40 mm, which can be seen in figure 5.1. Moreover, it is clear that the tilt angle can be increased. Afterwards the flatness of elevated dams has been measured with the same white light interferometer as in chapter 4. After a flattening operation the edges of the elevations were deburred using a manual grinding operation. The final surface profile can be seen in figure 5.2, the influence of the grinding can be seen. Excluding the lowered edges, a peak to peak distance equals to 8 μm has been realised.

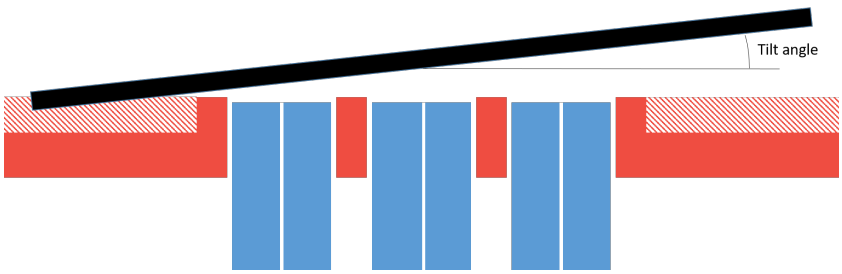

Figure 5.1: Elevation of dams to increase maximum tolerated tilt angle, hatched parts are removed with a lathe.

Another very crucial step involved the introduction of a new type of wafer. The initial wafers had been made from a plate of PMMA, which was expected to be flat. However, after replacing the PMMA wafers with a mirror, actuation in all planar directions was possible. A mirror is known for its nearly perfect flatness. Moreover, tilting was observed to a lower degree, which suggest that the tilting is related to the flatness of the wafer. Due to the improved results, it has been decided to continue with a mirror as wafer. A mirror with a diameter of 45 mm, which is slightly larger than the elevated area, is chosen.

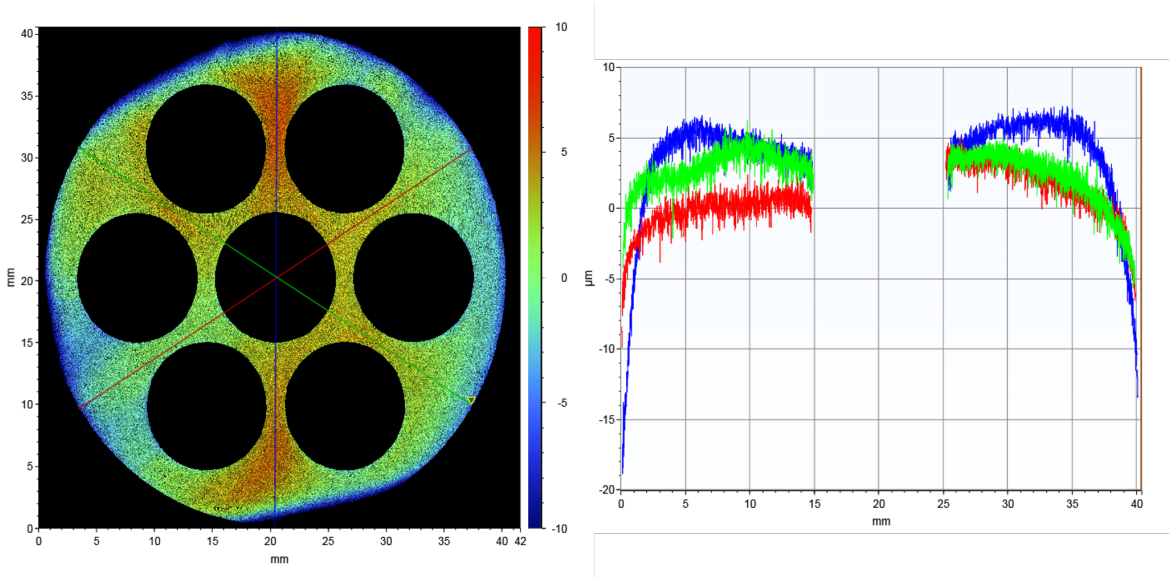

Figure 5.2: Surface profile of the elevated dams on the top plate, measured with the white light interferometer. Excluding the grinded edges, a peak to peak flatness of 8 μm has been obtained.

5.2. Measurement setup

5.2.1. Force

A force measurement will be done using Newton's second law. Using a high-speed camera the accelerations will be investigated which gives information with respect to the generated actuator force. The actuator will be actuated by hand until one of the pins makes contact with the top plate. A rotation of the mirror will be initiated rather than a translation, since rotating has no stroke limitations. Translations does have stroke limitation and therefore it will be challenging to extract enough data from a video. A downside however is that the mirror has to be constrained, meaning that three end stops have been placed around the mirror to ensure that the mirror keeps rotating above the actuator, see figure 5.3. On the mirror itself some markers have been placed to increase the contrast which makes analysis of video frames easier. The high-speed camera, a Casio Exilim EX-F1, was set at a shutting speed of 300 frames per second. Afterwards the open source video analysis software "Tracker" was used to obtain the x and y coordinates of the marker during actuation [8]. The angle is derived from the obtained x and y coordinates and accumulated over time, meaning that angles larger or smaller than respectively π and $-\pi$ will be obtained. Using the time difference between two frames (1/300 s) the velocity can be calculated. And from changes in velocity over time the angular accelerations can be found.

5.2.2. Fly height

Fly height will also be measured since it is a crucial variable for the performance, measurement will be done with an electronic dial indicator. An indicator, from the brand Mitutoyo with model number 543-250B and micro meter accuracy will be used. Measurements showed a zero stiffness of this device however a constant force around 1 N was measured, which corresponds to the manufactures specifications. The mirror will be placed on top of the actuator after setting the pocket depth. The vacuum source will be connected while pressure is not, which means contact and zero fly height. In this situation a first measurement is done. Afterwards the pressure source is connected which means that the air film will be created and the mirror will be lifted. A second measurement is done and the fly height can be calculated as the difference between both measurements. The force from the dial indicator is neglected in these measurements, since measurements with an added mass (130 g) on top of the mirror resulted in an equal fly height.

5.2.3. Pocket depth

An attempt to measure the pocket depth, defined with β and h_0 in this report, will also be done. It is crucial to perform this measurement with equal vacuum and pressure source as the actuation is done. The reason for this is that the pressures levels affect the pocket depth. The bottom plate will bend as a result of the high pressure, see figure 3.5, the vacuum pressure has a limited influence on the bending as well. Moreover, due

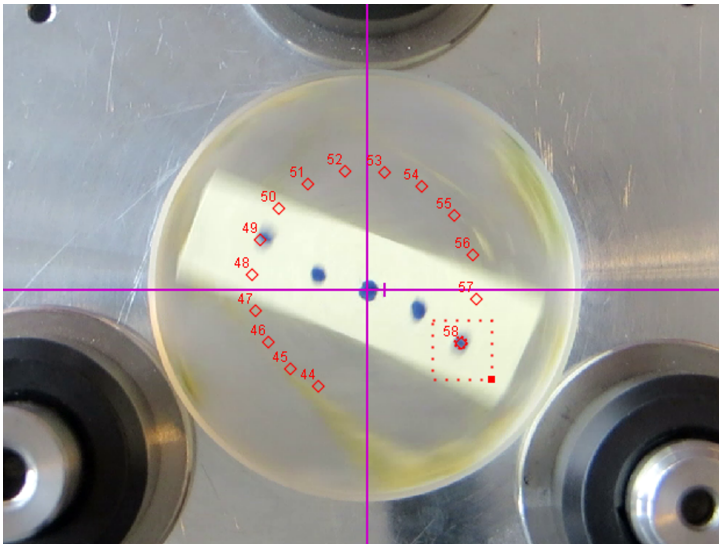

Figure 5.3: A screenshot from the open source video analysis software "Tracker". The origin in purple has been placed at the centre of the mirror, three boundary limits have been placed around the mirror to ensure the position. Markers have been placed on the mirror to increase contrast. The software marks the position of the dot for every frame.

to the vacuum pressure in the chamber between the top and bottom plate a significant compressive force is loaded on the three wire flexures. This force will lead to a compression of the wire flexures in the order of micrometres. Lastly, the pressure distribution between mirror and actuator does have a weakening effect on the influences just named.

By rotating the threaded rods the pocket depth can be adjusted, it can roughly be verified by laying a straight-edge (Dutch: haarliniaal) on the setup and investigating the light that protrudes through the gap. Visually it will be verified whether the gap widths are in the same order of magnitude. For a more precise measurement of the pocket depth the electronic dial indicator will be used again. Due to the relation between pocket depth and available pressures, this measurement should be done with the pressure that will be used during the actual actuation, which means that the mirror should be flying as well. Presence of the mirror and measurements of the pocket depth with the dial indicator can unfortunately not be combined.

An alternative to measure the pocket depth is a measurement without mirror, a shortcoming of this option is that the actuator is not loaded as it would be during actuation. Moreover, the absence of the surface restriction results in a lower restriction from the pressure source to ambient, which means a higher mass flow will be created for the same vacuum pressure. The vacuum source however is limited in terms of mass flow and therefore the vacuum pressure level cannot be sustained for all vacuum pressures after removing the mirror. The maximum vacuum pressure without mirror turned out to be 75 kPa, thus 25 kPa lower than ambient pressure. Therefore, the limit on the vacuum source has been set to this level. A downside is that actuation at a lower vacuum pressure results in a lower actuator force.

The electronic indicator will be placed on a stage with one translational degree of freedom that can be controlled manually, see figure 5.4. Since it cannot be assumed that the tip of the indicator moves in the same plane as the surface where the actuator is positioned, a double measurement on both sides of the pocket is necessary to compensate for the error. The elevated surface including the seven pins can be seen in figure 5.4. The red dots indicate the location of the measurements, the single degree of freedom stage will be used to move the actuator along the red lines. The average of both pocket depth measurements will be taken as the pocket depth. All measurements will be done ten times, such that every average fly height is based on twenty measurements.

5.3. Results

The measurements described in the previous section have been done, the results will be presented below. The results have been obtained with a vacuum source equal to 75 kPa absolute pressure, thus 25 kPa lower than ambient pressure. This is the maximum pressure level that can be sustained after removing the mirror, until this pressure level the pocket depth can be verified with some certainty with the method described above. COMSOL was consulted to find an interesting pressure source and pocket depth combination. It has

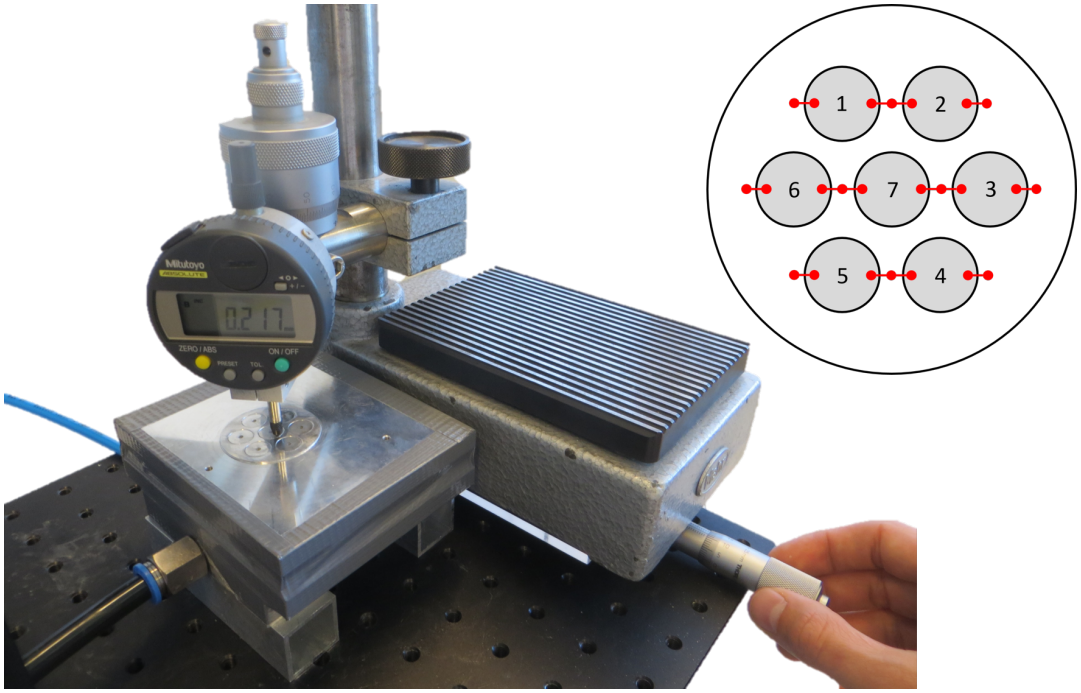

Figure 5.4: Pocket depth measurement setup using a manually controlled one degree of freedom stage and an electronic dial indicator with micrometer precision. The actuation lines and measurement location are schematically visualised in the upper right.

been decided to pursue a situation where the fly height is expected to remain constant throughout the full range of actuation, since in this situation measurements can be compared easier with the model, also if the concentricity is unknown. Figure 5.5 has been obtained with a fixed fly height of 10 μm and a corresponding pressure source found by COMSOL for a load equal to the weight of the mirror 39.5 gr. The rotation ratio has not been introduced yet, this ratio indicates how much of the ideal gap width (50 μm) is used for rotation. A rotation ratio of zero means that no rotation is actuated and a ratio of 1 means maximum rotation is actuated, the definition is comparable to the actuation ratio. From the figure it can be seen that a pocket depth of 27 mu gives a steady absolute source pressure equal to 3.6 bar for a large range of the actuation ratio. A constant pressure, when solving for pressure, indicates a stable fly height. Therefore, 3.6 bar has been chosen as the pressure source for the actuator.

Pressure and vacuum source were set to the levels described above using manually controlled proportional valves. A dial indicator on those valves has been verified visually to obtain the correct pressure levels. From a situation with zero pocket depth, obtained via trial and error with the straight-edge, the threaded rods were rotated to create the desired pocket depth. Since the lead of the threaded rod (M4) is known the required rotation was determined. It turned out that actuation was not possible since slight contact between mirror and actuator was present, meaning that the 10 μm fly height was chosen too small with respect to the tolerances on the flatness of mirror and actuator. To increase fly height, the pocket depth has been reduced until satisfying contactless actuation was possible, afterwards the pocket depth was measured. The measured pocket depths can be found in table 5.1, measurements have been done according to the method described in the previous section. Note that the mean standard deviation as well as the standard deviation over all measurements, which is between brackets, have been given. The mean standard deviation gives information regarding the accuracy of the measurement per pocket, the latter combines the accuracy of the measurements and the pocket depth difference per pocket. It should be noted that both values are rather high. The fly height had been measured as well, based on fifteen measurements the average fly height was 19.0 μm with a standard deviation of 1.46 μm.

Table 5.1: Measured pocket depth and standard deviation per actuator pin.

Actuator	**1**	**2**	**3**	**4**	**5**	**6**	**7**	**Mean**
Pocket depth [μm]	21.1	20.8	17.7	23.0	16.2	16.7	18.4	19.1
Standard deviation [μm]	4.4	3.4	2.8	3.4	3.1	2.3	3.1	3.2 (4.0)

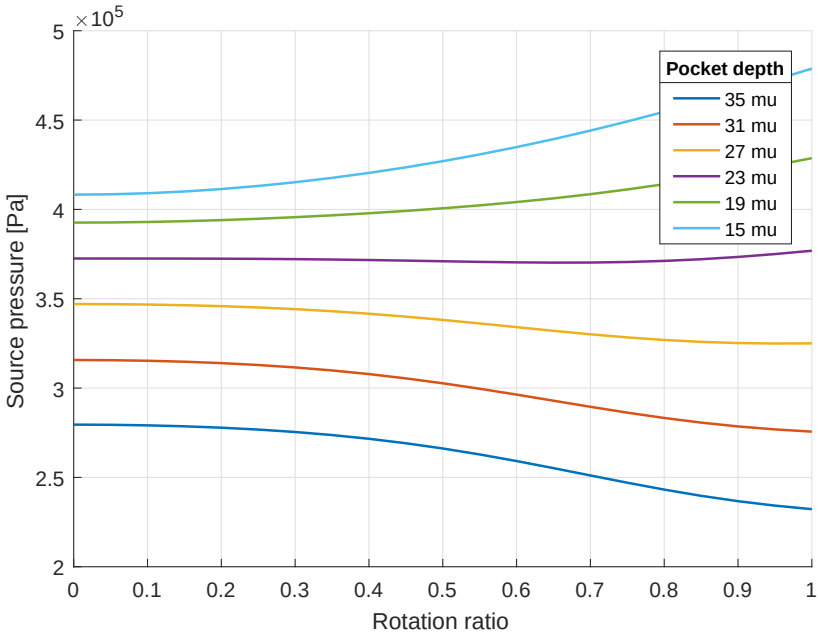

Figure 5.5: Source pressure for varying rotation ratio and pocket depth. A constant source pressure is preferable.

Using the measurements procedure described above the angular acceleration has also been derived. Some results can be seen in figure 5.6. As can be seen, the mirror has been rotated both ways multiple times. The data for the angle has been smoothed with a 25 points moving average. From this smoothed curve the angular velocities have been derived. The velocity curve has been fitted with a linear interpolation at multiple parts of the velocity graph. The angular accelerations based on these linear interpolations can be seen in figure 5.6. Moreover, the accelerations based on a smoothed velocity curve can also be seen. To obtain the acceleration curve the velocity curve has been smoothed using a 50 points moving average. The accelerations found with both methods do match reasonably. The values for angular accelerations and de-acceleration obtained after the interpolation can be found in table 5.2.

Table 5.2: Angular accelerations based on the linear interpolated angular velocity

Time [sec]	**0.8**	**2.6**	**3.2**	**5.3**	**5.7**	**7.7**	**8.8**	**11.6**	**12.2**
Angular acceleration [rad/s^2]	6.2		-5		6.4		-4.5		7.4
Angular de-acceleration [rad/s^2]		-11.1		16.3		-12.1		14.7	

Investigating figure 5.6 and table 5.2, it can be seen that different angular accelerations are present. Different accelerations were found per rotation direction and between two accelerations in the same direction. An initial explanation can be found in the fact that the actuator is manually controlled. Due to this the acceleration levels can vary due to a different rotation ratio. Another factor that can be influencing is that translation is actuated next to a rotation, this would result in a lower angular acceleration, since more and stronger collisions between mirror and boundary stops are present. Moreover, the concentricity of the actuator pins and holes is not perfect, meaning that maximum angular rotation per rotation direction can be limited, due to contact between pins and top plate.

Another interesting detail is that two acceleration levels have been found within a single acceleration. The acceleration level lowers at the moment that the rotation direction changes, this means that the angular acceleration is rotation direction dependent. According to the Reynolds equation, given in appendix A, this is correct. However, the magnitude of the velocity is important as well in this case. It has been assumed that the velocities are low enough such that this can be neglected. A rotation of 10 rad/s gives a velocity of 0.24 m/s at a radius of 12 mm, which is the radius of the circle at which the inlets are placed. Flow velocities are in the order of dozens of metres per second for this concept, thus the assumption of low angular velocities seems correct for the measurement shown in figure 5.6. Moreover, the turning point in terms of angular velocity is already visible at zero velocity, thus the velocity difference cannot explain the acceleration reduction around

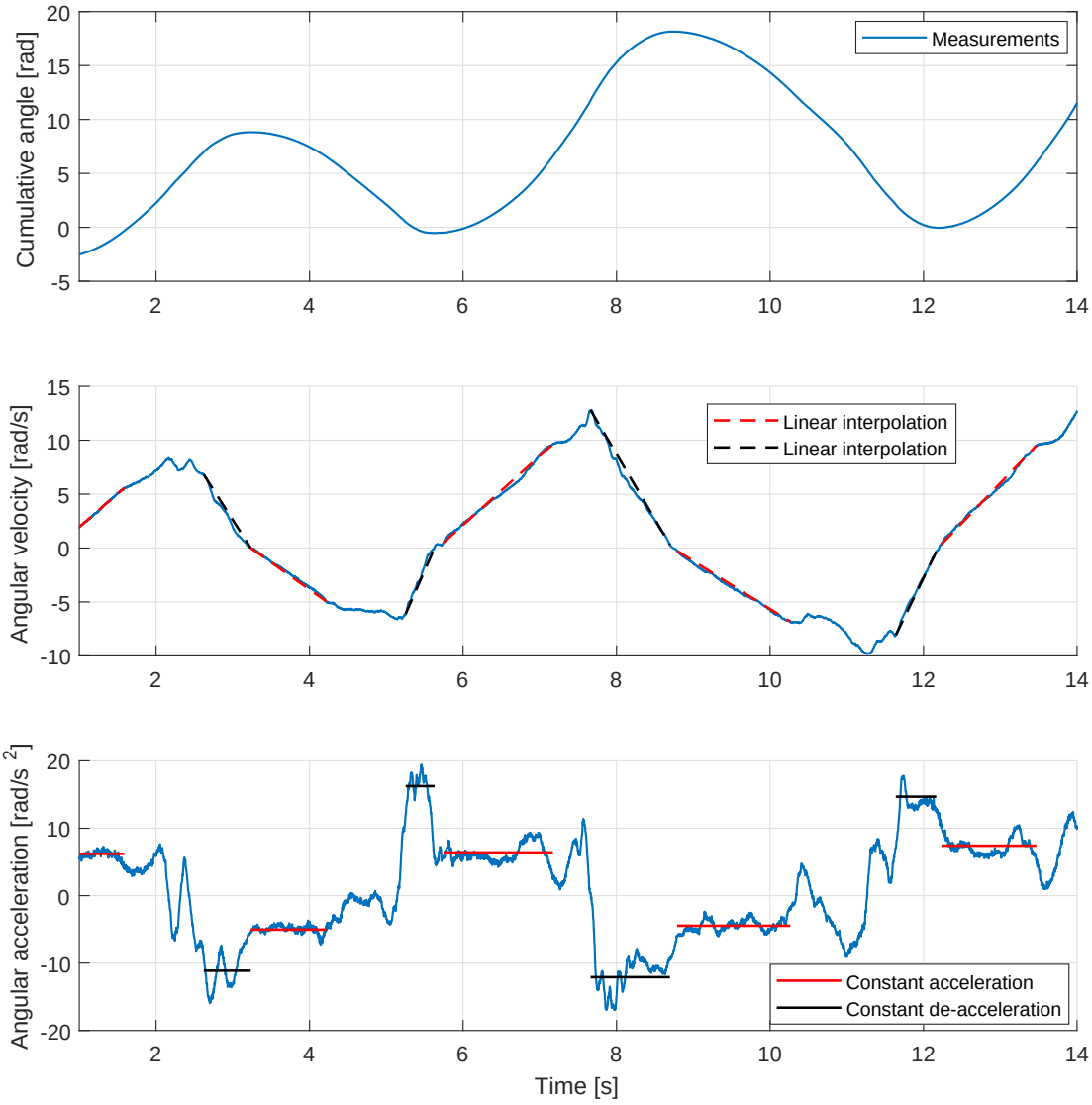

Figure 5.6: Accumulated angle, angular velocity and angular acceleration based on measurements.

zero velocity. Therefore, friction between mirror and limit stops is seen as the most important influencer in the acceleration step. The friction helps the rotating mirror in de-accelerating and prevents ideal acceleration once the rotation direction has been switched. This means that the actual rotational force of the actuator generates a force equal to an angular acceleration between the two accelerations found. Assuming that the influence of friction is equal during acceleration and de-acceleration the actual force generated by the actuator can be found using the average of both accelerations. The validity of this assumption is unknown, however it can be stated with certainty that the actual force generates an acceleration in between the two accelerations.

5.4. Comparison

In this section, the obtained results from measurements and modelling will be compared. First the combination between pocket depth and fly height will be investigated. Afterwards the obtained accelerations will be compared with the theoretically possible accelerations.

With the measurements described above a fly height was found equal to 19.0 μm with a standard deviation of 1.46 μm. The pocket depth was measured less accurately at 19.1 μm with a standard deviation of 4.0 μm, see table 5.1. Using the COMSOL model a nearly linear relation between pocket depth and fly height has been

found for the used pressure and vacuum source, see figure 5.7. The measured values for the fly height and pocket depth can also be seen in the figure with their corresponding standard deviations. The combination between fly height and pocket depth does not match the obtained measurements results, however taking the standard deviations into account a decent match is obtained.

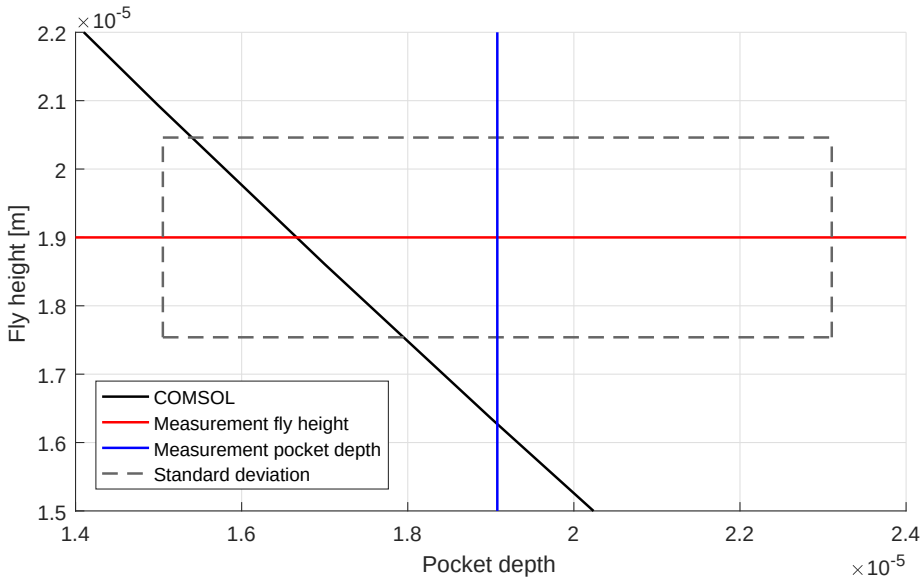

Figure 5.7: Pocket depth and fly height measurements including standard deviations compared with the numerically obtained relation between fly height and pocket depth from the COMSOL model.

The next step involves a comparison between measured angular acceleration and predicted angular acceleration. In the previous section different accelerations have been found. In this section, the focus will be placed upon the last acceleration and de-acceleration from figure 5.6, since the angular accelerations found during this actuation step turned out to be the highest. The angular acceleration was equal to 7.41 rad/s^2 and the de-acceleration equal to 14.68 rad/s^2, which leads to an average acceleration of 11.0 rad/s^2. Those three values can be seen in figure 5.8, moreover the angular accelerations theoretically possible for a given rotation ratio have been plotted for a range of pocket depths around the measured pocket depth. Assuming that averaging of the acceleration and de-acceleration is justified as well as that all pocket depths were equal to 19.1 μm, more than 67% of the theoretically maximum acceleration is obtained. Keeping in mind the deviations of the measurements and the tolerances of the manufacturing process, the author realises that this percentage has a large error margin. Moreover, it should be noted that this percentage has been derived from the maximum acceleration found for a setup with a certain pocket depth, pressure and vacuum source, nothing can be concluded about other configurations of the actuator. Besides, inaccuracies of the fly height and pocket depth measurements increase the error margin. Moreover, pressure levels have been set by hand using proportional valves, which means that the pressure levels obtained could differ from the indicated. Keeping these factors in mind the only claim that can be made is that the numerical model predicts forces in the same order of magnitude as those that have been measured.

A percentage of 100% would mean that model and measurements do match, especially the off-centre ratio, discussed in section 3.5, is seen as a limiting factor obtaining this maximum performance. Moreover, it should also be noted that the accelerations varied depending on actuation direction, table 5.2 showed a significant difference for acceleration and de-acceleration for both actuation directions. This results in a maximum percentage, derived similarly as the percentage above, around 49% for actuation in the less beneficial direction. This finding supports the theory off concentricity, apparently the pins are positioned in such a way that the maximum rotation ratio is depending on the rotation direction.

To put the found angular accelerations in perspective with the state of the art, the angular acceleration has to be transferred to a translational acceleration. The second moment of inertia for the circular mirror can be calculated since its weight and radius are known. This means that the torque created by the actuator can be found using Newtons second law and the assumption that the arm of the torque is equal to the radius of the circle on which the six outer inlets are placed. Since the actuator in the middle does not contribute to

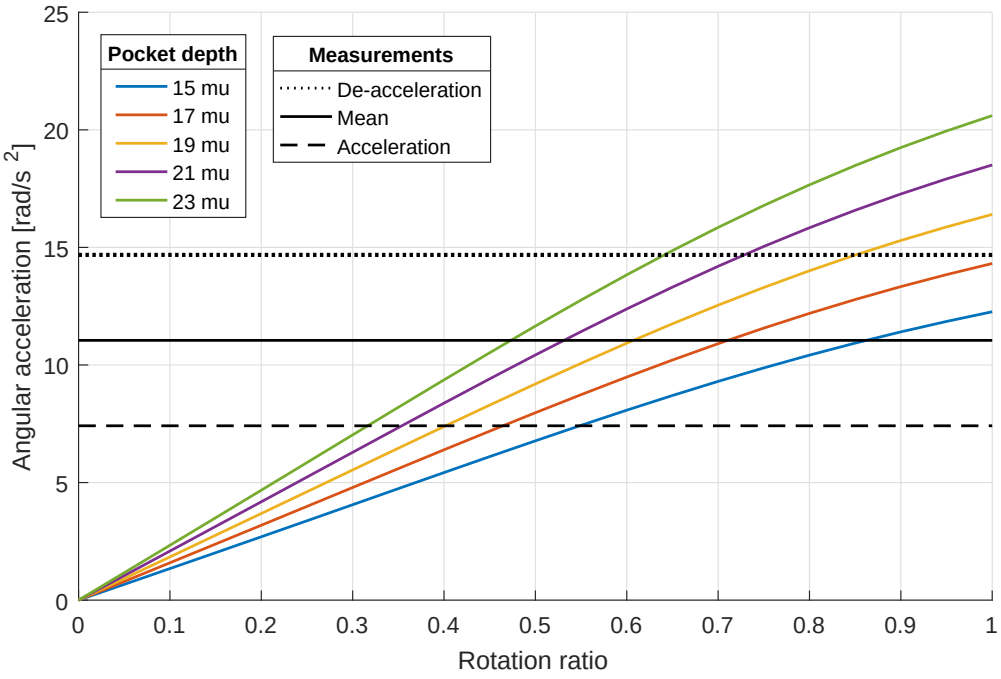

Figure 5.8: Angular acceleration from COMSOL in relation with the maximum accelerations measured.

the angular accelerations, the force found should be multiplied with 7/6 to obtain a translational force. The wafer that has been used in the study of Krijnen [17] had a diameter of 200 mm and a mass equal to 60 g. With a theoretical wafer, with the same density, having a diameter equal to the elevation of the created stage (40 mm), the translational accelerations can be obtained using Newtons second law again. An acceleration equal to 2.8 m/s^2 is found, which is more than double than the measured accelerations for the Flowerbed (1.2 m/s^2).

5.5. Conclusion

In this chapter, the experimental validation of the created outlet restriction variation concept has been discussed. Based on initial test results, an extra milling operation has been done to increase the allowable tilting angle. Moreover, the usage of a different wafer, namely a mirror, which is known for its flatness, increased the performance significantly. The next section in this chapter described the measurement procedures to measure the angular acceleration, fly height and pocket depth. A high-speed camera in combination with an open source video analysis software was used to capture the location of the mirror over time. Taking the derivative of the obtained position twice, the angular acceleration was found. The pocket depth and fly height have both been measured with an electronic dial indicator. The obtained combination between pocket depth and fly height showed a good comparison with the numerical model. Found angular de-accelerations were higher than accelerations, friction is seen as the reason why the de-accelerations are higher. Combining the highest acceleration and de-acceleration, the average angular acceleration was higher than 67% of the theoretically maximum. This is seen as a good result since tolerances on manufacturing, especially the off-centre placement of pins and holes, reduces the maximum forces significantly. Moreover, it should be said that that the configuration and pressure levels were done by hand causing uncertainties. Besides the measurements do have a significant standard deviation. Combining all these results and uncertainties in the comparison between measurements and model, it can be stated that the actuator behaves as expected with values found in the correct order of magnitude. Although no strong claim can be made, the results make it likely that the model is correct and differences between model and setup are caused by manufacturing tolerances.

6

Conclusions and recommendations

The last chapter of this research is fully focussed on the conclusions that can be drawn and the recommendations that can be given based on the findings in this research. The recommendations are split in two sections, recommendations for the created outlet variation concept and general recommendations for contactless actuation using a thin air film and the outlet variation concept.

6.1. Conclusions

- Solar panel production is reaching its limits with conventional handling. Contactless handling can lead to a further decrease of panel thickness and silicon usage, which leads to a reduction of solar panel prices. Moreover, the risk on contamination can also be reduced.
- There is potential in the state of the art with respect to air-based contactless handling. The pressure variation concept is limited in terms of bandwidth and the manufacturing of the deformable surface concept is problematic. Moreover, both concepts do have significant vacuum flow losses when no object is flying above the actuator.
- A new air based contactless handling concept is introduced. It fulfils the bearing and motor function with the same air film. The average pressure in the film decides the load capacity and viscous forces are used to actuate the object. A variation of the outlet restriction 'steers' the net air flow.
- The performance of the outlet restriction variation concept is similar to the state of the art: the stepped and tilted surface concepts. This is positive since the benefits of this concept are mainly seen in terms of bandwidth and manufacturability.
- The outlet restriction concept is a versatile concept that can be tuned to many different working conditions. The concept can be tuned to a high performance ratio or limit. Moreover, a stable fly height and a linear force actuation curve are also possibilities. Generally, it has been seen that a smaller gap width, a lower fly height and a larger actuator are beneficial for the performance and a linear force behaviour. However, decreasing gap widths and fly height will lead to manufacturing challenges and increasing the actuator size is limited due to allowable stresses in the object.
- The Fanno flow theory is able to predict the resistance of capillary restrictions. The match between theory and measurements is quite good after updating the estimated friction factor based on experimental data.
- A contactless stage based on the outlet variation principle has been designed and manufactured. Seven actuator pins were connected to a bottom plate. Those pins do line up with seven slightly larger holes in a top plate, the combination of pins and holes creates an average gap width of 50 μm. The outlet variation can be done close to the surface which is beneficial for the bandwidth. Flatness and concentricity are two focus areas during manufacturing.
- A tolerance on concentricity between pins and holes, leads to the off-centre placement of pins which limits the maximum force since the actuation ratio will be reduced. Moreover, assuming that the pins

are placed off-centre in all possible directions, then the average influence of the off-centre placement will make the force actuation curve more linear, which is a positive side effect.

- Forces in all planar directions can be created with the outlet restriction variation stage. This is concluded since bidirectional actuation in two translational direction and bidirectional rotation has been observed.

- The pocket depth and pressure levels have been adjusted to a configuration with satisfying performance. Pocket depth and fly height are measured with an electronic dial indicator. Fly height was equal to 19.0 μm with a standard deviation of 1.46 μm. Pocket depth was 19.1 μm with a standard deviation of 4.0 μm. Angular measurements are also done with this configuration

- A maximum angular accelerations of 7.4 rad/s^2 and a nearly double angular de-acceleration of 14.7 rad/s^2 have been observed. This is measured with a high-speed camera and open source video analysis software. This contactless method is easy to use and can be interesting for other motion capture purposes. Friction is seen as the cause of the difference between angular acceleration and de-acceleration. The average angular acceleration of 11.0 rad/s^2 leads to a theoretical translational acceleration of 2.8 m/s^2 of a 200 mm wafer, which is more than double than the state of the art.

- The measurements showed a reasonable comparison with the numerical model. The averaged acceleration of 11.0 rad/s^2 is equal to 67% per cent of the theoretical angular acceleration. Although no strong claim can be made due to inaccuracies, it is likely that the model is correct and that the difference between numerical model and setup are caused by manufacturing tolerances. Especially the concentricity of pins and holes is seen as a problem.

- The **final conclusion** is that the outlet restriction variation concept is a promising concept. After four phases of research involving concept exploration, actuator design, design realisation and experimental validation benefits are seen compared to the state of the art in terms of bandwidth, manufacturability and vacuum flow losses.

6.2. Recommendations

In this section, some recommendations will be done to increase the potential of the outlet variation concept. The first recommendations are mainly focussed on obtaining more data around the created setup such that the model can be updated and the experimental validation can be improved. The second set of recommendations involves some analyses and manufacturing recommendations for future outlet variation stages.

- Improve the way to verify the pressure levels at vacuum and pressure source, this is done manually and visually verified on a pressure gauge. A calibrated electronic pressure sensor would be a better alternative, since it has been seen that the pressure levels do have a great influence on the performance.

- Improve the restriction measurements by verifying the temperature level in the tank. The measurements showed an unexpected start up behaviour which could be related to the air temperature in the tank which is assumed to be constant at the moment. Moreover, it would also be interesting to verify the outlet restriction, due to the sealing with tape this has not be done.

- Try to find a method that is able to measure the exact surface profile. The pocket depths have now be measured using a dial indicator, the average pocket depth is fed back in the model. It would be a great step forward if the surface could be measured with for example a white light interferometer while the actuation pressure levels are applied to the setup. At the moment the actuation has been limited to 0.25 bar relative vacuum pressure since the measurement of the pocket depth could not be done with higher vacuum pressures. Moreover, this measurement can also improve the inlet pocket depth modelling, which has been modelled at a constant depth of 0.1 mm.

- Improve the force measurement, this could be an angular or translational measurement. It turned out that friction influences acceleration and de-acceleration levels. An example of a force measurement without the influence of friction would be to attach a force sensor to the flying object. Attachment of this force sensor can be complex since tilting should be avoided.

- Try to measure the actual gap widths surrounding the actuator. A proper measurement is able to measure the level of concentricity as used in this report, but it should also be verified whether the hole and actuator pin are placed coaxially.
- A final recommendation to improve the experimental validation, involves the advice to compare a measured stiffness with a calculated stiffness. Stiffness could be measured by verifying the fly height for different weights placed on the actuator. A quick measurement with an extra weight on top of the mirror showed no significant difference, this means higher loads should be used or the fly height measurement should be improved.

The next set of recommendations are focussed on improvements of the actuator setup created in this research or involve advise for future outlet restriction variation stages.

- Model and verify the dynamic behaviour of the actuator. The benefits in terms of bandwidth are seen since the restriction variation is done close to the surface, however this has not been verified. Moreover, the dynamic analysis can lead to a prediction regarding expected pneumatic hammer. In this research dynamic effects have been neglected, however at high vacuum pressures and a higher load on the actuator pneumatic hammer has been observed with the outlet restriction variation stage.
- Increase the number of actuators in a future stage, this will lead to more information regarding manufacturability of this concept. In this research an actuator has been made with seven actuator pins, this did not lead to severe complications in terms of alignment of pins and holes. Increasing the number of actuator pins might change this situation.
- Improve a future outlet variation stage with actuators and a control system. This means that a stage without limit stops can be made and thus can the effect of friction between flying object and limit stops be eliminated. Moreover, once actuators and a corresponding control system have been implemented it will be easier to determine the bandwidth limitations.
- Manufacture the bottom plate including actuator pins as a single part. This can eliminate post processing manufacturing steps. Examples of manufacturing methods that could be relevant are a die sinking process as well as CNC machining.
- Include a thread on the actuator pins and drill/ream the top and bottom plate simultaneously if the bottom plate could not be made as a single part as described in the previous recommendation and conventional machining is chosen as production method. Making holes with an equal diameter simultaneously will improve the concentricity. Some offer material should be placed between both plates such that the chips can be taken away, see figure 6.1. The actuator pin should then be made with two precisely defined different diameters, see figure 6.2. The thread and end stop ensure that no glue is required and that high pressure levels can be obtained.
- Add porous material in the outlet restriction gap. Including this material could allow the gap width to increase while a similar outlet restriction is necessary. This will greatly improve the manufacturability of the top and bottom plate since lower tolerances can be kept. A challenge however is to find a flexible porous material that gives repeatable restriction levels. Perhaps woven wire cloth can be used, which has been characterized by Belforte [5].

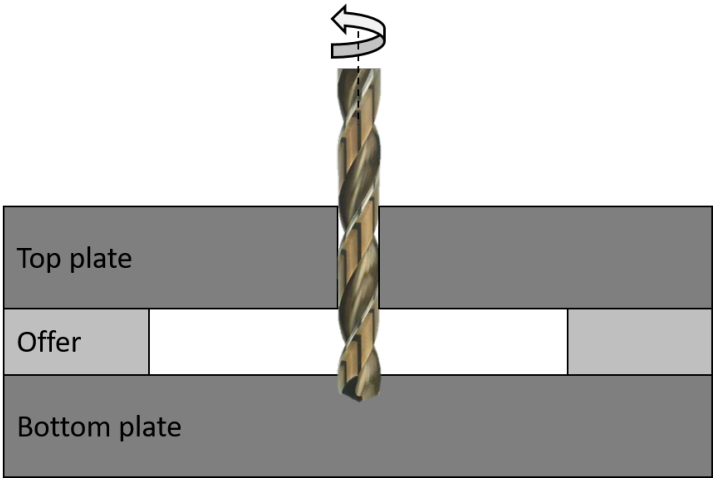

Figure 6.1: Simultaneously drilling of same diameter holes.

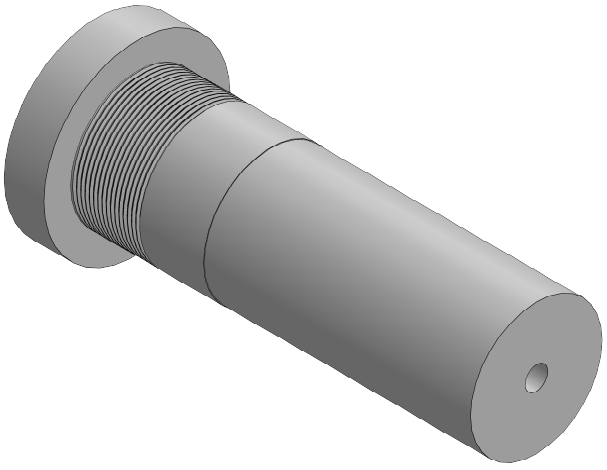

Figure 6.2: Pin with thread and two diameters.

A

Reynolds equation

Let us start with some history first. Hydrodynamic lubrication has been observed experimentally by Beauchamp Tower in 1883 [34] for the first time. He was an English rail road engineer who tried to simulate the conditions in railway axle boxes. A schematic representation of his experiments can be seen in figure A.1. The upper half of the axle was loaded with a weight, while the lower half of the axle was submersed in lubricating oil, this method is called oil bath lubrication. Oil adhering to the axle surface is pulled up by rotation of the axle, which brings the oil between the axle and load. When Tower drilled a hole in the bearing, initially for the supply of lubricating oil, he found out that after starting rotation of the shaft the oil would rise in the hole and eventually would spill out of it. With a pressure gauge on the hole, Tower showed that in the drilled hole a significant oil pressure can be created. These experiments led to a new explanation of the low friction in oil bath lubricated bearings. So far, it was accepted that the lubricating oil smoothens the (partial) contact between the axle and load. However, based on these experiments Osborne Reynolds [26] created a new theory assuming that the load was carried by a thin film of lubricating oil, which lowered resistance since no direct contact was present any more. The assumption of a thin film flow surrounding the axle led to a simplification of the Navier Stokes equations for thin film flows, which is known as the Reynolds equation.

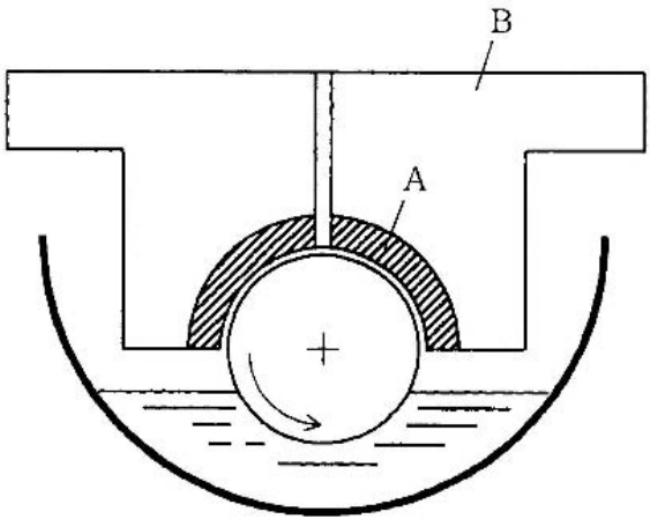

Figure A.1: Schematic representation of Beauchamp Tower's test rig. A, bearing bush; B, bearing cap or load. Rotation is lubricated using oil bath lubrication [14]

.

The general Reynolds equation can be derived from the Navier Stokes equation and is given below. The derivation, starting with a balance of forces in a flow element, can be found in literature, for example [14, 29].

$$\frac{\partial}{\partial x}\left(\frac{\rho h^3}{12\mu}\frac{\partial p}{\partial x}\right)+\frac{\partial}{\partial y}\left(\frac{\rho h^3}{12\mu}\frac{\partial p}{\partial y}\right)-\frac{\partial}{\partial x}\left(\frac{\rho h(u_1+u_2)}{2}\right)-\frac{\partial}{\partial y}\left(\frac{\rho h(v_1+v_2)}{2}\right)=\rho(w_2-w_1)-\rho u_1\frac{\partial h}{\partial x}-\rho v_1\frac{\partial h}{\partial y}+h\frac{\partial \rho}{\partial t} \tag{A.1}$$

where:

- p is the fluid film pressure
- x and y the bearing width and length coordinates
- z is the fluid film thickness coordinate
- h is the fluid film thickness
- μ is the fluid viscosity, assumed to be constant in this report.
- ρ is the fluid density
- u, v and w the body velocities in x, y and z respectively.
- 1 and 2 are the denotations of the bounding bodies see figure A.2.

The first two terms on the left hand side of the Reynolds equation represent Poiseuille flow, which is a pressure driven flow type. The next two terms represent the Couette flow, which is a flow generated by surface velocities. The wedge and stretch effects are described by these terms. The first three terms on the right hand side of the equation describe the squeeze effect, which is induced by normal motions of the bounding surfaces. The last term on the right hand side represents the local expansion term, caused by a varying density over time.

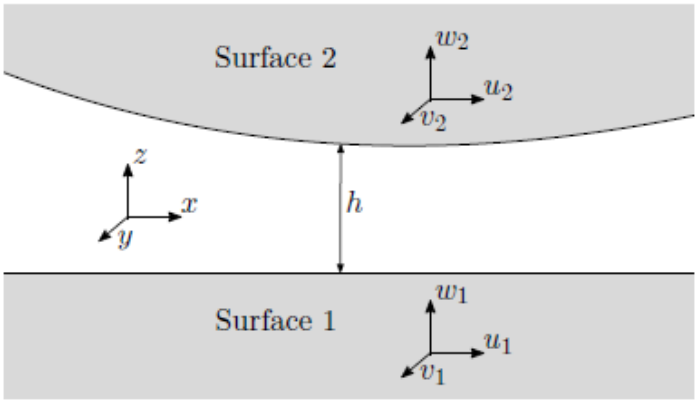

Figure A.2: Thin fluid film between two surfaces, moving with velocities u,v and w in a Cartesian coordinate system. [29]

While deriving the Reynolds equation some assumptions have been made. For the sake of completeness they will be stated here.

- Body forces within the fluid film are neglected. Body forces can originate from gravity or electric fields for example.
- Constant pressure is assumed throughout the film height. The reason for this is the small film height compared with the film length making the pressure differential in height negligible.
- No slip boundary conditions have been implemented, meaning that surface and fluid have the same velocity at their interface.
- The fluid behaves as an Newtonian fluid. This indicates that shear stress is linear proportional with the velocity derivative
- Laminar flow is assumed.

- Fluid inertia is neglected, which can be verified with the Reynolds Number.
- Constant temperature is assumed throughout the air film, resulting in an isothermal assumption.
- Fluid viscosity is assumed to be constant, this assumption holds quite well for gasses. The viscosity of some oils is dependent on temperature, however with the isothermal assumption in place, this can also be neglected.

After solving the Reynolds equation for a specific situation the pressure distribution can be obtained for a fluid film. After Reynolds' discovery, many types of fluid film lubricated bearings have been developed for an even wider range of applications. Fluid film bearings can be characterized on different criteria. A first distinction can be made on the phase of the lubricant. Fluid film bearings using a liquid lubricant, denoted with the prefix 'hydro-', can be distinguished from bearings using air as lubricant, with the prefix 'aero-'. Considering pressure generation, two types of bearings can be identified. Pressure can be generated by relative movement of bearing surfaces, which is the case in Tower's experiments. This type of pressure generation is labelled with the suffix '-dynamic', while externally pressurized bearings us the suffix '-static'. A final distinction can be made with respect to the guidance type. Linear, cylindrical and spherical are the most common.

This study focusses on linear aero static bearings, where an external pressure and vacuum source will push/pull air through a small gap between parallel plates. In this research the assumption is made that the velocities of the bounding bodies are low compared to the air flow velocities, meaning that no Couette flow will be present, therefore the wedge and stretch effects can be neglected. Moreover a constant fly height is also assumed over the whole surface, meaning that also the squeeze effect can be neglected. Finally a steady state analysis will be done, meaning that the local expansion term can be left out as well. This simplifies the general Reynold's equation even further, since the Couette terms and the complete right hand side of equation A.1 reduce to zero, resulting in the following simplified Reynolds equation:

$$\frac{\partial}{\partial x}\left(\frac{\rho h^3}{12\mu}\frac{\partial p}{\partial x}\right)+\frac{\partial}{\partial y}\left(\frac{\rho h^3}{12\mu}\frac{\partial p}{\partial y}\right)=0 \tag{A.2}$$

B

Inlet restrictions

Restriction theory can be explained very well using Ohm's law for electrical current flow through an resistance. Ohm's law states that the potential difference (voltage) across an ideal conductor is proportional to the current through the same conductor. The constant of proportionality is called the resistance (R). Pressure difference ($p_1 - p_2$) relates to the potential difference, if the volumetric flow ($\dot{q}$) is coupled to the current and the electrical resistance to the air flow restriction, see figure B.1 and equation B.1.

$$R = \frac{p_1 - p_2}{\dot{q}} \tag{B.1}$$

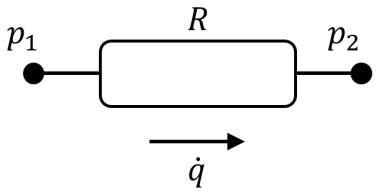

Figure B.1: Resistance to air flow an its similarities to Ohm's law.

Three types of restrictors are commonly used to restrict air flow: Porous, orifice and capillary restrictions. The difference between them is the geometric representation of the obstruction created. A porous restriction derives its resistance to air flow from an irregular pattern of mostly open structures. The capillary and orifice restriction limit the air flow due to a reduction in flow area, for example a reduction in diameter for pipes. The difference between the latter two is the ratio of length over diameter of the hole l/d, see figure B.2.

To estimate the pressure drop over a restriction, one should know which forces are dominant. Viscous forces, which are related to laminar flow and low Reynolds numbers, are dominant for low velocities relative to the diameter of the relevant pipe. For higher velocities relative to diameter the Reynolds number will increase and the inertia forces become more important, although frictional forces could still play an important role depending on restrictor geometry.

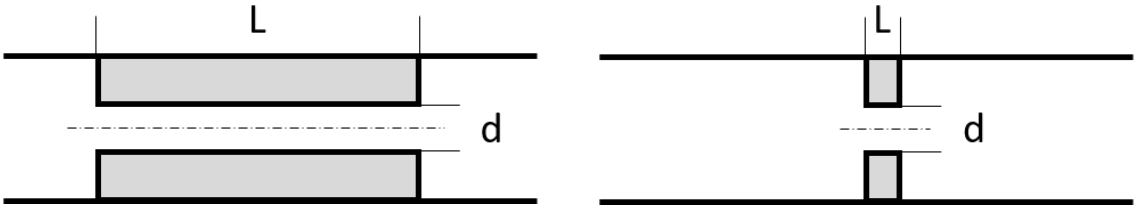

(a) Capillary restrictor

(b) Orifice restrictor

Figure B.2: The main difference between the orifice and capillary restrictor in terms of the geometry is the ratio l/d.

B.1. Porous restriction

For a porous material the resistance to viscous fluid flow is depending on the permeability of the porous material, the surface area that is perpendicular to the flow direction, the thickness of the porous material and the viscosity of the flowing fluid. The relation between these variables has been determined experimentally by Darcy [10]:

$$\dot{q} = \frac{\kappa_p A_p (p_1 - p_2)}{\mu L} \tag{B.2}$$

where μ the viscosity of the fluid, L the thickness of the porous material, κ_p the permeability of the porous material and A_p the surface area. Writing this in the same form as in equation B.1:

$$R_p = \frac{\mu l}{\kappa_p A} \tag{B.3}$$

where R_p is the resistance for a porous restriction in [Pa s/m^3] or [kg/m^4 s].

B.2. Orifice restriction

The next restriction option is an orifice restriction, this is basically a small hole with diameter d in a thin plate, where $l \approx d$. The relation of an incompressible flow to the pressure difference has been experimentally determined [15]:

$$\dot{q} = C_d A \sqrt{\frac{2(p_1 - p_2)}{\rho}} \qquad A = \frac{\pi}{4} d^2 \tag{B.4}$$

where ρ is the density of the fluid flowing through the orifice and C_d is a discharge coefficient. This coefficient is a measure between the actual flow velocity and the theoretically maximum Bernoulli flow velocity. The value of the restriction coefficient is between 0 and 1 and is highly dependent on geometry and Reynolds number [38], however normally 0.61 is taken [7]. The restrictive value of an orifice (R_o) in the familiar form can be stated as follows. Note that the restriction of an orifice is dependent on the air flow, which is in contrast with a porous restriction.

$$R_o = \frac{8\rho}{C_d^2 \pi^2 d^4} \dot{q} \tag{B.5}$$

As stated, the formulas above are valid with the assumption of incompressibility. This normally means a low pressure difference or the usage of liquids. In an externally pressurized air bearing the pressure differences are significant and can therefore not be neglected. For an orifice restrictor the relation of a compressible flow to the pressure difference should therefore be stated as [4]:

$$\dot{q} = C_d A p_1 \sqrt{\frac{k}{k-1}\left(\left(\frac{p_2}{p_1}\right)^{2/k} - \left(\frac{p_2}{p_1}\right)^{(k+1)/k}\right)\frac{2}{R_s T}} \qquad \text{if} \quad \frac{p_2}{p_1} \geq 0.528 \tag{B.6}$$

$$\dot{q} = C_d A p_1 \sqrt{\left(\frac{2}{k+1}\right)^{2/(k-1)}\left(\frac{k}{k+1}\right)\frac{2}{R_s T}} \qquad \text{if} \quad \frac{p_2}{p_1} < 0.528 \tag{B.7}$$

where $k = 1.4$ is the specific heat ratio of air at constant pressure and volume, $R_s = 287.1\,\mathrm{J/(kgK)}$ is the air constant and T the absolute temperature upstream of the orifice. The pressure ratio p_2/p_1 determines which formula should be used. The reason for this is that flow velocities reach the speed of sound for pressure difference below the given margin. Velocities cannot be further increased than the speed of sound, meaning that the flow will become choked and independent of the pressure downstream. One understands that it is impossible to rewrite these formulas in the familiar form, where the restriction is related to geometric variables (and the air flow) only.

B.3. Capillary restriction

The last common restrictor is a capillary restriction, which is basically a pipe with a small diameter d and a length l in another bigger pipe, see figure B.2. Depending on assumptions and working conditions, different theories can be used to calculate the restrictive value of capillary restrictions. We will start with the assumption of laminar flow.

B.3.1. Laminar flow

Derived from the Hagen-Poiseuille law, a viscous fluid flow (Re < 1000 and $l/d > 20$) relates to the pressure difference as follows [40]:

$$\dot{q} = \frac{\pi d^4}{128 \mu l}(p_1 - p_2) \tag{B.8}$$

where μ is the dynamic viscosity in [kg/ms], this means that the restriction can be formulated as follows:

$$R = \frac{128 \mu l}{\pi d^4} \tag{B.9}$$

Capillary restrictors are used to promote a steady laminar flow into an air bearing, which is considered to give the best results. Although capillary restrictions have been used, both Vuong [39] and Hoogeboom [29] came to the conclusion that the created flow was not laminar but turbulent. The reason for this was a Reynolds number transcending the valid region of the formulas above. This meant that the restrictive value was depending on the pressure difference, contrary to what one would believe based on equation B.9.

B.3.2. Adiabatic Fanno flow

For higher Reynolds numbers a Mooody type friction flow can be considered, which takes into account the compressibility and friction of the viscous fluid along the pipe surface. This type of flow is often called a Fanno flow, since it was studied by Fanno for the first time. The adiabatic assumption is normally taken for high velocity flows in a short duct. A full overview including derivation of an adiabatic Fanno flow is presented in [41, Ch. 9.7], a method to use the theory is discussed here. The conservation laws for continuity, momentum and energy can be solved using the perfect-gas law as well as the relation between wall shear and the local Darcy friction factor (Moody chart). One of the results is the following relation:

$$\frac{p}{p^*} = \frac{1}{\mathrm{Ma}} \sqrt{\frac{k+1}{2+(k-1)\mathrm{Ma}^2}} \tag{B.10}$$

With this formula one calculates the ratio between the inlet pressure p and outlet pressure p^* for a certain duct based on the inlet Mach number (Ma), given that the duct has exactly the length that is required to develop a sonic flow. Another relation, derived from the Fanno theory:

$$\frac{\bar{f} l^*}{d} = \frac{1-\mathrm{Ma}^2}{k\mathrm{Ma}^2} + \frac{k+1}{2k} \ln \frac{(k+1)\mathrm{Ma}^2}{2+(k-1)\mathrm{Ma}^2} \tag{B.11}$$

where $\bar{f}$ is the average friction factor for the pipe form $x = 0$ to $x = l^*$ derived from the Moody chart based on the Reynolds number and the relative pipe roughness. l^* is exactly the length that is required to develop the flow such that the Mach number equals unity at the outlet. When designing restrictors, one normally knows the required pressure difference $(p_1 - p_2)$ and the mass flow $\dot{m}$. Using the ideal gas law, one can find the inlet density, which means that the flow velocity at the inlet of the capillary restriction can be found using:

$$v = \frac{\dot{q}}{A} = \frac{4\dot{m}}{\rho \pi d^2} \tag{B.12}$$

Using the inlet density of the gas, as well as the bulk modulus $K_c = k * p$ one finds the speed of sound, using $c = \sqrt{K_c/\rho}$. The Mach number is defined as the ratio of velocity over the speed of sound Ma= v/c. This means that if $\bar{f}$ and p_1 are known, p^* and l^* can be calculated using equation B.10 and B.11. The specific heat ratio is commonly taken as 1.4. Using the obtained p^* and required p_2, the theoretical Mach number at the outlet Ma_2 can be derived using equation B.10 again. Reasoning further, a second l^* can be calculated using equation B.11. Subtracting the latter l^* from the one found earlier, one obtains the required length for the desired pressure difference and mass flow. Some precautions should be taken into account while using this theory, since it does not hold for flows that develop a flow equal to the speed of sound. In the case of air bearings, a subsonic flow is promoted in the capillary tubes and therefore care should be taken not to exceed a Mach number of 1.0. Ultimately, at a Mach number equal to unity, while starting with a subsonic flow, the flow will become choked. In practice this means that the maximum mass flow will be decreased resulting in a lower mass flow than expected based on the pressure difference.

Based on the Fanno flow theory Turton [35] derived new relations that relate the up and downstream characteristics. The results that can be obtained with these relations are similar as the ones presented above, however these are less cumbersome in use since different variables are chosen for elimination.

$$\frac{fl}{d} = \frac{k-1}{2k}\left(\frac{p_1^2T_2^2 - p_2^2T_1^2}{T_2 - T_1}\right)\left(\frac{1}{P_1^2T_2} - \frac{1}{P_2^2T_1}\right) - \frac{k+1}{k}\ln\left(\frac{P_1T_2}{P_2T_1}\right) \tag{B.13}$$

$$\dot{m} = A\sqrt{\frac{2kMp_1^2p_2^2}{(k-1)R_g}\left(\frac{T_2 - T_1}{T_1^2P_2^2 - T_2^2P_1^2}\right)} \tag{B.14}$$

where M is the molar mass of the fluid used, here 28.97×10^{-3} kg/mol for air and R_g is the gas constant, which is 8.314 J/K/mol. Equation B.13 can be used to determine the outlet temperature T_2 if the pipe characteristics and in and outlet pressures are known. Afterwards equation B.14 can be used to determine the mass flow. One understands that these steps are less cumbersome since the Mach number does not need to be calculated any more, moreover the length of the pipe can be used instead of the detour via l^*. However precautions should still be taken with respect to choked flow, which means that the Mach number should still be calculated in some situations.

B.3.3. Isothermal Fanno flow

In this section an isothermal flow with friction will be investigated. Although an adiabatic assumption makes more sense for short ducts with high velocity flow, mostly found in air bearings, the isothermal situation is shown for its ease in calculation. The difference with the adiabatic Fanno flow is that the continuity equation for energy is replaced by the simple relation $dT = 0$. All variables are eliminated using the Mach number again. However, due to the constant temperature over de pipe a direct relation between the known pressures and mass flow can be derived, which is done in [41, Ch. 9.7]. The result is an useful relation between mass flow and in and outlet pressures.

$$\left(\frac{\dot{m}}{A}\right)^2 = \frac{p_1^2 - p_2^2}{R_sT(\bar{f}l/d) + 2\ln(p_1/p_2)} \tag{B.15}$$

B.3.4. Comparison theories

In this section the different theories will be compared for a case study. In this case study a capillary restrictor is required that restricts an air flow ($\dot{m} = 2.75 \times 10^{-5}$ kg/s) from $p_1 = 4 \times 10^5$ Pa to $p_2 = 3 \times 10^5$ Pa. This corresponds to a restrictor with a value of 1.5×10^{10} Pa $*$ s/m^3. Figure B.3 shows the required relation between the diameter and length of the restrictor. The friction factor is taken as 0.04 for the whole length of the duct and all diameters. Theoretically this is not correct since the pressure changes along the duct, which means the density changes and so does the velocity and the corresponding Reynolds number, which influences the friction factor. However the changes in Reynolds number are limited and normally no attempt is taken to compensate and an average friction factor is assumed along the duct [41, p.659]. Also the diameter change leads to small changes in friction factor and therefore a constant friction factor is used. The value 0.04 is a results of a relative roughness factor of ($\epsilon/d = 0.0015/0.25 = 0.006$) and a Reynolds number ranging between $4 * 10^4$ and $10 * 10^4$.

It is clear that the laminar assumption shows significantly different results compared to the Fanno flow, which makes perfect sense since the restrictor is operated with Reynolds numbers exceeding the limitations of the laminar flow assumption. The isothermal and adiabatic flow however show a very comparable relation between the required diameter and length. Note the dashed line around 0.164 mm as well, this line indicates the diameter for which the outlet flow of the adiabatic pipe equals unity. This means that the results on the left side of this line are not relevant for the adiabatic calculation, since this involves a choked flow. Moreover, because the isothermal and adiabatic lines are comparable the dashed line can also be taken as a good approximation of the lower limit for the isothermal calculation.

B.4. Comparison

The potential of the use of porous restrictors for air bearings has been shown [11, 36]. Advantages could be a higher out of plane stiffness as well as a smooth pressure distribution. Moreover, they are quite tolerant to damage and relatively insensitive to clogging. A major downside however is the difficulty to obtain the

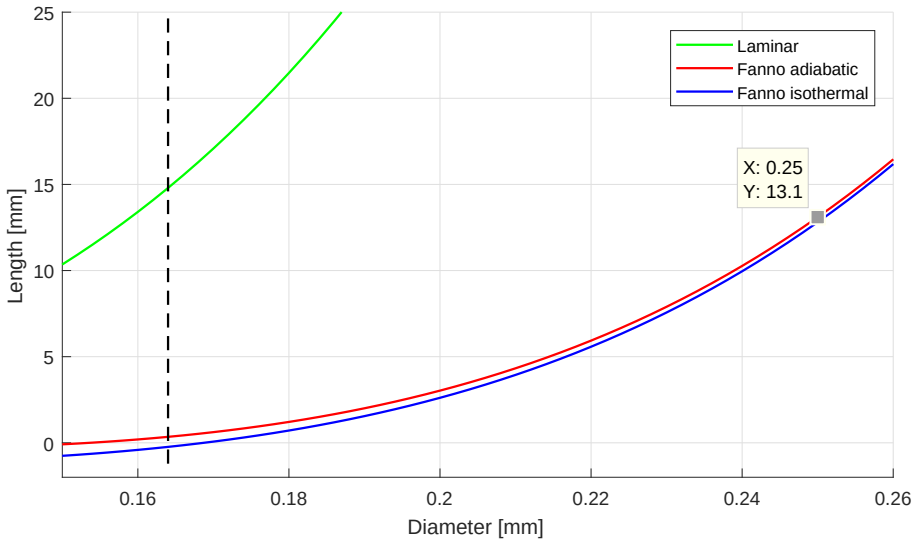

Figure B.3: Comparison of the diameter and length necessary for a restrictive value of 1.5×10^{10} Pa $*$ s/m^3 for different theories. Laminar, adiabatic and isothermal Fanno flow are plotted.

correct material in terms of permeability and evenness throughout the material. Moreover, since a single point restriction is required, there is no simple way to implement them in the current design. For this reason, a porous restriction is not considered as a viable option.

Orifice restrictions have shown their potential in the high tech industry [11] as well. Computation techniques made implementation easier and engineers came up with many configurations including multiple orifices and the usage of grooves. However controlling the exact length of the hole and maintaining the ideal bevelling is challenging and condemned to fail, while crucial for an as-designed resistance, [38] states that a sharp edge orifice can have half the flow resistance compared to a bevelled orifice. Moreover slight variation in diameter results in large flow deviations as well, see equation B.4.

Contrarily, capillary restrictors turned out to be rather easy to implement [29, 39]. Moreover, since the length of the tubes can easily be modified the resistance can be tuned rather simple as well. For these reasons, a capillary restriction is chosen for implementation. The adiabatic Fanno flow theory will be used to dimension the restriction.

C

Restriction measurements

In this appendix the restriction measurement will be discussed and explained in more detail. The Labview program written to perform the restriction measurements will be shown and briefly explained, moreover an irregularity of the measurement will be discussed. The Labview user interface is shown in figure C.1. A moving graph showing the pressure level over time will be shown in the black box during measurement. The name of the data output file can be given in the top left. The time step between two measurements can also be defined. To stop the measurement the big button with "STOP" can be used.

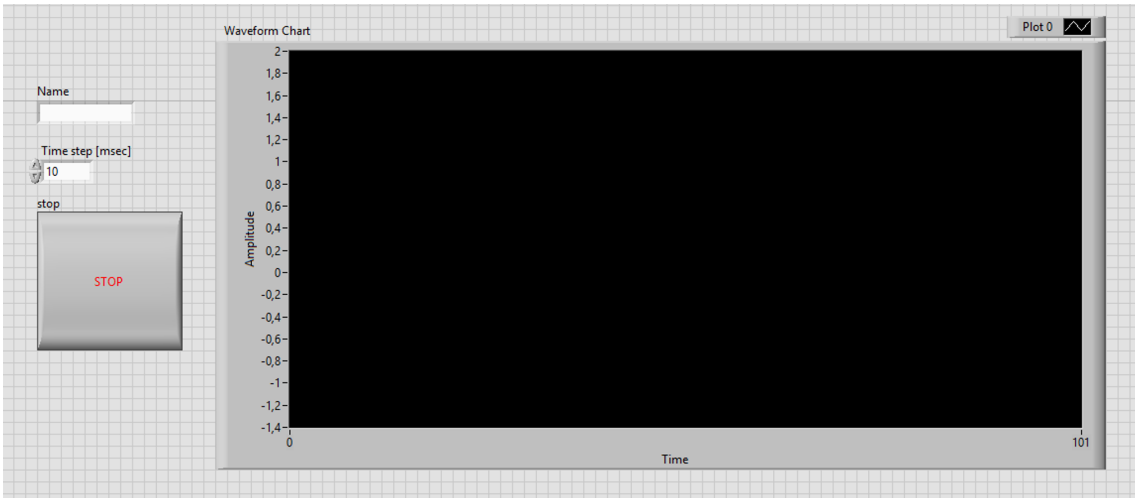

Figure C.1: LabView user interface

The Labview block diagram defining the output of the program is shown in figure C.2. In the top left corner in pink the name of the output program is defined including time and date stamp. Below that the input signal from a 16-bit multifunctional I/O Device is processed, a NI USB-6211 from National Instruments is used. In the upper right corner (orange) the incoming signal is transferred to a pressure level in kilopascal using the conversion rates given by the sensor manufacturer. As stated in the report a NXP 5700DP differential pressure sensor is used. In the lower right corner the data obtained is written to the file defined. All the boxes and clocks in the block diagram ensure that all steps are done with the correct timing and sequence.

After the Labview setup has been explained an irregularity in the measurements will be discussed. The irregularity is actually not very irregular since it has been noted at most measurements, however it is irregular since it has not been explained yet. After the pressure has been measured over time, the mass flow versus pressure can be calculated and is given in figure C.3. The calculation has been explained in chapter 4, however the equation will be given again:

$$\dot{m} = \frac{\partial p}{\partial t} \frac{V}{R_s T} \tag{C.1}$$

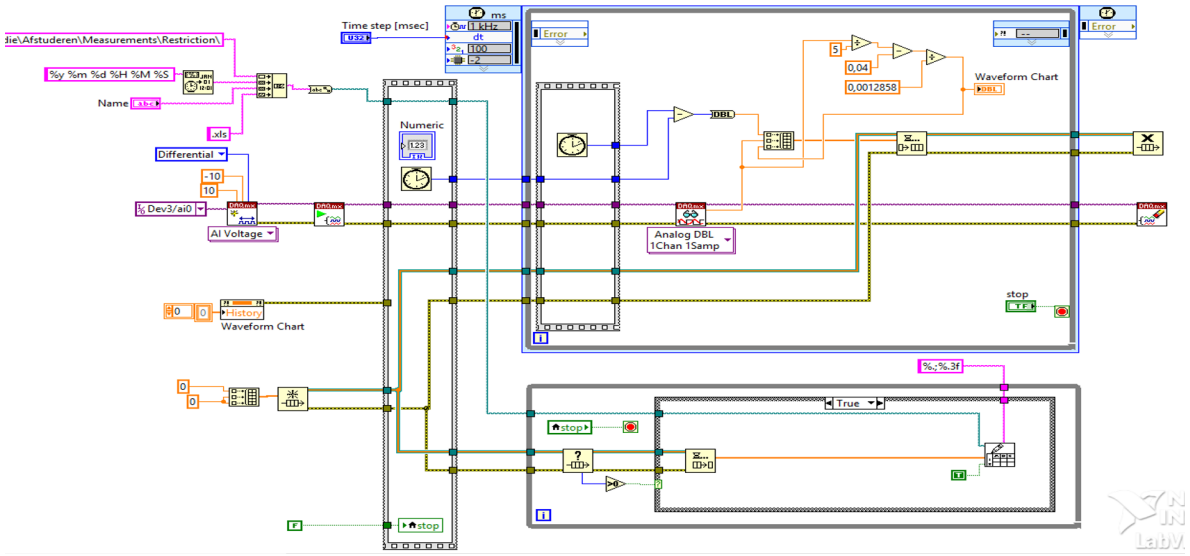

Figure C.2: LabView block diagram

In figure C.3 focus on the light blue lines which indicate the mass flow over pressure difference for a normal measurement described in chapter 4. All these light blue measurements have been done with the same procedure and same restriction, however it can be seen that the mass flow becomes less predictable at higher pressure levels and an inexplicable high mass flow is present, which is called the measurement 'flag'. One would expect a line that increases steadily for pressure level above the 2.5 bar, however a flag is present. The equation to calculate the mass flows present is based on the assumption of constant pressure in the tank and restriction. The assumption could be incorrect and therefore some extra measurements were done to verify the assumption. Figure C.4 shows the measurement setup, the parts in the red box are added in comparison with the measurement setup described in the report, see figure 4.6. First of all the influence of the restrictors temperature was investigated. This was done by opening valve 1 and 2 in figure C.4, which meant air was flowing from the wall supply through the tank and restrictor to the ambient pressure. After some time valve 1 was closed and the measurement was started simultaneously. This did not change the results and a similar flag was present in the obtained results. Therefore is has been concluded that the temperature of the inlet restriction does not play a role in the origin of the flag.

A second measurement procedure was done with the auxiliary restriction 2 to see whether this could change the flag. The tank was filled with a pressure difference higher than 5 bar. Afterwards valve 3 was opened and air did flow through the restriction 2, which was significantly larger than restriction 1. Once 4 bar pressure difference was reached, valve 3 was closed, valve 2 opened and the measurement with Labview was started. This procedure gave the light blue line in figure C.3. As can be seen the obtained data is less widely spread and on average lower for the higher pressure difference. Clearly the followed procedure gave different results. The hypothesis is that the air temperature in the tank plays a role.

More measurements where done to verify this hypotheses. Some normal measurements were done starting at a lower pressure level, this gave the pink lines, again a chaotic flag is present. Afterwards the tank was filled with higher pressure again and the auxiliary restriction was used to lower the air pressure in the tank to the same level as the starting point for the normal measurements. A quick switch was made between valve 2 and 3 before the data acquisition started with Labview. Again a less chaotic flag was present and a lower average mass flow for the higher pressure levels was seen. A last measurement was done with air flowing from a high pressure level through the restriction 1. After a pressure around 2.25 bar was reached valve 2 was closed and opened quickly, in the meantime the measurement with Labview was started. Again this gave a lower average mass flow for the higher pressure levels. The difference between the last two procedures is that restriction 1 is much smaller than restriction 2, meaning that a higher mass flow is present.

This leads to a higher and more comparable mass flow with the mass flows during the measurement. It can be seen that all the measurement do show a very similar behaviour for pressure levels below 1.25 bar, the author thinks that the reason for this is that the air temperature in the tank stabilizes after some time due to interaction of the tank with the environment, heat subtracted from the environment and the adiabatic

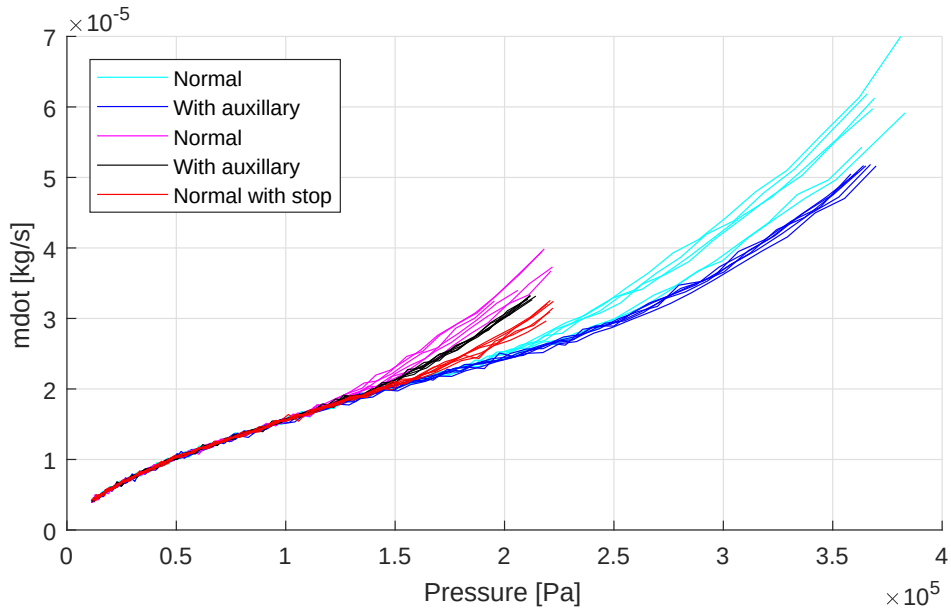

Figure C.3: Mass flows for different measurement procedures for the same restriction

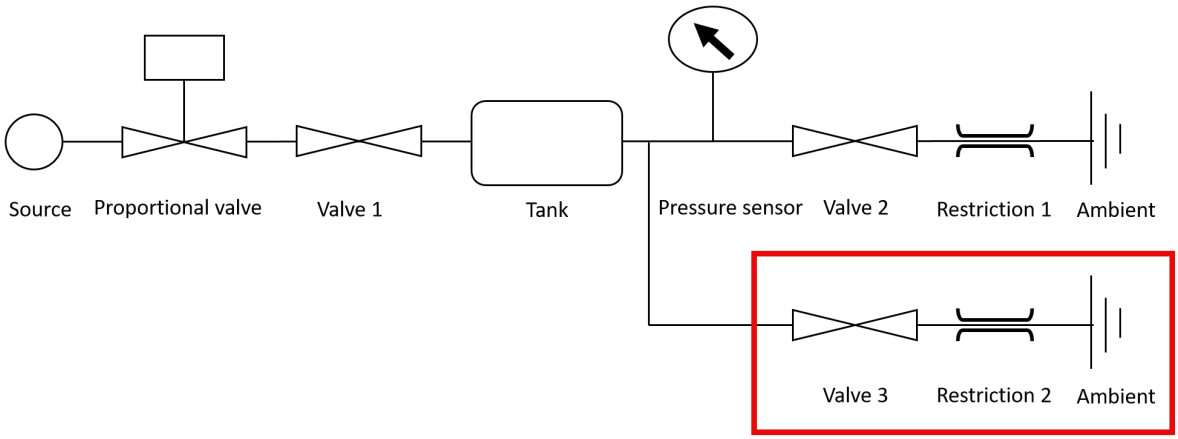

Figure C.4: Schematic measurement setup with an auxiliary restriction compared to the measurement described in chapter 4

expansion in the tank find an equilibrium. Initially this balance has not been obtained and therefore a flag is present since the temperature in the tank is still subjected to temperature changes. Reasoning further this means that the measurements which have been described in the report to obtain the friction factor did yield incorrect results, since an incorrect assumption for the temperature has been used. Unfortunately, no further research into this topic has been done due to time limitations. To improve correctness of the mass flow calculations the author recommends to measure the air temperature in the tank simultaneously with the pressure measurement which is already done at the moment.

D

Pin manufacturing

As explained in chapter 4 pins have been fastened into the bottom plate with Loctite 246 and afterwards the surfaces have been machined to decent flatness and roughness. Coming to this solution required several steps which will be explained here focussing on what can be learned from these steps.

D.1. Air tightness

A first attempt to create an air tight connection between pins and bottom plate, O-rings were used. Actuator pins were manufactured according to figure D.1. An O-ring with a larger diameter than the groove depth was used. Afterwards the pins were pushed in the correct position, no glue or other connection was used. The friction between O-ring, pin and hole was the only fixing. This resulted in an air tight solution, however the connection of a pressure source resulted in the displacement of the pins and ultimately they were pushed out of the bottom plate due to the pressure applied.

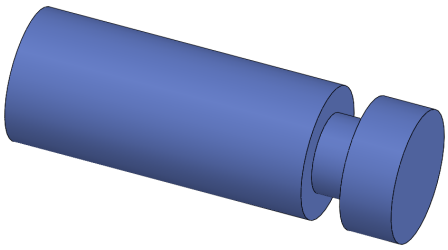

Figure D.1: Schematic view of actuator pin with notch for O-rings.

A second attempt was done using O-rings and a glue based on cyanoacrylate to ensure the fixed connection between bottom plate and actuator pin. A cyanoacrylate glue has been used since it is known for its low viscosity and creeping in small gaps before drying. Therefore the pins were pushed in correct position and glue was deposited at the interfaces after positioning. Although this solution was able to withstand higher pressure than a solution without glue, it resulted again in displacements of the actuator pins after increasing the pressure level.

A third attempt was done using Loctite 246 which is a specialized liquid fastener that cures in the absence of air while being in a confined space between two metal surfaces. Loctite 246 is also known for its air tight connections and has therefore been applied without O-ring. For optimal fastening the pin and corresponding hole surfaces have been slightly roughened using some fine sand paper. This procedure has been satisfying for the contactless stage, which has been used up to a supply pressure of 4 bar without failure.

D.2. Flatness

As explained in chapter 4 all pins have been machined flat after fixing with Loctite 246 This required several iterations as well. An important lesson learned is that the obtained flatness differs per machine and requires some trial and error for that reason. In the end the Aciera F3 has been used since the results obtained were

fine and could be reproduced. Next to using the best machine a procedure was found which turned out to be beneficial for the flatness. A crucial part of this procedure was to stop the milling operation when the front side of the face mill had machined all surfaces, meaning that the back side of the face mill was not allowed to get into contact with the surfaces, see figure D.2. The reason for this is that it turned out that the mill removed material on two sides; at the front side, the point were initial contact is made, but also at the opposite side of the mill, which is called the back side for simplification. This last contact left scratches on the surface probably due to instability of the machine and the difference between conventional and climb milling. For these reasons the flatting operation was stopped with the mill completely covering all pins, meaning that the back side of the mill never came in contact with the pins and no scratches were left on the surface, see figure D.2.

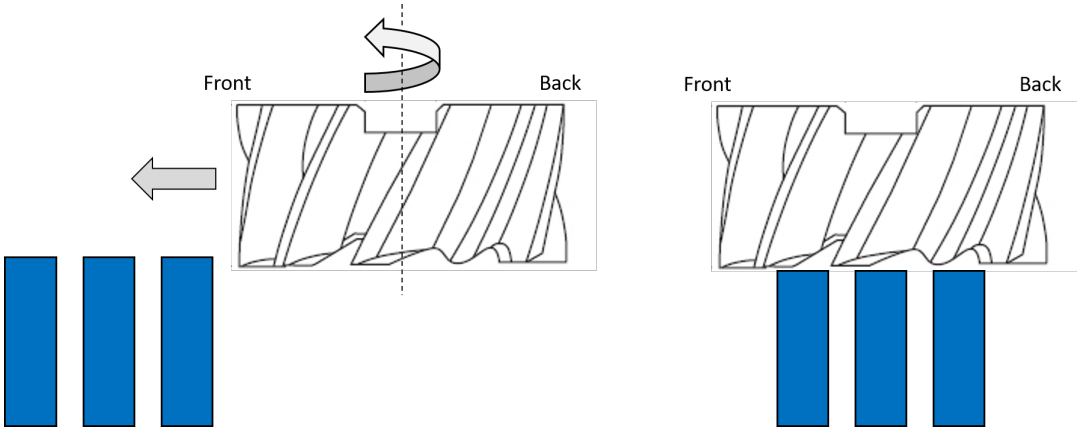

Figure D.2: At the left the start of the milling operation is visualised, at the right side the position of the face mill with respect to the blue pins has been shown were the machining operation should be stopped.

Another complication during the milling operation showed up, it involved the milling of the already installed inlet restrictions. It turned out that although all pin surfaces were flat with a maximum peak to peak distance of 8 μm the inlet restrictions did protrude above the surface after machining. This can be explained with the fact that the inlet restriction tubes were made from a different material than the aluminium pins, resulting in a different material removal. The protruding inlet restrictions could not be allowed due to the limited fly heights, therefore a drill operation over minimal depth has been used to remove the protruding parts. This had two implications, first of all the inlet restriction would be lower since the capillary tube was shortened, which results in a reduction of the out of plane stiffness of the stage. The second implication is that a pocket was introduced in the middle of the actuator, this pocket increases the stiffness of the actuator significantly and therefore the reduced length of the tubes is acceptable. A downside of the pocket is a smaller actuator area, which reduces the maximum actuator force. For this reason the author advises future manufactures of a contactless outlet variation stage to incorporate the restrictions at the very end of the production process. This means that the manufacturer is in full control of the length of the capillary restriction as well as the presence and depth of a possible pocket.

E

Actuation force

In this appendix the actuation force necessary for actuation will be discussed. The actuation force should not be confused with the actuator force, which is the force generated by the actuator. The actuation force is a determined by stiffness induced by air flow and pressure as well as mechanical connections between top and bottom plate.

E.1. Air

Air flow and pressure create a viscous force and a pressure force in the gap. The viscous force is generally in the order of millinewtons, while the pressure force is generally in the order of tenths of Newtons per actuator pin, therefore the focus will be placed on the force originating from the pressure differences in the gap. The pressure difference in the gap during actuation can be seen in figure 3.4b, a non symmetric pressure distribution is present. During actuation the pressure will be higher on the side where the gap is smaller, so the net force from this pressure distribution pushes the actuator back to the centre of the hole. A larger actuation ratio does generally mean a larger pressure difference and thus also a larger force required to actuate. These pressure differences are a crucial part of the outlet restriction concept and have to be accepted. The actuation force can be influenced by changing the pressure differences or the area. Lower pressure differences result in a lower actuator force and is therefore unwanted. The area however can be changed by changing the outlet length. The actuation force at an actuation ratio of 0.8 for a single pin hole combination has been plotted for different actuation lengths in figure E.1. At this actuation ratio the maximum actuation force has been found. It can be seen that an optimum is present, which is counter intuitive since a longer length indicates a larger area and thus a larger force and therefore one could expect a larger force.

The reason for the optimum can be found in figure E.2, where the pressure at the inlet of the outlet restriction is shown. The pressure is plotted against the angle of the respective location of the outlet seen from the centre of the actuator. It is clear that for a longer length the difference between the two maxima reduces.

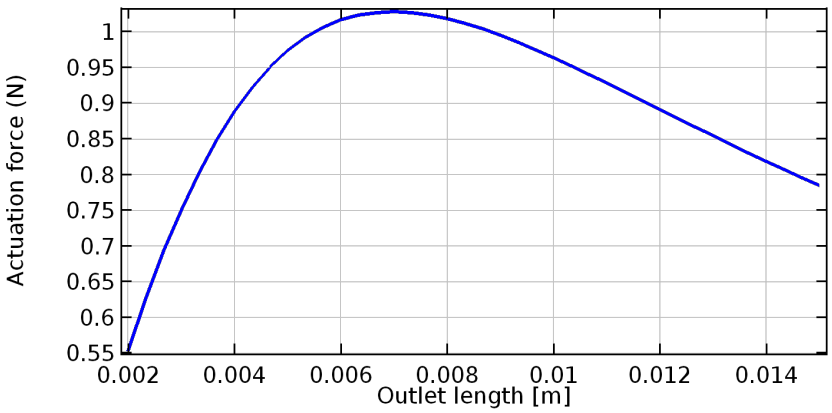

Figure E.1: Actuation force [N] per actuator for different outlet lengths

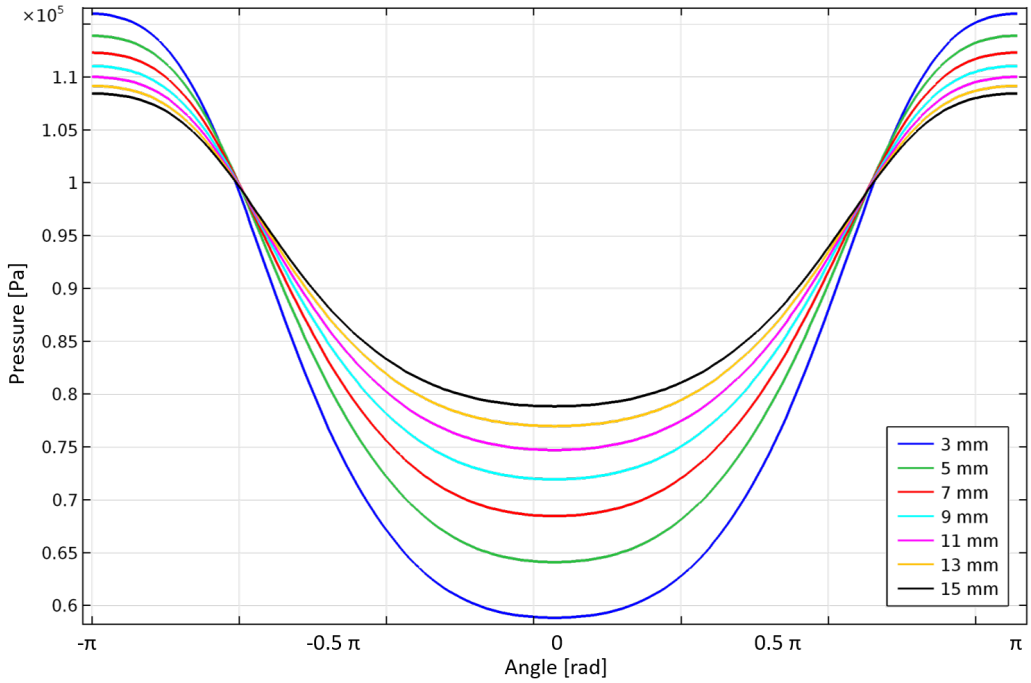

Figure E.2: linePressureActuationForce [N]

A lower pressure difference results in a lower actuation force, which has been discussed before. The reason why the pressure difference reduce can be explained with the fact that the ratio between outlet resistance and surface resistance on the actuator increases. In other words, the increasing length of the outlet resistance increases its restrictive value, the surface restriction remains equal and therefore a larger part of the pressure potential between pressure and vacuum source will be covered by the outlet restriction. This means that all pressure levels at the start of the outlet will develop towards p_+, the pressure at the inlet, for larger outlet lengths.

E.2. Mechanical

The top and bottom plate have been connected with three wire flexures. A displacement of the top plate relative to the bottom plate requires bending of the wire flexures. The wire flexures do have some stiffness which is depending on the material, diameter and length of the wire flexures. The stiffness of a clamped beam with loading at the end can be derived.

$$k = \frac{3EI}{L^3} \tag{E.1}$$

with E the materials Young's Modulus (180 Gpa for spring steel), I the second moment of inertia and L the length of the beam, see figure E.3. Adding two of those beams gives the situation of the wire flexures, the equation for stiffness per wire flexure becomes as follows.

$$k = \frac{12EI}{L^3} \tag{E.2}$$

E.3. Outlet variation stage

Using the theory and knowledge presented above the total actuation force for the created outlet variation stage can be calculated. The mechanical stiffness for a wire flexure installed is 1.1×10^5 N/m. The maximum counter force generated by the contactless stage in terms of air pressure is around 4.4 N at an actuation ratio around 0.8. In figure E.4 all forces have been plotted as well as the total force required, which is maximum 20 N. Assuming a constant stiffness from zero actuation to maximum actuation this adds up to 400 kN/m for the total actuator. Dividing by the surface area of the top plate this gives an stiffness per surface area

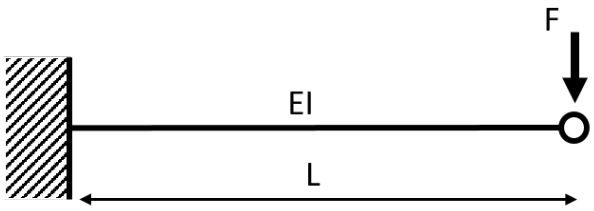

Figure E.3: Clamped beam

around 40 MN/m^3. To put this in perspective, the flowerbed has a theoretical stiffness per surface area around 6 MN/m^3 [17, p.14]. This means that a high stiffness is present in the current concept, which should and can be lowered by increasing the number of actuators, since at the moment most of the surface area of the top plate is subjected to the maximum vacuum pressure. An increasing number of actuators means a lower available surface area, which means that the wire flexures can be made thinner. Moreover the wire flexures have been over dimensioned for the current generation, which means that the length diameter ratio could be optimised.

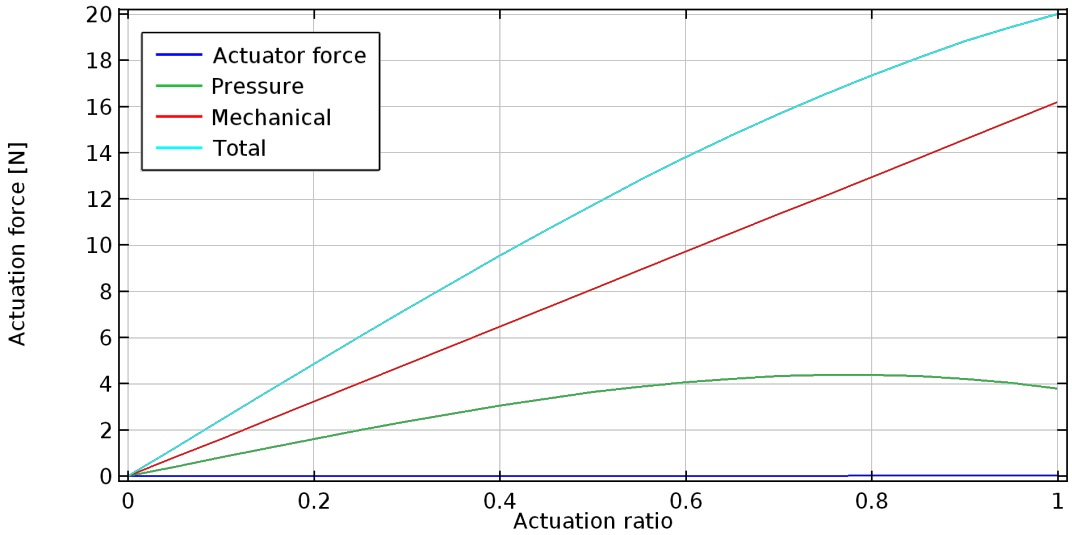

Figure E.4: Clamped beam

F

Numerical model

In this chapter the numerical model, created in COMSOL will be explained. Although many models have been created during this research, the final model is chosen as example in this appendix. This appendix is written to guide readers who want to build their own model, however do realise this is not a manual to COMSOL. The structure of a COMSOL model can be seen in the "Model Builder", see figure F.1. Generally speaking, building a model is done following the steps in the model builder starting at the top. One starts defining **parameters** in the "Parameters" section, parameters often define the actuator geometry.

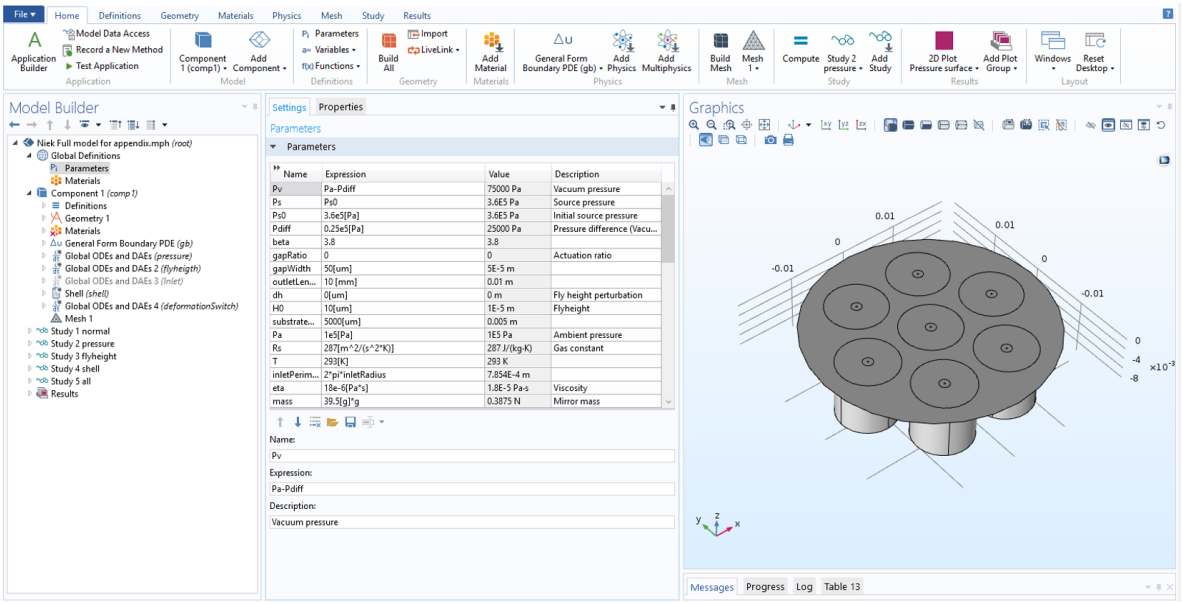

Figure F.1: General overview of a COMSOL model

Afterwards the **geometry** was created based on the parameters just defined. Since the Reynolds equation is based on the assumption of laminar flow it can be solved two-dimensionally. This means that, the actuator in figure F.1 is build up from multiple dimensional surfaces where variables, such as fly height, have been defined at the surface. A predefined shape, in this case a circle, has been used. However, the hexagon in figure 3.2 has been created using a "Polygon". Moreover another interesting feature is the "Extrude" function, which made it possible to give the outlet restriction a length a model it as a thin film. Make sure to check the box "Unite with input objects". Basically multiple two-dimensional models have been coupled in this way, making a three-dimensional figure, however the calculation are still done two-dimensionally. Once the geometry has been defined a **mesh** can be defined, a "Physics-controlled mesh" could be chosen or an "User-controlled mesh", in this research the first option has been chosen. "Element size" has to be defined afterwards, usually "Finer" has been chosen, since more precise meshed did yield the same results.

The next step is to define general and local **variables**, the difference between variables and parameters is that variables are not necessarily predefined and can get a value based on the result of a computation. In figure F.2 an example can be seen of locally defined variables. The fly height in the pockets should be different than the fly height on the dams. Moreover a dependency on the "flyheightVariable" is seen. This variable can be changed by COMSOL to satisfy the no load condition. The implementation of this condition will be explained later. Moreover the shear stresses are also calculated on the surface. Using an integration, in this case "intop1", over the whole surface the force can be derived from the shear stresses.

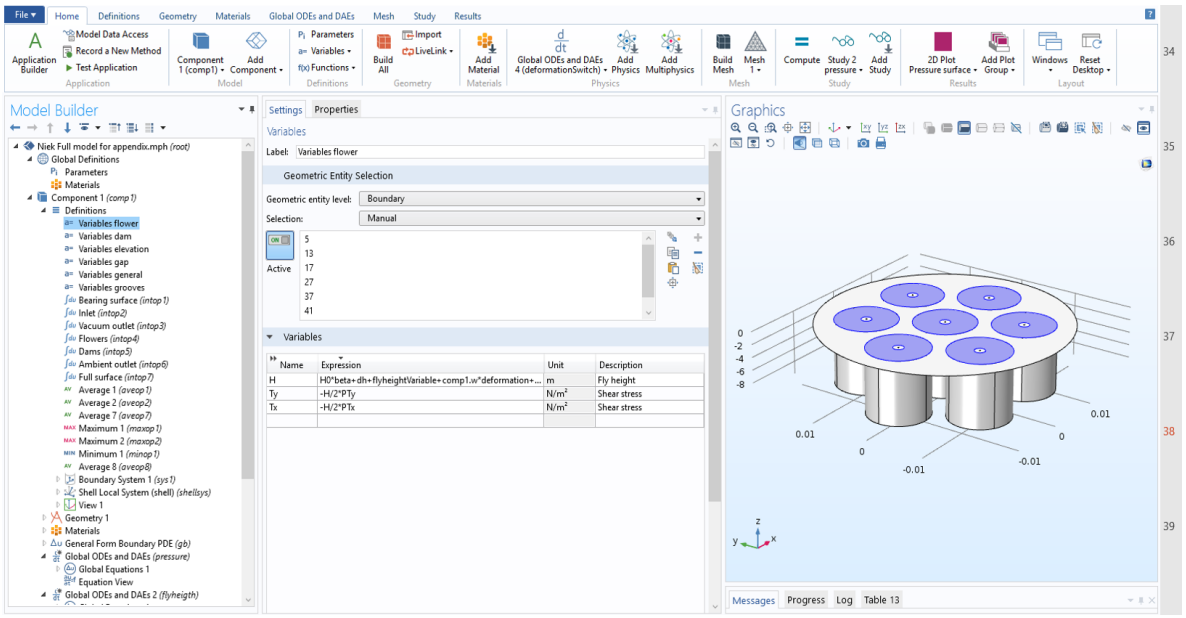

Figure F.2: Defining local variables in COMSOL

After the geometry, parameters and variables one usually starts defining the **physics** involved. COMSOL has many pre defined physics also a standard packages for thin film flow studies is implemented, however it has been chosen to introduce the Reynolds equation in a "General Form Boundary PDE". The reason for this is that the package has extra options which are unnecessary and by defining the differential equation in its mathematical form gives a better understanding of the model. In figure F.3 it can be seen how the Reynolds equation was defined in the model. As can be seen it has been defined in all three Cartesian directions. The "Source term" f, "Damping or Mass Coefficient" d_a and the "Mass Coefficient" e_a have all been defined as zero. With a "Dirichlet Boundary Condition" ambient pressure was defined at the outer ring of the elevated dams the vacuum pressure was defined at all seven outlets. At the seven "Flux/Source" tabs the mass flow at every inlet was prescribed based on the source pressure and the pressure at the surface. A curve fitted through the restriction measurements in figure 4.8 was used.

As can be seen in figure F.3 four more physics have been defined. Three "Global ODEs and DAEs" have been defined in mathematical physics tabs. In these tabs an equation can be stated that should be equal to zero, COMSOL will try to find a solution that satisfies this condition while varying a predefined parameter. In the first Global ODEs and DAEs, named "pressure" the following equation will be solved:

$$W_m - F_z = 0 \tag{F.1}$$

The parameter allowed to obtain this equilibrium it the pressure source. In other words, the weight of the mirror W_m will be made equal to the load capacity F_z of the actuator by varying the pressure source. A higher pressure source will results in a higher average pressure and thus a higher load distribution. In the second Global ODEs and DAEs "flyheight" the same equation is solved, however COMSOL is now allowed to vary the fly height by varying the "flyheightVariable", which has also be seen in figure F.2. A higher fly height means a lower surface restriction, which results in a lower average pressure assuming the inlet resistance is larger than the outlet resistance. Finding an equilibrium between the mirror weight and the load capacity should only be done with one of the methods described above. In the report, this is distinguished with "solving for pressure" or "solving for fly height". The next physics that is defined is the predefined "Shell" package. In this

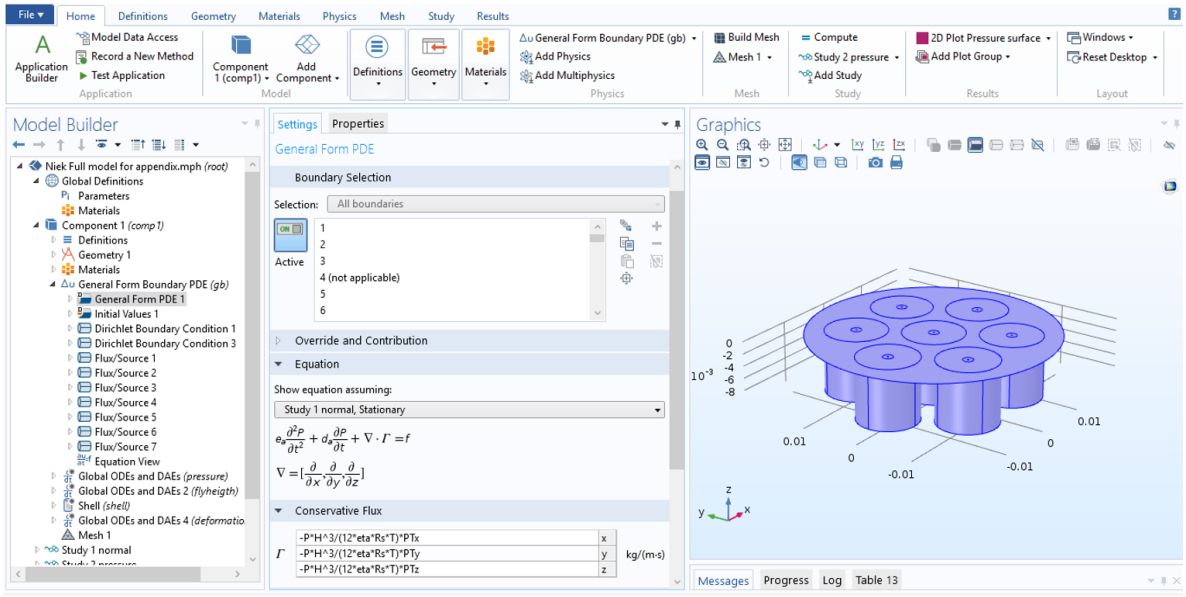

Figure F.3: Compressible Reynolds equation in COMSOL

intuitive package a material with certain thickness is prescribed. The pressure distribution is used as a "Face load", using six "Global constraints" the shell is fixed in space. In those constraints the displacement and rotational axes of the mirror will be constrained by setting "intop(u)", "intop(v)", "intop(w)", "intop(arx)", "intop(ary)" and "intop(arz)" equal to zero. The last Global ODEs and DAEs "deformationSwitch" couples the deformation of the shell to a change of fly height. The equation that is solved is simply $S_d - 1 = 0$, the obvious results changes the deformation switch parameter S_d from zero to unity. This ensures that the calculated deformations, "comp1.w" in figure F.2, are coupled to the fly height. Defining this separately means that first the deformation can be calculated based on a certain pressure distribution, coupling afterwards makes convergence of the model easier since an initial condition is defined by the uncoupled solution. Directly solving for a coupled end results is more complex for the solver and can results in a non converging model.

Defining a **study** is done in the "Study" section of the model builder. Per study different study steps can be defined, depending on the required outcome. The example that will be discussed is "Study 5 all", which is the most elaborate study since in this study all physics will be coupled. As can be seen in figure F.4 four stationary steps have been defined. The physics that have to be solved for can be defined per step using the check boxes in the "Physics interface". The different steps will be coupled in the "Values of Dependent Variables" tab such that the initial values of the variables is equal to the solutions just found in the previous step. In the first step, only the Reynolds equation will be solved, in the second step COMSOL solves also for the fly height. In figure F.4 it can be seen that in the third step the deformation of the thin film is added, in the final step the deformation switch is also checked and thus solved for. Note that the second physics will not be used, since in this case the model is solved for fly height, which means a constant pressure source is prescribed.

Another interesting feature, which has been used frequently, in the study section is the possibility to perform a "Parametric sweep" or an "Optimization", which are methods to verify the influence of certain parameters or find an optimum. Next to a parametric sweep also a "study extension" can be used, this options is basically the same as a parametric sweep, however the initial situation for a calculation is chosen to be equal to the solution that has been found for the previous calculation. This means that it is generally faster, however it cannot be applied on parameters defining the geometry, since the mesh will change and COMSOL does not couple information from two different meshes in a study extension. Lastly, the "Solver Configurations" can be changed, allowed "Relative tolerance" could be controlled, moreover in the "Method and Termination" tab, the stopping criteria can be changed as well as which Non-linear method" used.

The next step is to let COMSOL do its work by pressing "Compute", **convergence** of the model can be monitored in an automatically generated "Convergence Plot" in the "Graphics" window as well as in the "Log" tab below the graphics window. After the model has converged **output** can be generated. This will be done in the "Results" section of the model builder, all kinds of thinkable outputs can be generated. Tables with obtained values have frequently be created, this can be done in a "Global Evaluation" tab. Curves repre-

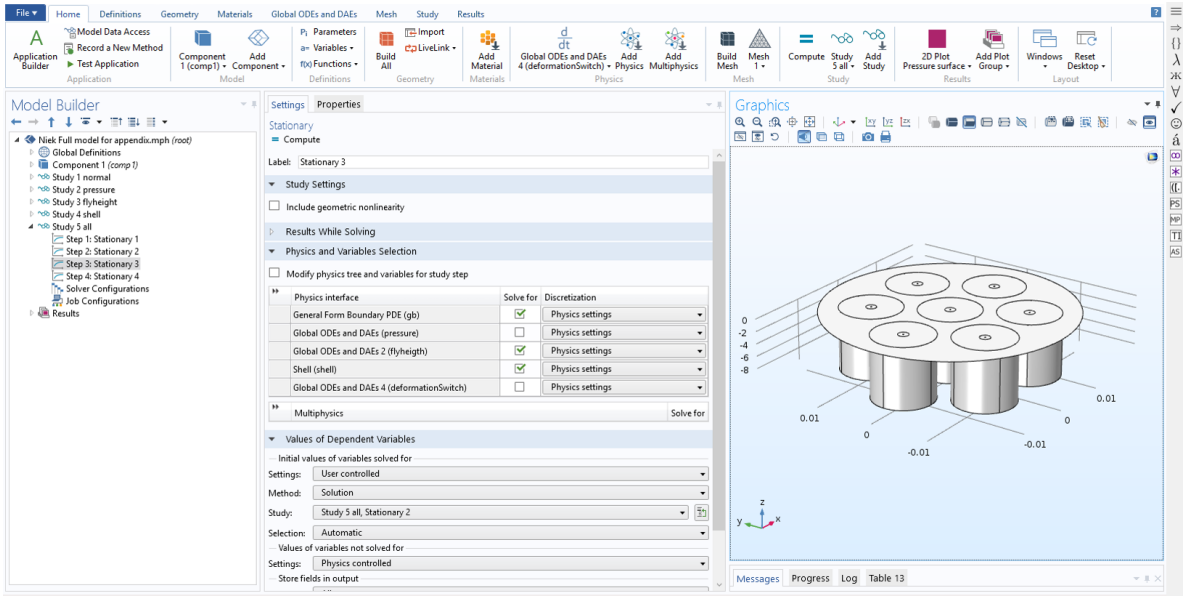

Figure F.4: COMSOLstudy

senting these global values have been made as well, in a "1D Plot Group" environment, see for example 3.7. More over a "2D Plot surface", to visualize variables that are not constant over the surface, has frequently be used as well, see for example figure 3.5.

Lastly some handy function are named that can save some time in building the model. First of all the "**atan2**" function can be used to describe the angle between a point on a circle and the origin with a value changing from π to $-\pi$, this function takes the location of the points with respect to the four quadrants into account. This angle was frequently necessary to describe a change in gap width around an actuator, this change is depending on the angle that can be defined with the atan2 function. The next tip involves the **Lagrange multiplier** denoted with "P_lm" in COMSOL, it has been found that an integrated Lagrange multiplier over the outlets of the actuators yields the mass flow for the defined outlets. Finally, **Matlab** should also be named, since this program can be used to control COMSOL, which means theoretically that the COMSOL interface is not necessary. However, the author of this report has built models in COMSOL since it is easier to keep an overview, Matlab has been used in some occasions to run the model for various configurations. Required lines of Matlab code that define a COMSOL model, can be found after saving a COMSOL model as a m-file.

Bibliography

[1] Mark Albert. Getting to submicron accuracy, 2004. URL http://www.mmsonline.com/articles/getting-to-submicron-accuracy.

[2] Amada Miyachi. Precision cutting options for medical devices. Technical report, Amada Miyachi America, 2015. URL http://www.amadamiyachi.com/.

[3] Twan Bearda. Pv & energy research at IMEC epitaxial silicon foils (epifoils). Technical report, IMEC, 2016.

[4] G Belforte, T Ã Raparelli, V Viktorov, and A Trivella. Discharge coefficients of orifice-type restrictor for aerostatic bearings. *Tribology International*, 40:512–521, 2007.

[5] G. Belforte, T. Raparelli, V. Viktorov, and Trivella. A. Metal woven wire cloth feeding system for gas bearings. *Tribology International*, 42:600–608, 2009.

[6] Thomas Booij, Ugljesa Todorovic, Roderik Verbruggen, and Janiek van Straalen. Evaluation of a layer-based pneumatic micro ball valve actuated by an electro-permanent magnet. Technical report, Delft University of Technology, Faculty of 3mE, 2016.

[7] W Borutzky, B Barnard, and J Thoma. An orifice flow model for laminar and turbulent conditions. *Simulation Modelling Practice and Theory*, 10:141–152, 2002.

[8] Douglas Brown. Tracker, 2017. URL http://physlets.org/tracker/.

[9] Geoffrey Carr. Sunny Uplands, nov 2012. URL http://www.economist.com/news/21566414-alternative-energy-will-no-longer-be-alternative-sunny-uplands.

[10] Henry Darcy. *Histoire des Fontaines publiques de la ville de Dijon.* Paris, 1856.

[11] Andrew J. Devitt. Porous vs. orifice air bearing technology. Technical report, New Way Air Bearings, 1999. URL http://www.ncbi.nlm.nih.gov/pubmed/19623112.

[12] Wei Gao, Yunbo Zhang, Devarajan Ramanujan, Karthik Ramani, Yong Chen, Christopher B. Williams, Charlie C.L. Wang, Yung C. Shin, Song Zhang, and Pablo D. Zavattieri. The status, challenges, and future of additive manufacturing in engineering. *Computer-Aided Design*, 69:65–89, 2015. URL http://linkinghub.elsevier.com/retrieve/pii/S0010448515000469.

[13] Konstantin T Holdermann, Reinhold E Schlosser, and Steffen Sterk. Thin Monocrystalline Silicon Solar Cells. *IEEE Transactions on Electron Devices*, 46(10):2055–2061, 1999.

[14] Yukio Hori. *Hydrodynamic Lubrication.* Springer-Verlag, Tokyo, 2002.

[15] F.C. Johansen. Flow through pipe orifices at low reynolds numbers. *Proceedings of the Royal Society of London. Series A*, 126(801):231–245, 1930.

[16] D. Kray, H. Kampwerth, E. Schneiderlöcher, A. Grohe, F.J. Kamerewerd, A. Leimenstoll, D. Osswald, A. Schäffer, S. Seitz, S. Wassie, S.W. Glunz, and G.P. Willeke. Comprehensive experimental study on the performance of very thin laser-fired high-efficiency solar cells. In *19th European Photovoltaic Solar Energy Conference*, number June, Paris, 2004.

[17] Martijn E. Krijnen. Control System Design for a Contactless Actuation System, 2016.

[18] Minhee Lee and Ho-young Kim. Toward Nanoscale Three-Dimensional Printing: Nanowalls Built of Electrospun Nano fi bers. *Langmuir ACS Publications*, 30:1210–1214, 2014.

[19] Made-in Europe. P-ECM: ultraprecies spaanloos bewerken, 2012. URL http://www.made-in-europe.nu/2012/10/p-ecm-ultraprecies-spaanloos-bewerken/.

[20] Gaëtan Masson, Sinead Orlandi, and Manoël Rekinger. Global Market Outlook for Photovoltaics 2014-2018. Technical report, European Photovoltaic Industry Assocation, 2014.

[21] Nena Milenkovic, Thomas Rachow, Stefan Janz, and Stefan Reber. Epitaxial Growth of High Quality n-type Silicon Foils in a Quasi-inline APCVD Reactor. *Energy Procedia*, 77:613–618, 2015.

[22] Mike Munsell. How Much Does It Cost to Manufacture a Solar Module in 2014? *Greentech Media*, November:2014–2016, 2014. URL http://www.greentechmedia.com/articles/read/how-much-does-it-cost-to-manufacture-a-solar-module-in-2014.

[23] Gregory F. Nemet. Beyond the learning curve: factors influencing cost reductions in photovoltaics. *Energy Policy*, 34:3218–3232, 2006.

[24] Kris Van Nieuwenhuysen, Valerie Depauw, Roberto Martini, Jonathan Govaerts, Maarten Debucquoy, Sivaramakrishnan Radhakrishnan, Ivan Gordon, Twan Bearda, Kris Baert, and Jef Poortmans. High quality epitaxial foils, obtained by a porous silicon based layer transfer process, for integration in back contacted solar cells. *27th European Photovoltaic Solar Energy Conference and Exhibition*, pages 2471–2474.

[25] Simon Philipps and Werner Warmuth. Photovoltaics Report. Technical Report November, Fraunhofer ISE, Freiburg, 2016. URL http://www.ise.fraunhofer.de/en/downloads-englisch/pdf-files-englisch/photovoltaics-report-slides.pdf.

[26] Osborne Reynolds. On the Theory of Lubrication and Its Application to Mr. Beauchamp Tower's Experiments, Including an Experimental Determination of the Viscosity of Olive Oil. *Proceedings of the Royal Society of London*, 40:191–203, 1886.

[27] Richard M. Swanson. A Vision for Crystalline Silicon Photovoltaics. *Prog. Photovolt: Res. Appl.*, 14:443–453, 2006.

[28] B.A. Robert Willis. On the Pressure produced on a flat Plate when opposed to a Stream of Air issuing from an Orifice in a plane Surface. October:129–140, 1828.

[29] R.P. Hoogeboom. Design and experimental validation of low stiffness aerostatic thrust bearings. 2016.

[30] Karl J. Schulitz, Helmut C. Sobek, Werner Hamermann. *Steel Construction Manual*. American Institute of Steel Construction, Chicago, 14th edition, 2005.

[31] Potomac Photonics Services. Laser Micromachining, 2016. URL http://www.potomac-laser.com/services/core/laser-micromachining/.

[32] Geoff Shannon. Fine laser cutting, 2011. URL http://www.industrial?lasers.com/articles/print/volume?26/issue?2/features/fine?laser?cutting.html.

[33] Jelle Snieder. Feasibility Study into the Application of a Contact- less Handling Stage in the ADAT3-XF. Technical report, Delft University of Technology / NXP Semiconductors, 2017.

[34] Beauchamp Tower. First report on Friction Experiments. *Proceedings of the Institution of Mechanical Engineers*, November:632–659, 1883.

[35] Richard Turton. A new approach to non-choking adiabatic compressible flow of an ideal gas in pipes with friction. *The Chemzcal Engzneerzng Journal*, 30:159–160, 1985.

[36] Eshan P Vagher. Contactless Passive Transport of Thin Solar Cells. 2016.

[37] Valco Instruments Co. Inc. VICI AG international. SPEEK Tubing: SS-clad PEEK with Flared PEEK Ends. URL https://vici.com/tube/SPEEK-tubing.php.

[38] Anton van Beek. *Advanced engineering design, Lifetime performance and reliability*. Delft University of Technology, 5th edition, 2012.

[39] Phuc Hong Vuong. *Air-Based Contactless Actuation System for Thin Substrates, the concept of using a controlled defromable surface.* PhD thesis, Delft University of Technology, 2016.

[40] Jasper Wesselingh. *Contactless positioning using an active air film.* PhD thesis, Delft University of Technology, 2011.

[41] Frank M. White. *Fluid Mechanics.* McGraw-Hill, New York, 7th edition, 2011.

[42] Kaufui V Wong and Aldo Hernandez. A Review of Additive Manufacturing. *International Scholarly Research Network*, 2012. doi: 10.5402/2012/208760.